A LINEAR FLUID INERTIA MODEL FOR IMPROVED PREDICTION OF FORCE COEFFICIENTS IN GROOVED SQUEEZE FILM DAMPERS AND GROOVED OIL SEAL RINGS

A Dissertation

by

ADOLFO DELGADO-MARQUEZ

Submitted to the Office of Graduate Studies of
Texas A&M University
in partial fulfillment of the requirements for the degree of

DOCTOR OF PHILOSOPHY

December 2008

Major Subject: Mechanical Engineering

A LINEAR FLUID INERTIA MODEL FOR IMPROVED PREDICTION OF FORCE COEFFICIENTS IN GROOVED SQUEEZE FILM DAMPERS AND GROOVED OIL SEAL RINGS

A Dissertation

by

ADOLFO DELGADO-MARQUEZ

Submitted to the Office of Graduate Studies of
Texas A&M University
in partial fulfillment of the requirements for the degree of

DOCTOR OF PHILOSOPHY

Approved by:

Chair of Committee,	Luis San Andrés
Committee Members,	Luciana Barroso
	Dara W. Childs
	Chii-Der Suh
Head of Department,	Dennis L. O'Neal

December 2008

Major Subject: Mechanical Engineering

ABSTRACT

A Linear Fluid Inertia Model for Improved Prediction of Force Coefficients in Grooved Squeeze Film Dampers and Grooved Oil Seal Rings. (December 2008)

Adolfo Delgado-Marquez, B.S., Universidad Simón Bolívar;

M.S., Texas A&M University

Chair of Advisory Committee: Dr. Luis San Andrés

In Squeeze Film Dampers, (SFD), grooves (deep or shallow) are used to feed oil into the damper and prevent oil starvation within the fluid film lands. In oil seals with film land of clearance *c*, short shallow grooves (depth ≤ 15*c*, length ≤ 30*c*) are machined to reduce the cross-coupled stiffness coefficients, and thus improve the seal stability characteristics. Moreover, test stands for these devices can also incorporate grooves or recesses as part of oil feeding/ discharge arrangements. A common assumption is that these grooves do not influence the test system forced response. However, unexpected large added mass coefficients are reported in these configurations and not adequately predicted. In the case of grooved oil seals, experimental results also show that circumferential grooves do aid to reduce cross-coupled force coefficients but to a lesser extent than predictions otherwise indicate.

A linear fluid inertia model for analysis of multiple-groove SFD or oil seal configurations is advanced. A perturbation analysis for small motion about a journal centered and off-centered position yields zeroth and first order flow equations defined at each individual flow region (land and grooves) of constant clearance (c).The analysis considers both the circumferential and axial dynamic pressure variations across the groove and land regions. At the groove regions, an effective groove depth (d_η) and effective clearance ($c_\eta = d_\eta + c$) are defined based on qualitative observations of the laminar flow pattern through annular cavities. This depth differs from the actual physical groove depth. The boundary conditions at the inlet and exit plane are a function of the

geometric configuration. Integration of the resulting dynamic pressure fields on the journal surface yields the force coefficients (stiffness, damping, and inertia).

Comparisons between predicted and experimental force coefficients for a grooved oil seal and a SFD show excellent correlation over a narrow range of effective groove depths. The results confirm that large added mass coefficients are associated to the feed/discharge grooves in the scrutinized test configurations. Furthermore, predictions, benchmarking experimental data, corroborate that short inner land grooves in an oil seal do not isolate the pressure field of the adjacent film lands, and hence contribute greatly to the force response of the seal.

DEDICATION

To my mother, father, brother, and Elia

ACKNOWLEDGEMENTS

I thank my advisor and committee chair, Dr. Luis San Andrés, for his generous advice and continued support over the course of this research.

Thanks to Dr. Dara Childs for his valuable advice, as well as for facilitating the access to the oil seal experimental data. I also thank Dr. Chii-Der Suh and Dr. Luciana Barroso for their careful review of this dissertation.

Thanks to all the graduate students at the Rotordynamics Laboratory, especially: Zach Zutavern, Arun Suryanarayanan, Ahmed Gamal and Sang Hyun Park. I also thank Eddie Denk and the rest of the Turbomachinery Laboratory staff for all their assistance.

The financial support by the Texas A&M Turbomachinery consortium is gratefully acknowledged.

Finally, I would like to express my sincere appreciation to Dr. Luis San Andrés for giving me the opportunity to pursue research at Texas A&M Turbomachinery Laboratory under his guidance. His dedication and passion towards research are an inspiration.

NOMENCLATURE

C_{ij}	Direct damping coefficients [N.s/m] $i,j=X,Y$
c	Clearance [μm]
$(c,s)_{f,g}$	Complex coefficients of dynamic pressure functions [Pa/m]
c_η	Effective clearance [m]
d_η	Effective depth [m]
e_0	Journal eccentricity [m]
f^e	Element external velocity vector (FEM)
$(f,g)_{X,Y}$	Dynamic pressure functions [Pa/m]
h	Film thickness [m]
L	Axial length [m]
K_{ij}	Direct stiffness coefficients [N/m] $i,j=X,Y$
k_{ij}	Cross-coupled stiffness coefficient [N/m] $i,j=X,Y$
$k_{x,z}$	Shear flow factors
k^e, S^e	Element fluidity matrix (FEM)
M_{ij}	Added mass coefficient [Kg] $i,j=X,Y$
Nem	Number of elements (FEM mesh)
n_{pe}	Number of Nodes per element (FEM)
N	Number of flow regions
P	Pressure [Pa]
P_X,P_Y	First-order pressure field [Pa]
P^e	Element pressure matrix (FEM)
$\dot{q}$	Fluid flow rate [m/s^3]
i	Imaginary number ($\sqrt{-1}$)
R	Journal radius [m]
Re_A	$V_A c\rho/\mu$. Axial flow Reynolds number
Re^*	$\omega c^2/\nu$ Modified squeeze film Reynolds number

s	Zeroth order pressure axial gradient [Pa/m]
t	Time [s]
V_A	Axial velocity [m/s]
V_x, V_z	Bulk flow velocities [m/s]
X,Y,Z	Inertial coordinate system [m]
x,z	Circumferential and axial coordinates [m]
Δe	Displacement amplitude [m]
ε	Eccentricity ratio (e/c)
Γ^e	Finite element boundary (FEM)
μ	Absolute viscosity [Pa.s]
ν	Kinematic viscosity [m^2/s]
Ω	Rotor rotational speed [rad/s]
Ω^e	Finite element (FEM)
ω	Rotor whirling frequency [rad/s]
ρ	Oil density [kg/m^3]
θ	Angular coordinate [deg]
ψ	Interpolation functions (FEM)
Subscripts	
0	Zeroth order solution
exp.	Derived from experiments
g	groove
N	Last annular cavity section
model	Derived from predictions
S	Supply
D	Discharge
α	α-th annular cavity section
σ	*X,Y* coordinates

TABLE OF CONTENTS

Page

LIST OF TABLES

Page

LIST OF FIGURES

Page

Page

Page

1. INTRODUCTION

In squeeze film lubrication, the hydrodynamic pressures generated by the fluid film can be classified into viscous and inertial. The relative contribution of the viscous and inertial pressure fields to the thin film reaction force is quantified in terms of the squeeze film (or modified) Reynolds number ($Re^* = \omega c^2/\nu$), where ω is frequency of vibration, c is the film clearance, and ν the fluid kinematic viscosity. Furthermore, the linearized representation of the fluid film bearing reaction force is expressed as $F = -Kx - C\dot{x} - M\ddot{x}$, where *K, C, M* are the bearing stiffness, damping and mass coefficients, respectively. The three terms of the reaction force represent the elastic, viscous dissipation and inertia forces, respectively. In most practical applications of thin film hydrodynamic lubrication, like journal bearings, $Re^* < 1$ due to the smallness of the bearing clearance [1]. In these cases, viscous film forces are much larger than fluid film inertial forces; and thus, the inertialess fluid flow assumption of classical lubrication theory is plausible. For other applications with large clearances or geometries including circumferential grooves (i.e. with $Re^* \geq 12$), fluid inertia forces become significant and comparable to viscous forces. In these cases there is a so called "apparent mass effect" that generates a radial reaction force that opposes the acceleration of the journal. Thus, the net effect is a system with a larger mass. In short rotors, this mass is significant respect to the rotor mass and could appreciably change the natural frequency of the bearing system [2].

SFDs comprise of an annular thin film of lubricant between two non-rotating surfaces. Commonly, the inner surface or journal is the outer race of a ball bearing and the outer surface is the bearing housing, as shown in Fig. 1. Vibration in a machine induces a whirling (precessional motion) journal orbit that squeezes the oil film periodically. Hydrodynamic pressures are generated during the squeeze motion action on the whirling surface, thus reducing the amplitude of vibration. Large fluid inertia forces are apparent in squeeze film dampers since these operate with larger Re^* than in typical journal bearings. SFDs usually include feeding and discharge grooves. A groove

---

This dissertation follows the style of *ASME Journal of Tribology*.

is a deep and wide channel machined around the bearing circumference. Grooves are thought to keep a uniform pressure and used to feed oil into the damper film land. Similarly, SFDs with end seals generally incorporate grooves at the side end of the damper land. These grooves provide an oil plenum that, when filled, prevents the ingestion of air into the damper land [1].

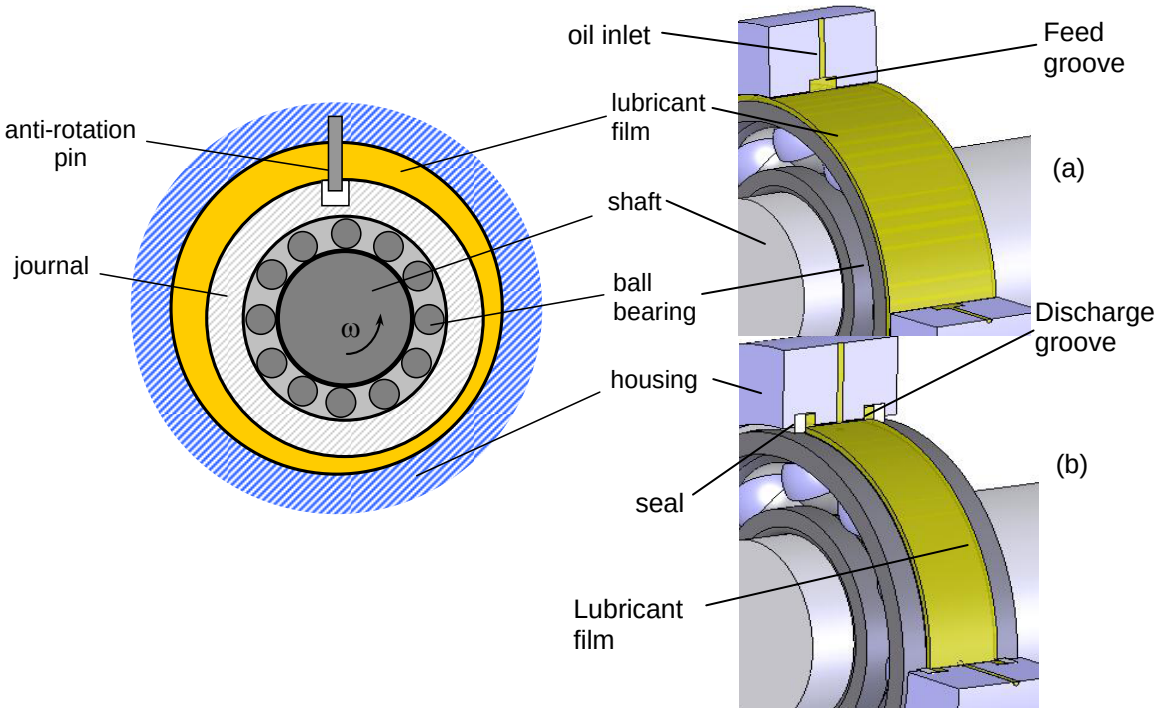

Figure 1 Squeeze film damper (SFD) grooved configuration. a) SFD with central feed groove. b) SFD with end grooves and seals [1].

Fluid film inertia forces in single land SFDs have been extensively investigated. As early as 1967, Kuzma [3] analyzes the effect of fluid inertia effects on squeeze films in simple geometries (parallel plates). Later, Reinhart and Lund [4] obtain the force coefficients for plain journal bearings including the contribution of fluid inertia forces, and indicate that the added mass coefficient can be significant in small machines with short rotors. Later on, a number of researchers [5-17] conduct extensive work to qualify and quantify the fluid film inertia effects in squeeze films. In general, predictions of fluid film inertia coefficients present adequate correlation with experimental results only

for the simplest geometries tested (i.e. without grooves or end seals). In practical configurations, which include feeding grooves and recesses (mainly shallow ones, i.e. depth < 15c), added mass coefficient are underpredicted by about 50% [12]. The apparent discrepancies prompted many researches to investigate the effect of grooves (shallow ones) on the SFD forced response [18-26]. However, up to this date, added mass coefficients in SFDs remain to be properly predicted for most common geometries including deep and/or shallow grooves, as evidenced in recent experimental work [27]. This deficiency also extends to other grooved geometries like oil seal rings. However, in grooved oil seals not only the added mass coefficients are largely underpredicted, but the cross-coupled stiffness coefficients are also underpredicted by available models (i.e. Ref. [28]) as indicated by Graviss [29].

Oil seal rings are used in centrifugal compressors to prevent leakage of the process gas into the support oil lubricated bearing cartridge as well as to ambient [30]. An oil seal, shown in Fig. 2, comprises of two spring loaded floating rings that, when locked due friction forces at the contact surfaces, act as a plain journal bearing [28]. These seals are known as potential sources of instability due to the generation of large cross-coupled stiffnesses [31-32]. A common practice to minimize the destabilizing effect of oil seals is to machine circumferential grooves to isolate and divide the seal land into shorter length lands, thus reducing the fluid film forces [33]. To date, there are major discrepancies between predicted and experimental force coefficients obtained in grooved seals. Experimental results detailed in Refs. [29, 30, 34] show that circumferential grooves do aid to reduce cross-coupled force coefficients but to a lesser extent than predictions otherwise indicate. Furthermore, experimental added mass coefficients are found to be very large; and worse yet, not even modeled in available predictive tools. More importantly, the test data reveals large magnitude added mass coefficients even for a smooth oil seal (i.e. without grooves) [29, 30, 34]. In actuality, the smooth seal configuration tested in Refs. [29, 30, 34] does include a deep central groove that feeds lubricant into two seals. The seals are installed in parallel in an axially symmetric arrangement with the purpose of balancing the test rig thrust force. The identification of

the force coefficients follows the premise that the force coefficients of each seal correspond to half the value of the force coefficients associated to the test configuration. Thus, it is assumed that the central groove does not affect the forced response based on the commonly accepted rationale that deep grooves do not generate dynamic pressures.

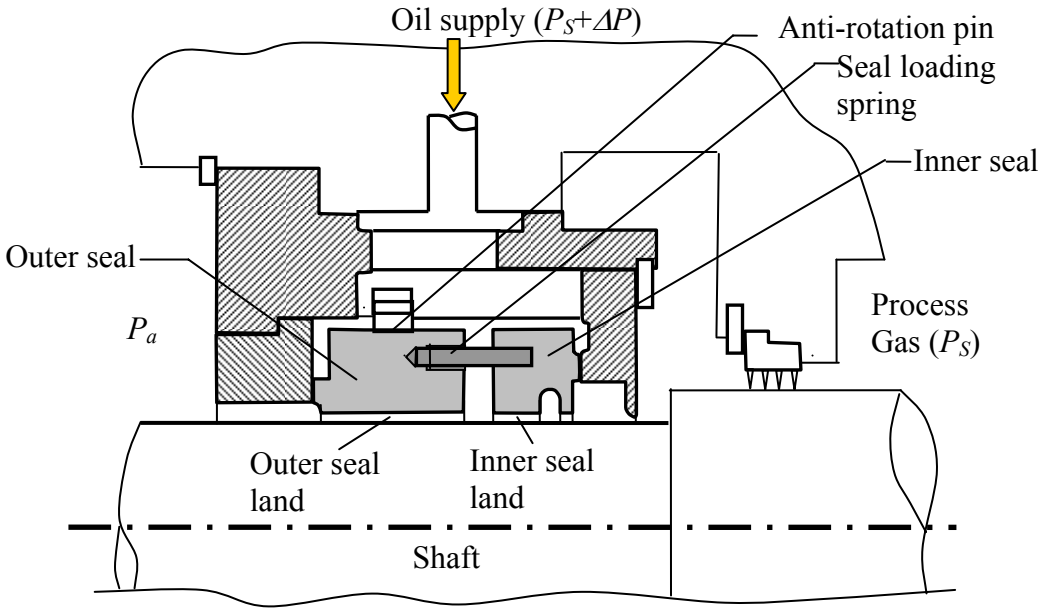

Figure 2 Typical oil seal multi-ring assembly.

The abundance of experimental data showing large added mass coefficients for seal and SFD configurations with grooves (i.e. Ref. [27, 29]), and the inadequacy of predictive models to address this issue are an urgent concern. In the case of grooved oil seals, damping and stiffness coefficients are also largely underpredicted by available models (i.e. Ref. [28]). The discrepancy between predictions and experimental results reveals that grooves do affect the forced response of these test configurations. Hence, the objective of this study is to incorporate shallow and/or deep grooves into a fluid film flow model for predicting force coefficients in grooved SFDs and grooved oil seals.

2. LITERATURE REVIEW

This section presents a review of the existing experimental and analytical research quantifying fluid inertia effects on the dynamic force response of grooved SFDs and grooved oil seals. The reader should refer to Della Pietra and Adilleta [35, 36] for a more general and comprehensive review of the state of the art in SFDs from 1963 to 2002. In these references, the authors call for better models to predict force coefficients in SFDs with practical geometries (i.e. including circumferential grooves and recesses).

The first section briefly describes early work to investigate fluid inertia forces in simple SFD geometries (i.e. without grooves or smooth land) and moves into an examination of the most relevant experimental work on SFD configurations including grooves, as well as analytical developments to predict the force coefficients in such configurations. Next, the review presents experimental results evidencing large added mass coefficients in SFD and oil seal test configurations including deep lubricant supply grooves. Finally, the last section presents a survey of experimental research related to the identification of force coefficients in grooved oil seals and the analytical tools available to predict their dynamic forced performance.

2.1 Grooved SFDs

Reinhart and Lund [4], in a classical paper, derive the force coefficients for journal bearings including fluid inertia effects. Prior to this work, fluid inertia effects were only considered in the analysis of simple geometries like parallel plates [3]. Reinhardt and Lund, using a perturbation analysis with the modified Reynolds number (Re^*) as the small parameter $O(1)$, corroborate that fluid inertia forces may be larger than the mass of the journal itself in long bearings, and henceforth significant in short length rotors.

Other authors, like Brennen [5] and Mulcahy [11], included the effects of fluid inertia when analyzing other applications including long whirling shafts. In the case of Brennen [5], the author presents a laminar flow analysis to determine the fluid forces in liquid sodium pumps for cooling nuclear reactors. The analysis includes the case of pure whirling and whirling with rotation for increasing clearance ratios and Reynolds

numbers (Re^*). The results show that fluid inertia reaction forces dominate the viscous forces for large values of Re^*. Similarly, in the analysis of fluid film forces in long whirling helicopter shafts, Mulcahy [11] obtains a closed-form solution for predicting force coefficient on finite length thin films for small translational journal motion about its centered position. This analytical solution is elegant and simple, and most importantly, it served as a starting point for other authors [12, 24] to obtain closed-form solutions for predicting force coefficients in finite-length SFDs for small circular orbits about a centered position.

Tichy [5] later focuses on analyzing fluid inertia forces from a quantitative point of view. Tichy gives an insightful physical interpretation of the fluid inertia film forces and their importance in the forced performance of dampers and journal bearings. In general, fluid inertia forces become significant in thin film flows in the case that the component of the flow induced by whirling motions (Poiseuille flow) is comparable to the shear flow component (Couette flow). Theses findings imply that in a thin film flow system with purely whirling motions (i.e. SFDs), or with whirling and rotating motion but with relatively large clearances (i.e. annular grooves), the forces of inertial nature can not be neglected. These remarks explain, from a qualitative point of view, the amplification of fluid inertia effects in oils seal and SFD test configurations including grooves (i.e. large clearance regions). Also, in more practical terms, Tichy quantifies the significance of fluid inertia forces in smooth-land squeeze-film flows with the analysis of viscoelastic fluids for small centered journal and off-centered journal whirling motions [8-10]. The analyses show that fluid inertia forces are indeed comparable to viscous forces in squeeze film dampers when $Re^*>12$. More importantly, Tichy also shows that solutions using Re^* as a small parameter are accurate for values up to $Re^*=20$.

Modest and Tichy [7] analyze the relative contribution of the temporal and convective fluid inertia terms to the resulting inertia force. The authors demonstrate, with an order of magnitude analysis, that inertia advection (nonlinear) terms are negligible with respect to temporal inertia terms for small amplitude motions about a static equilibrium position. This leads to an important simplification that makes the fluid

film equation including inertial effects linear and thus amenable for closed-form solutions.

Since the early 1980's, an extensive analytical and experimental investigation to study fluid inertia forces in SFDs has been conducted at the Texas A&M Turbomachinery Laboratory. The research effort extends from experiments to analytical developments to understand and predict the fluid inertia forces in SFDs. First, San Andrés [12] extensively investigates fluid inertia effects in single land SFDs. The author derives expressions to calculate force coefficient on SFDs for small, large, center and off-centered journal orbits using various approaches. The work strives to provide predictions of added mass coefficients for most common SFD operating conditions. The most important findings include that, for circular centered journal orbits, the fluid inertia coefficient or added mass decreases as the orbit radius increases due to the effect of convective acceleration terms. The maximum difference of the added mass coefficient calculated using an inviscid flow assumption (i.e. $Re^*=\infty$) or $Re^*=0$ is within 20%. Also, for small amplitude circular centered orbits, San Andrés presents a closed-form solution for the fluid film force coefficients. The solution for whirling motions, based on Mulcahy's analysis for translational motions [12], is obtained by considering that the flow is steady in a coordinate system rotating with the same journal precessional speed. Similar considerations are included in the hereby proposed analysis, to be discussed later. In addition, San Andrés' keen observation that added mass coefficients are proportional to $1/c$ while the damping coefficients are proportional $1/c^3$ proves to be fundamental in the development of the presently proposed model.

Besides the contributions to the analysis of single land SFDs, Ref. [12] presents tests on two SFD configurations that include a central feed groove and O-rings sealing the damper ends. One configuration has an inlet groove clearance (c_g) of 6 times the land clearance ($c_g/c = 6$); while in the other configuration $c_g/c = 10$ and also includes a groove at the sealed end of the damper ($c_g/c = 3$). Dynamic pressure measurements at the grooves reveal large amplitudes and out of phase with the film land dynamic pressures. The experimental results evidence that in both configurations, the central and

end grooves largely influence the film land pressure profiles and the SFD fluid film reaction forces.

The findings in Ref. [12] prompted the investigation of the effect of circumferential grooves on the force response of SFDs, and more importantly, lead to question the common rationale that there is no generation of dynamic pressure in (deep) grooves. To this end, San Andrés and Vance [37] present further experimental work with measured dynamic pressures at the central feeding groove ($c_g/c = 6$) that are 1/3 of those recorded at the film land. Zeidan and Vance [38] also report forces at the central feed groove ($c_g/c = 7$) as large as 60% of those identified at the damper film lands. From this point on, many researchers concentrated their efforts on quantifying the effects of central feed grooves on the forced response of SFDs to improve the prediction of force coefficients.

San Andrés [18] presents an analysis, based on the short length bearing model and for small centered journal motions, that treats the fluid volume at the groove as a capacitance and the liquid as slightly compressible. Based on experimental evidence, the analysis assumes that the dynamic pressure at the groove is not null. This pressure is obtained through a mass flow balance at the groove-land interface. The correlation of predictions and experimental data from Ramli *et al.* [39], show that a SFD with a shallow groove ($c_g/C = 3$) behaves at low frequencies as a single land damper (i.e. w/o groove). Furthermore, dynamic force coefficients are determined to be frequency dependent at high excitation frequencies. However, the groove volume-liquid compressibility effects are limited to large frequencies of no practical interest.

Arauz [40] extends the analytical work in Ref. [18] by considering the circumferential flow in the central feed groove. He also conducts experiments to quantify the fluid film forces developed in SFD incorporating a central supply groove (c_g = 6c, 11c) . The work is condensed and presented in two technical publications by Arauz and San Andrés [19, 20]. In Ref. [19], Arauz and San Andrés solve analytically the bulk flow equations at the grooves without including fluid compressibility and considering both the circumferential and axial pressure variations. The closed-form solution is valid for small amplitude motions around a centered position. The pressure

distribution at the film land is predicted using the short length bearing model including fluid inertia. Predictions of tangential and radial forces (per unit axial length) at the groove and at the SFD lands are compared to experimental results from Ref. [40]. The predictions reproduce well dynamic forces at the groove, but underestimate the radial force and overestimate the tangential (damping) force at the damper film land. This might be related to the fact that the authors considered the full volume of the groove for the local mass balance at the groove-land interface. In addition, the use of the short length bearing model to analyze the SFD land may also add to the discrepancy between the forces predicted and measured at the SFD land. Arauz and San Andrés [20] also present tests revealing the importance of a circumferential feeding groove and recirculation annuli on the forced response of a test damper. The test results show that the radial forces in a damper with grooves, clearance ratios (c_g/c) of 6 to 11, are similar or larger to those at the SFD film land (depending on the journal whirl orbit amplitude). For uncavitated lubricant conditions, the tangential (damping) forces at the groove are smaller than at the damper film land but still of comparable magnitude.

Zhang and Roberts [21] present an analysis to predict SFD force coefficients including the effects of a shallow central groove ($c_g/c = 3$) and oil supply system. The authors make a balance of the flow and pressure starting at the upstream supply line, passing through a recirculation groove, and into the damper film lands. The pressure magnitudes at the groove are a function of four correction factors that depend on the flow resistance of the lubricant supply lines and size of the groove. The expression of the pressure drop at the groove-film land interface is obtained by using an inertialess axial velocity profile and integrating the axial momentum and continuity equations across the film thickness. Predictions of damping and inertia force coefficients are compared to experimental values obtained by Ellis *et al.* [22] and Zhang *et al.* [23]. The comparisons show that the new analytical formulas render better predictions of damping coefficients but only improve marginally the predictions of added mass coefficients with respect to classical predictions without including the effect of the grooves [4, 12].

Qingchang *et al.* [24] analyze the effect of circumferential grooves on the forced response of SFDs. The authors analyze the grooved portion of the damper following the model described in Ref. [18], and for the squeeze-film land the authors use a similar approach to that by Tichy and Bou-said [41]. The predictions are presented in terms of the radial and tangential reaction forces. From these expressions, the authors conclude that a groove affects the fluid film tangential forces but does not influence the radial force component. In other words, the authors indicate that the fluid inertia effects in a groove are not important. This conclusion contradicts experimental and analytical results found in the open literature on grooved SFDs. The authors compare predictions of fluid film forces to experimental results for journal amplitude up to 80% of the clearance, although the equations included in the analysis are not valid for such large motions. The predictions show good correlation for the tangential force at the lowest test journal orbit amplitudes, but the radial (inertia) force is underpredicted for all test amplitudes.

Lund *et al.* [25] present predictions and experimental results of dynamic force coefficients of a SFD with a central groove and sealed at both ends with O-rings. An equivalent first-order Reynolds equation is derived and solved using a perturbation analysis for small amplitude journal motion. The authors invoke the short-length bearing assumption in the solution of the pressure field even though the damper ends are sealed with O-rings. A bulk flow model describes the conditions in the central groove and the pressure is obtained through a flow balance at the groove-land interface. The authors consider the flow at the grooves as inviscid and the expression for the axial flow does not include the acceleration term. The damping and added mass coefficients predictions are presented in dimensionless form and compared with experimental results for different groove-to-land volume ratios, but there is not indication of the actual values of the damper clearance or groove depth. In any case, the experimentally identified fluid inertia force coefficients are largely overpredicted (up to 70 %) as the groove volume increases.

Kim and Lee [23] present experiments and predictions of the force coefficients in a sealed SFD with feed and discharge grooves. The theoretical development follows from

the bulk-flow equations with the pressure and velocity fields as originally given by Mulcahy [11] and San Andrés [12]. The dynamic film pressure at the groove is obtained as in Ref. [18] where the fluid at the groove is regarded as slightly compressible, although their experimental study is limited to low excitation frequencies (< 50Hz). The tests and analysis includes a two-stage (step-journal) seal configuration. Predictions of the fluid inertia coefficient correlate well with experimental data while the damping coefficients are underestimated. Interestingly, the curve fit of the experimentally identified inertia force seems to underpredict the actual slope described by the experimental data points. The actual groove depth-to-clearance ratio of the inlet groove is not reported.

To date, the analytical work on SFDs with grooves is mainly limited to relatively small groove clearance ratios (c_g/c= 5) with the few exceptions as in Ref. [40] (i.e. c_g/c = 11). Even for such shallow grooves, there are still discrepancies in the prediction of SFD added mass coefficients. In addition, recent experiments by San Andrés and Delgado [27] show large added mass coefficients for SFD configurations with much deeper grooves that those previously considered. In this experimental work, the authors identify the force coefficients of an end sealed SFD describing circular centered orbits. The vertical SFD is fed from a plenum, and incorporates deep circumferential grooves at the inlet (c_g = 78c) and outlet (c_g= 36c) of the damper film land section. The identified damping coefficients are presented as a function of the amplitude of motion and correlate well with well known formulas found in the literature [42]. On the other hand, the added mass coefficients are largely underpredicted. Dynamic pressure measurements at the end groove reveal significant magnitudes, and with peak pressures 180^o offset with respect to the minimum film thickness. This result suggests that even deep grooves have an important influence on the forced response of the damper and that the dynamic pressure field generated at the groove is mainly due to fluid inertia. Similar results, showing large added mass coefficients, are also seen in oil seal test configuration for both smooth and grooved oil seals, as explained next.

2.2 Grooved Oil Seals

As advanced in Section 1, oil seal rings are well known sources of rotordynamic instability [30], and it is a common practice to machine grooves within the oil seal land to partition the film into smaller segments. The expected effect is to reduce the magnitudes of the seal cross-coupled stiffness coefficients. However, the archival literature for laminar flow oil grooved seals is rather scant [30, 43]. Most annular seal work has been conducted to analyze turbulent flow annular pressure seals typical in high pressure compressors and pumps [43]. This literature review includes the current available computational tools and experimental results for laminar-flow grooved oil seals, i.e. axial flow Reynolds number ($Re_A = V_a * c/\nu$) $\leq$ 2000, with V_a as the axial mean flow velocity, c as the film clearance, and ν is the kinematic viscosity.

Semanate and San Andrés [28] present an isoviscous flow analysis to predict force coefficients of a grooved oil seal operating under either laminar or turbulent flow regimes. The model does not account for fluid inertia terms in the film land. The analysis does model fluid inertia and viscous edge effects at the seal inlet and includes a variable clearance tapered seal. The force coefficients are presented in terms of the ring eccentricity ratio for three seal cases: single land, two lands and three lands. The numerical results show that both the cross-coupled stiffness and direct damping coefficients are substantially reduced. These findings imply that the grooves effectively separate the seal lands and thus reduce the seal force coefficients. However, the whirl frequency ratio (WFR) remains relatively constant, and thus there is not significant improvement of the seal dynamic stability characteristics. Regarding the entrance effects due to viscous and inertia effects, the predictions indicate that such effects are of importance only in very high pressure applications. Ref. [44] presents similar conclusions and a more detailed discussion on fluid inertia and viscous entrance effects.

Baheti and Kirk [33] analyze the dynamic response of grooved oil seals including thermal effects. The coupled pressure and temperature transport equations, developed in terms of a perturbation analysis for small amplitude motions, are solved with a finite element solution scheme. The study includes arc and square groove geometries. The

numerical results show a reduction of 40% in the direct damping and cross-coupled stiffness coefficients of an oil seal when including a square groove with a groove-depth to clearance ratio (c_g/c) of 6. On the other hand, when using a deeper groove (c_g/c = 15) the force coefficients are reduced by a factor of 4 when adding a single groove seal, and by 10 when adding two grooves. Thus, for the latter case, the results indicate that the groove effectively isolates the pressure distribution of the contiguous film lands.

Childs *et al.* [30] experimentally identify the rotordynamic force coefficients and leakage characteristics of a smooth oil seal and grooved oil seals operating in the laminar flow regime. The test configuration used in Ref. [30] is similar to that employed in Refs. [29, 34] as described in Section 1. The test rig includes a deep inlet central plenum (~136 c) that feeds a pair of parallel seals installed in an axially symmetric arrangement to balance the thrust load generated due to the pressure drop across the seals. Nevertheless, it is assumed that the central groove does not affect the test system forced response. The authors aim to identify the influence of the inner land groove on the rotordynamic performance of oil seals and evaluate the accuracy of the existing predictive models. The paper includes a detailed description of smooth and grooved oil seals and their operating features, and a comprehensive literature review of the previous work conducted in oil seals operating in the laminar flow regime. Particularly, prior to this publication, the only experimental work on laminar-flow oil seals was conducted by Kaneko [45] on smooth seals. In Ref. [30], static and dynamic force coefficients are identified for a smooth seal, a 1-groove seal, and 3-groove seal (with c_g/c = 6). The experimental force coefficients for the smooth seal correlate well with predictions from Zirkelback and San Andrés [46] except for the added mass coefficient that are underestimated by a factor of 10. Precisely, the authors mention the large oil supply groove as a possible source for the large discrepancy between experimental and predicted added mass coefficients. However, pressure measurements at both the inlet groove and exit cavity show no significant magnitudes for the dynamic pressures. Hence, they discard the rationale that the groove is responsible for such unusually large added mass coefficient (~20 kg). Furthermore, the experimental stiffness and damping

coefficients for the grooved oil seal are largely underestimated by the prediction model in Ref. [28]. These results suggest that, contrary to the predictive model assumptions, the grooves are not deep enough to isolate the hydrodynamic film pressure from contiguous seal lands.

Childs *et al.* [34] present experimental results, extracted from Graviss' thesis [29], evidencing the effect of groove depth on the dynamic forced response and leakage performance of a test oil seal. Similarly to Ref. [30], the experimental set up includes a deep inlet central plenum feeding a pair of parallel seals. Force coefficients are identified for three grooved seals with three groove clearance ratios (c_g/c): 6, 11, and 16. The laminar flow oil seal force coefficients and leakage measurements are presented as a function of the operating static journal eccentricity for increasing rotor speeds (up to 10,000 rpm) and oil supply pressures (up to 70 bar). The test results indicate that the force coefficients decrease for increasing groove depths except for the added mass coefficients. However, predictions based on Ref. [28] largely underestimate the grooved seal oil stiffness and damping coefficients even for the configuration with the deepest groove. Thus, the experiments suggest that even for groove-depths to clearance ratios of 15 the grooves do not completely isolate the hydrodynamic pressures of the two adjacent seal lands (i.e. K_{xy} (2 lands) ≠ ¼ K_{xy} (1 land), C_{xx}(2 lands) ≠ ¼ C_{xx}(1 land). In addition, similar to Ref. [30], the experimental results also show relatively large added mass coefficients that increase as the groove depth increases (up to 30 kg). However, predictions of added mass coefficients using formula in Ref. [4] yield 2.8 kg (i.e. nearly 10 times smaller than the experimental value).

In addition to the work in laminar flow oil ring seals, it is also important to mention the analytical models to analyze the dynamic forced performance of Lomakin bearings [47, 48], since their geometry closely resembles the test configuration in Ref. [29, 30, 34] (i.e. parallel thin film lands separated by a central deep groove). Although the process liquid is injected in an angle (against the journal rotation) and the fluid flow is turbulent, the analysis of these bearings focuses on incorporating the inlet feed groove into the fluid film model to predict the whole bearing force coefficients. Both, San

Andrés *et al.* [47] and Arghir *et al.* [48], analyze the flow at the film land using a two dimensional bulk-flow model, while the flow at the groove is represented as purely circumferential. However, while Ref. [47] neglects fluid film effects at the groove (i.e. inertialess though turbulent flow), Ref. [48] considers that the flow is dominated by inertia forces based on the large Reynolds number values at the groove ($Re^* \sim 26{,}000$). Nevertheless, the large Re^* value is based on the surface circumferential velocity of the flow at the groove, which is related to fluid jet injected through the angled supply orifices and not to squeeze film motions. In fact, the Reynolds number (Re^*) in the groove based on the journal whirl frequency (ω) is as low as 0.02. Thus, considering that inertia effects are related to flow field driven by squeeze motions [5], the Re^* reported in Ref. [48] is not a good indicator of the relative contribution of fluid inertia effects respect to viscous effects. Interestingly enough, both models (Refs. [47, 48]) overpredict experimental added mass coefficients of a test water Lomakin bearing [49].

3. FLUID FLOW MODEL AND MAJOR ASSUMPTION IN GROOVED FILM GEOMETRIES

3.1 Introduction

The analysis aims to predict fluid film forces developed in annular thin film geometries including deep/shallow grooves or annular recesses. Unlike prior fluid film analyses of grooved geometries, the current development treats both the groove and film land sections similarly, based on a major consideration derived from the experimental results in Refs. [27, 29]. The development of this approach is already advanced in prior reports [50, 51] also part of this research effort. The formulation of the fluid film flow equations and a detailed explanation of the assumptions involved in the proposed analytical development follow.

3.2 Fundamental Fluid Flow Equations

Presently, the formulation is illustrated for an axially symmetric annular cavity that includes a central (mid-plane) feeding groove, as shown in Fig. 3. In particular, this geometry is representative of the test configuration in Ref. [29].

Only half of the system is considered due to symmetry. The flow region, including land and groove portions, is divided into sub-flow regions (α= *I, II,...N*). Within each individual sub-flow region the fluid flow rates ($\dot{q}_\alpha$) in the circumferential (*x*) and axial (*z*) directions are:

$$\dot{q}_{x_\alpha} = h_\alpha V_{x_\alpha} \; ; \; \dot{q}_{z_\alpha} = h_\alpha V_{z_\alpha} \qquad \alpha = I, II, ...N \tag{3.1}$$

where h_α is the film thickness and ($V_{x_\alpha}, V_{z_\alpha}$) are bulk-flow velocities in each flow region α.

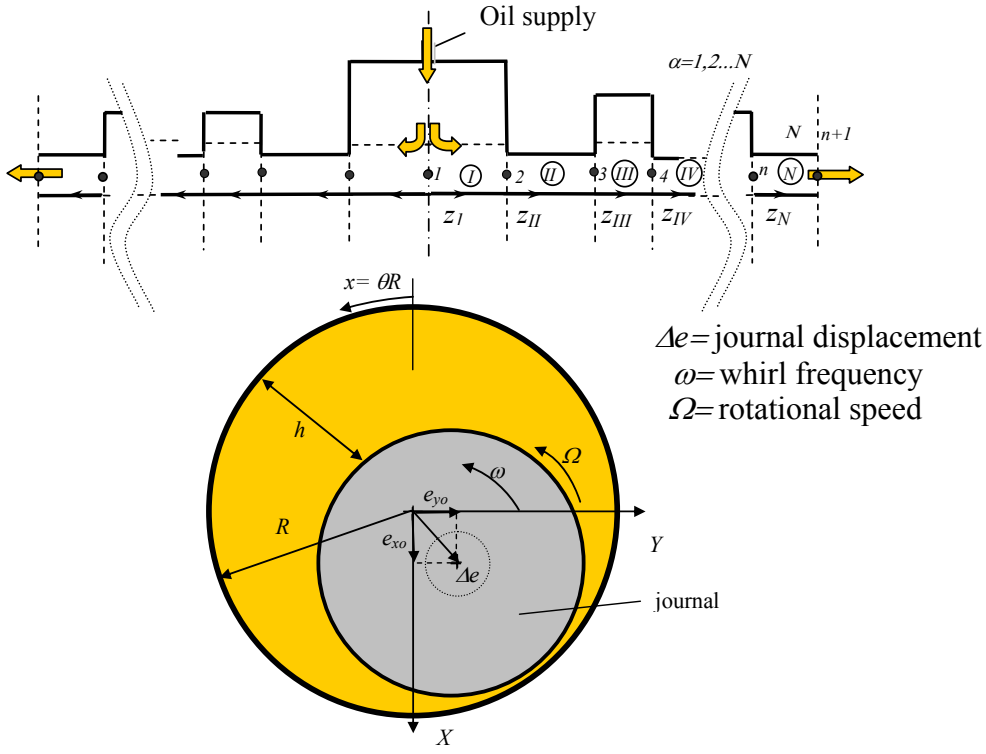

Figure 3 Schematic view of grooved annular cavity divided into flow regions and coordinate system for the analysis.

The bulk-flow continuity and moment transport equations are linear and given as [52]:

$$\frac{\partial}{\partial x}\left(\dot{q}_{x_\alpha}\right)+\frac{\partial}{\partial z_\alpha}\left(\dot{q}_{z_\alpha}\right)+\frac{\partial}{\partial t}\left(h_\alpha\right)=0 \tag{3.2}$$

$$-h_\alpha\frac{\partial P_\alpha}{\partial x}=k_x\,\frac{\mu}{h_\alpha}\left(V_{x_\alpha}-\frac{\Omega R}{2}\right)+\frac{\partial\left(\rho\,\dot{q}_{x_\alpha}\right)}{\partial t} \tag{3.3}$$

$$-h_\alpha\frac{\partial P_\alpha}{\partial z_\alpha}=k_z\,\mu\frac{V_{z_\alpha}}{h_\alpha}+\frac{\partial\left(\rho\,\dot{q}_{z_\alpha}\right)}{\partial t}\;;\qquad \alpha=I,II,\ldots N \tag{3.4}$$

with k_x=k_z=12 for laminar flow and (ρ, μ) as the lubricant density and viscosity. These equations do not included fluid advection terms since these are negligible compared to

the temporal fluid inertia terms for small amplitude motions as detailed in Refs. [7,12]. Equations (3.3) and (3.4) are written as:

$$\dot{q}_{x_\alpha} = -\frac{h_\alpha^{\,3}}{k_x \mu}\frac{\partial P_\alpha}{\partial x} - \frac{h_\alpha^{\,2}}{k_x \mu}\frac{\partial\left(\rho \dot{q}_{x_\alpha}\right)}{\partial t} + \frac{h_\alpha \Omega R}{2};$$
$$\dot{q}_{z_\alpha} = -\frac{h_\alpha^{\,3}}{k_z \mu}\frac{\partial P_\alpha}{\partial z_\alpha} - \frac{h_\alpha^{\,2}}{k_z \mu}\frac{\partial\left(\rho \dot{q}_{z_\alpha}\right)}{\partial t} \quad ; \quad \alpha = I, II, \ldots N \tag{3.5}$$

Differentiating $\dot{q}_{x_\alpha}$ with respect to *x,* and $\dot{q}_{z_\alpha}$ with respect to z_α, adding both equations and disregarding second order terms yields a Reynolds-like equation for the film pressure of an incompressible fluid [4]

$$\frac{\partial}{\partial x}\left(h_\alpha^{\,3}\frac{\partial P_\alpha}{\partial x}\right) + \frac{\partial}{\partial z_\alpha}\left(h_\alpha^{\,3}\frac{\partial P_\alpha}{\partial z_\alpha}\right) = 12\mu\frac{\partial}{\partial t}\left(h_\alpha\right) + 6\mu R\Omega\frac{\partial}{\partial x}\left(h_\alpha\right) + \left(\rho h_\alpha^{\,2}\right)\frac{\partial^2}{\partial t^2}\left(h_\alpha\right) \tag{3.6}$$
$$\alpha = I, II, \ldots N$$

A closed-form solution of the pressure field defined by Eq. (3.6) can be obtained for small journal perturbations about a centered equilibrium position. In the case of journal static off-centered operation, a finite element formulation is employed to obtain the pressure field and the resulting force coefficients also assuming small amplitude journal perturbations. Both solutions are based on the following major assumption.

3.3 Major Assumption: Effective Groove Clearance

There is abundant experimental evidence from SFD test configurations with shallow grooves (*depth* < 15*c*) confirming the generation of significant dynamic pressures in the grooves [12, 37, 38, 40]. Current predictive models [19, 23, 24, 25, 26] provide from moderate to good correlations with experimental force coefficients. However, these models show large discrepancies for either the damping [19, 26] or added mass coefficient [23, 24, 25]. In the case of relatively deep grooves, the experimental results evidence large added mass coefficients but relatively small variation of the damping coefficients [27]. Large added mass coefficients are also reported in oil seals tested in configurations with deep grooves [29], with relatively small variation of the damping

coefficients respect to predictions assuming null dynamic pressures at the grooves. In both cases, SFDs and oil seals, the added mass coefficients are largely underpredicted. In addition, in oil seals with short and shallow grooves in the film land (i.e. grooved oil seals) the force coefficients are also not accurately predicted [29, 30, 34]. Furthermore, current models predicting force coefficients in grooved seals altogether neglect fluid inertia effects.

Most of the discrepancies between experimental results and predictions of fluid film reaction forces in grooved SFDs are mainly related to the combination of different analytical treatments for the flows in the land and in the groove regions. The use of different approaches and unnecessary simplifications leads to inaccurate formulations at the groove-land interface. In the case of deep grooves, the discrepancies between predictions and experiments are simply related to assuming a null dynamic pressure at the grooves by considering the full volume of the groove in the fluid film flow analysis. In the current analysis, only a fraction of the groove volume is considered based on the fact that the laminar flow pattern at the grooves is characterized by a thru flow and a recirculation flow regions. Figure 4(a) shows a representation of the streamlines pattern for a pressure driven flow through a (symmetric) annular cavity with a supply groove and two mid-land grooves. This schematic representation shows a single vortex at the grooves. In actuality, the number and distribution of the vortices within the recirculation region depend on the geometry and flow conditions at the entrance of the groove [53]; though the only assumption made in the proposed analysis is that there are two distinctive flow regions. Figure 4(b) depicts a close-up of the streamline field obtained from CFD simulations of the pressure driven flow at the mid-land groove of the seal tested by Graviss [29] for two groove depths (10c and 15c). In this configuration not only the flow pattern at the inner-land grooves is characterized by two regions, but also the dividing streamlines for the 10c and 15c groove depths present a similar penetration depth.

In the proposed analysis, the domain for the pressure induced due to dynamic journal motions is delimited to the thru flow region. Thus, the fluid film clearance at the groove

is represented in terms of an effective clearance $c_\eta=(d_\eta+c)$, with d_η as an effective groove depth and c as the clearance of the ungrooved portion or smooth land. This assumption is complemented by the observation that, even for small effective groove clearances (i.e. $c_\eta=5c$), the damping contribution from the groove remains significantly lower than that related to the ungrooved portion since a damping coefficient is roughly proportional to $1/c_\eta^3$ [12]. On the other hand, the added mass term is proportional to $1/c_\eta$ [12]. Thus, the added mass coefficient derived from an effective groove clearance (c_η) is of the same order of magnitude at the grooves as in the film lands (i.e. ungrooved portion). The assumption substantiates experimental results evidencing that the grooves in oil seals, regardless of depth, do not isolate the pressure fields in contiguous lands [29, 30, 34]. Also, this assumption implies that the contribution of deep grooves to the fluid film forces is of inertial nature (i.e. a radial force), which is also supported by experimental findings [27]. A similar rationale can be also extended to inlet (central) deep grooves. For larger volumes there is the formation of multiple vortices, but the assumption that the domain for the perturbed flow is limited to the thru flow region remains. Figure 5 depicts a schematic view of the SFD tested in Ref. [27] and a close-up view of CFD simulations of the pressure driven streamline field in the inlet groove. Note that, although the recirculation region extends to the feed plenum, a thru flow and recirculation regions are observed at the inlet groove. As shown in Section 6, the present analysis provides an explanation to the large added mass coefficients generated in a test seal configuration with deep grooves (SFDs [27] and smooth land oil seals [29]).

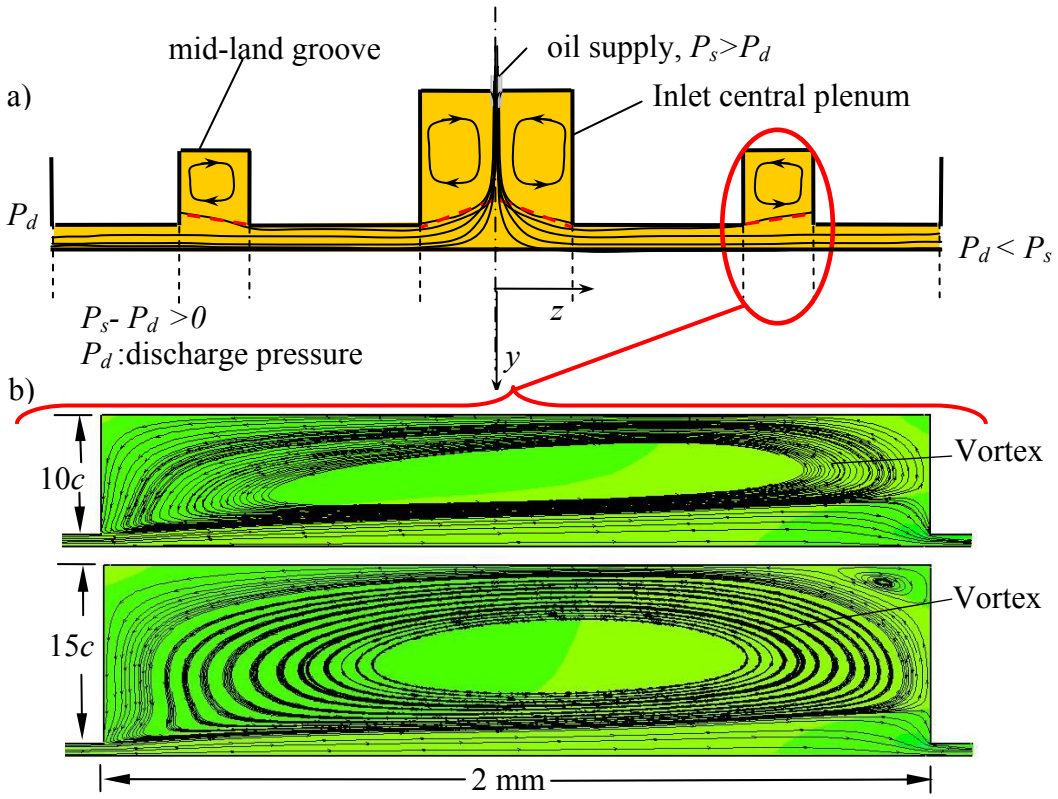

Figure 4 a) Schematic view of streamlines in axially symmetric grooved annular cavity ($\Delta P = P_s - P_d$). b) CFD simulation of pressure driven streamlines across a 10c and 15c circumferential mid-land groove in an oil seal tested in Ref. [29]. (c= 86 μm, ω=7000 RPM, D= 117 mm).

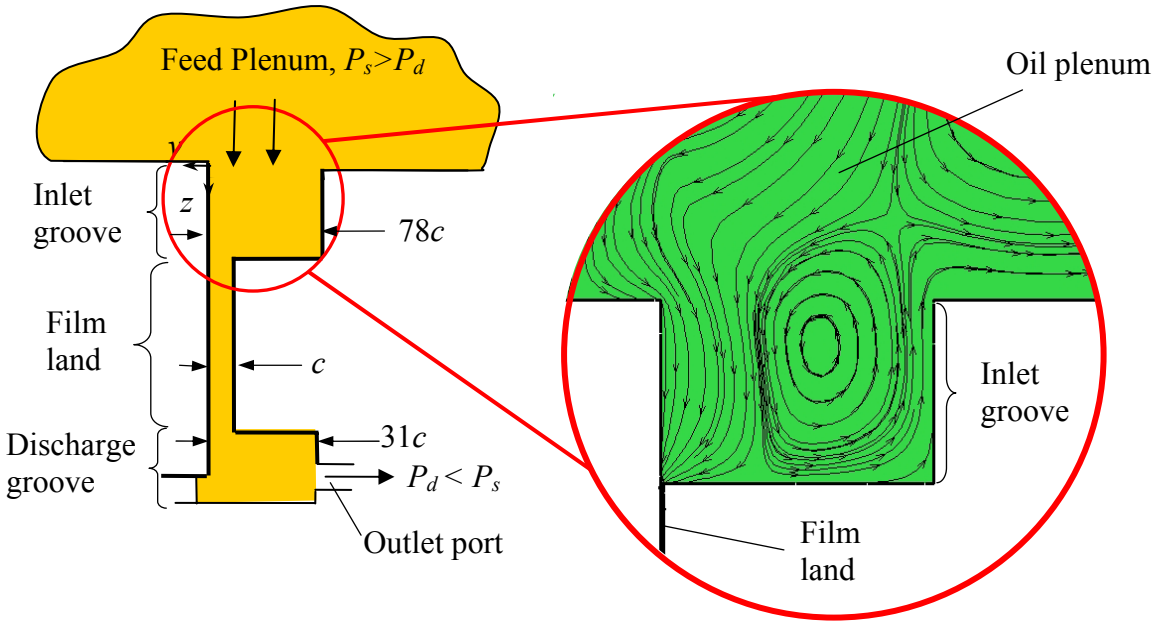

Figure 5 Schematic view of SFD tested in Ref. [27] and close-up of CFD simulation of pressure driven streamlines across the inlet groove ($\Delta P = P_s - P_d$). (c= 127 μm, D= 127 mm).

The distinction of a thru flow region and a recirculation region and their application in the analysis of grooved seals is not a novel concept. Wyssmann *et al.* [54] first included such considerations in the formulation of a two-control-volume model to analyze the flow across labyrinth seal cavities. This concept was also implemented by Florjancic [55] and Marquette [56] to formulate a three control volume theory to obtain fluid film dynamic forces in grooved liquid seals. In both references, the flow is turbulent and the streamline dividing the flow regions at the grooves is used to define control volumes.

In the present analysis, this concept is implemented in a simpler manner by using a constant depth boundary to define a single flow region. This boundary is estimated based on experimental results and may differ from the streamline dividing the through and recirculation flow regions obtained from CFD calculations. In fact, for the grooved oil seal tested by Graviss [29], the comparison of experimental and analytical results yields effective groove depths that are approximately half of the actual groove depth while the penetration depth of the streamline dividing the flow regions is approximately

1/5 of the groove depth (see Fig. 4). Interestingly, the effective groove depth of about 1/2 of the groove depth coincides with the center of the main recirculation vortices depicted in Fig. 4b. The vortex center, as illustrated with the vector field in Fig. 6, represents the boundary between the forward and backward axial flow fields (i.e. null axial velocity boundary).

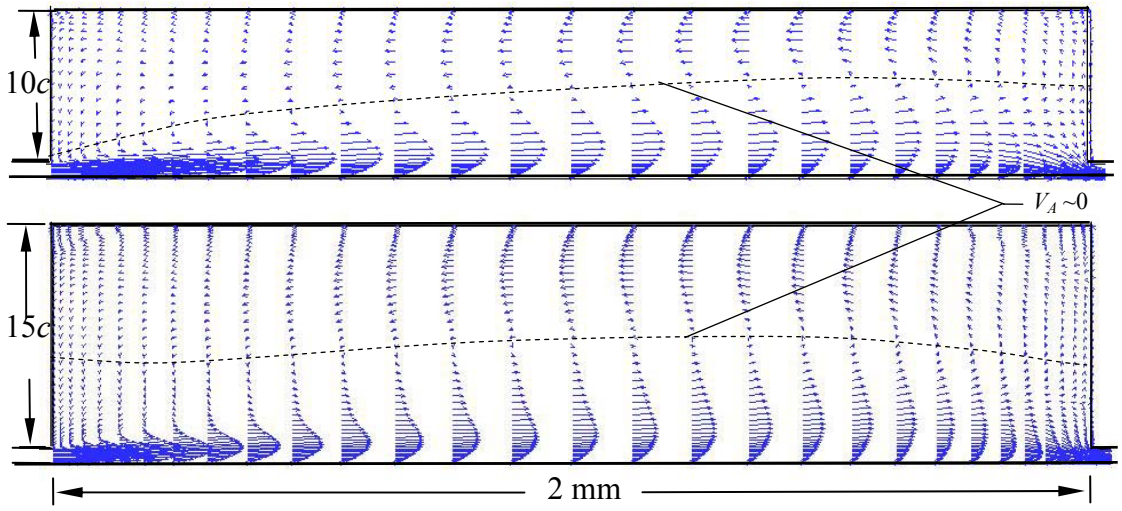

Figure 6 CFD simulation of pressure driven velocity vector field across a 10c and 15*c* circumferential mid-land groove in an oil seal tested in Ref. [29]. (*c*= 86 μm, ω=7000 RPM, D= 117 mm).

A description of the perturbation analysis and boundary conditions to obtain the pressure field and fluid film reaction forces in grooved SFDs and grooved oil seals follows.

4. FLOW ANALYSIS FOR SMALL AMPLITUDE MOTIONS ABOUT A JOURNAL CENTERED POSITION

4.1 Analysis

This section details the fluid flow analysis to obtain the dynamic pressure field and force coefficients in axially symmetric annular cavities with groove arrangements, including a central feeding groove, as shown in Fig. 7. Figure 8 depicts the journal, annular cavity geometry, and the coordinate system for small journal motions about a centered position. As explained in Section 3, the multiple groove annular cavity is divided into individual flow regions with uniform clearance. In case of a groove, its effective groove depth (d_η) replaces the actual physical groove depth. The following derivation applies to a flow region of constant clearance, and with the local coordinate system origin at the entrance of the corresponding grooved or ungrooved region.

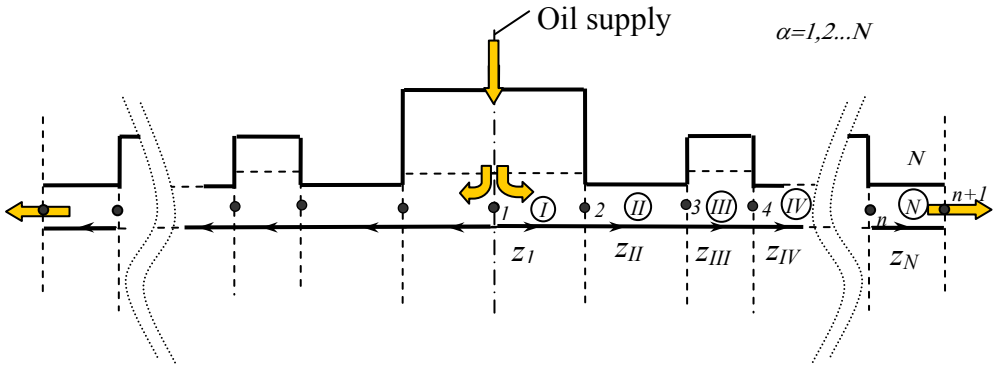

Figure 7 Schematic view of grooved annular cavity divided into flow regions.

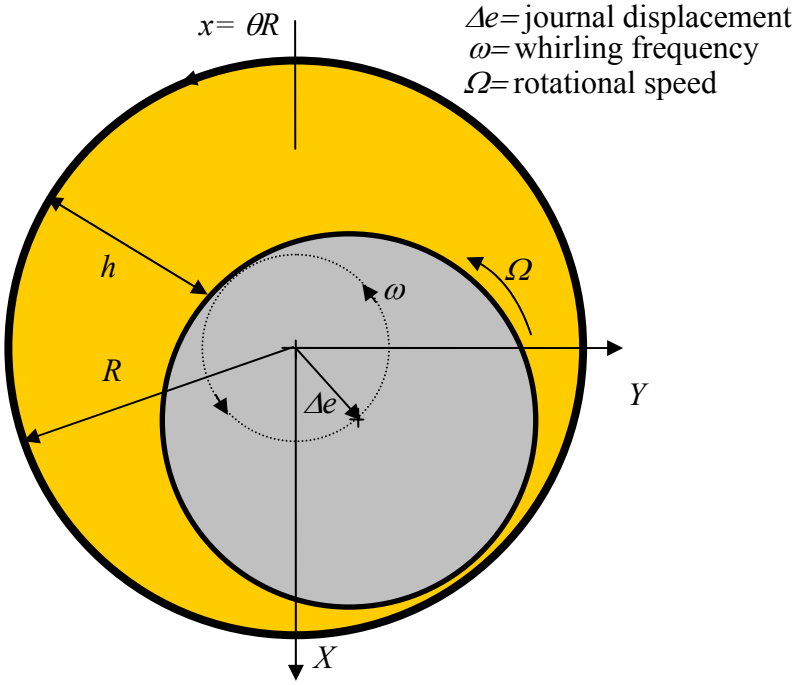

Figure 8 View of rotating and whirling journal and coordinate system for bulk-flow analysis.

The Reynolds fluid film equation presented in the previous section adds temporal inertia terms (Eq. 3.6),

$$\frac{\partial}{\partial x}\left(h_\alpha{}^3\frac{\partial P_\alpha}{\partial x}\right)+\frac{\partial}{\partial z_\alpha}\left(h_\alpha{}^3\frac{\partial P_\alpha}{\partial z_\alpha}\right)=12\,\mu\frac{\partial}{\partial t}\left(h_\alpha\right)+6\mu R\Omega\frac{\partial}{\partial x}\left(h_\alpha\right)+\left(\rho\,h_\alpha{}^2\right)\frac{\partial^2}{\partial t^2}\left(h_\alpha\right)\qquad \alpha=I,II,\ldots N \tag{3.6}$$

and is to be solved within each individual flow region for journal motions of small amplitude $(\Delta e_X\ ,\ \Delta e_Y\ ) << c_{\eta_\alpha}$ and frequency ω about the centered position. For the center journal operation condition, the film thickness (h_α) equals

$$h_\alpha = c_{\eta_\alpha} + e^{i\omega t}\ \left\{\Delta e_X h_X + \Delta e_Y\ h_Y\right\}; \Delta e_X, \Delta e_Y << c_{\eta_\alpha}, i=\sqrt{-1};\quad \alpha=I,II,\ldots N \tag{4.1}$$

with $h_X=\cos(\theta), h_Y=\sin(\theta)$. The pressure is the superposition of a zeroth order field (P_o) and a first order (dynamic) fields ($P_{X_\alpha}, P_{Y_\alpha}$)

$$P_\alpha = P_{0_\alpha} + e^{i\omega t}\ \left\{\Delta e_X\ P_{X_\alpha}\ +\ \Delta e_Y\ P_{Y_\alpha}\right\}\ ;\quad \alpha=I,II,\ldots N \tag{4.2}$$

Substitution of Eqs. (4.1) and (4.2), into Eq. (3.6) gives the zero$_{th}$ order equilibrium pressure equations

$$\frac{d^2}{d z_\alpha^{\,2}}\left(P_{0_\alpha}\right)=0 \rightarrow \quad P_{0_\alpha}=a_\alpha+s_\alpha z_\alpha \quad ; \ \alpha = I, II, \ldots N \tag{4.3}$$

since the static component of film thickness does not change along the axial or circumferential directions. Above s_α denotes the axial pressure gradient in each flow region. The first order equations for the perturbed pressure fields due to journal motions along the X and Y directions are

$$\begin{aligned}
&\frac{\partial^2 P_{X_\alpha}}{\partial x^2}+\frac{\partial^2 P_{X_\alpha}}{\partial z_\alpha^{\,2}}=12\,i\,\frac{\mu\omega}{c_{\eta_\alpha}^3}\left\{1+i\,\overline{\mathrm{Re}}_{*_\alpha}\right\}\cos(\theta)-\left\{\frac{6\mu\Omega}{c_{\eta_\alpha}^3}\right\}\sin(\theta)\\
&\frac{\partial^2 P_{Y_\alpha}}{\partial x^2}+\frac{\partial^2 P_{Y_\alpha}}{\partial z_\alpha^{\,2}}=12\,i\,\frac{\mu\omega}{c_{\eta_\alpha}^3}\left\{1+i\,\overline{\mathrm{Re}}_{*_\alpha}\right\}\sin(\theta)+\left\{\frac{6\mu\Omega}{c_{\eta_\alpha}^3}\right\}\cos(\theta) \quad ; \quad \alpha = I, II, \ldots N
\end{aligned} \tag{4.4}$$

where $\overline{\mathrm{Re}}_{*_\alpha}=\dfrac{\rho\omega c_{\eta_\alpha}^2}{12\,\mu}$ is a modified local squeeze film Reynolds number [1]. PDEs (4.4) are linear with solution

$$\begin{aligned}
&P_{X_\alpha}(z)=f_{X_{\alpha(z_\alpha)}}\cos(\theta)+g_{X_{\alpha(z_\alpha)}}\sin(\theta)\\
&P_{Y_\alpha}(z)=f_{Y_{\alpha(z_\alpha)}}\cos(\theta)+g_{Y_{\alpha(z_\alpha)}}\sin(\theta) \qquad \alpha = I, II, \ldots N
\end{aligned} \tag{4.5}$$

Replace the first of Eqs. (4.5) into the first of Eqs. (4.4) to obtain

$$\frac{d^2 f_{X_\alpha}}{d z^2}-\frac{f_{X_\alpha}}{R^2}=12\,i\,\frac{\mu\omega}{c_{\eta_\alpha}^3}\left\{1+i\,\overline{\mathrm{Re}_{*_\alpha}}\right\}; \ \frac{d^2 g_{X_\alpha}}{d z^2}-\frac{g_{X_\alpha}}{R^2}=-\frac{6\mu\Omega}{c_{\eta_\alpha}^3} \quad ; \quad \alpha = I, II, \ldots N \tag{4.6}$$

whose solution are $f_{X_{\alpha(z_\alpha)}}=f_{X_{H_\alpha(z_\alpha)}}+f_{X_{P_\alpha}}$ and $g_{X_{\alpha(z_\alpha)}}=g_{X_{H_\alpha(z_\alpha)}}+g_{X_{P_\alpha}}$. The particular and homogenous solutions are

[1] The equations show that fluid inertia effects are of importance for Re_{*_α} >1.

$$f_{X_{P_\alpha}} = -12\,i\,\frac{\mu\,\omega\,R^2}{c_{\eta_\alpha}^3}\left\{1 + i\,\overline{\mathrm{Re}}_{*_\alpha}\right\} \quad ; \quad g_{X_{P_\alpha}} = -\frac{6\mu\Omega R^2}{c_{\eta_\alpha}^3} \tag{4.7}$$

$$\begin{Bmatrix} f_{X_{H_\alpha}}(z_\alpha) \\ g_{X_{H_\alpha}}(z_\alpha) \end{Bmatrix} = \begin{Bmatrix} c_{f_\alpha} \\ c_{g_\alpha} \end{Bmatrix} \cosh\left(-z_\alpha / R\right) + \begin{Bmatrix} s_{f_\alpha} \\ s_{g_\alpha} \end{Bmatrix} \sinh\left(z_\alpha / R\right); \qquad \alpha = I, II, \ldots N \tag{4.8}$$

The evaluation of P_{Y_α} is similar. The analysis shows that $g_{Y_\alpha} = f_{X_\alpha}$; $f_{Y_\alpha} = -g_{X_\alpha}$. For evaluation of boundary conditions at the interfaces between adjacent flow regions, axial flow rates are needed. Hence, let $\dot{q}_{z_\alpha} = \dot{q}_{z_{0_\alpha}} + e^{i\omega t}\left\{\Delta e_X\ \dot{q}_{z_{X_\alpha}} + \Delta e_Y\ \dot{q}_{z_{Y_\alpha}}\right\}$, and from Eqs. (3.5), the first order axial flow rates are

$$\begin{aligned} \dot{q}_{z_{X_\alpha}}\left(1 + i\,\overline{\mathrm{Re}}_{*_\alpha}\right) &= -\frac{c_{\eta_\alpha}^3}{12\,\mu}\frac{\partial P_{X_\alpha}}{\partial z_\alpha} - \frac{3\,c_{\eta_\alpha}^2\cos(\theta)}{12\,\mu}\ s_\alpha \\ \dot{q}_{z_{Y_\alpha}}\left(1 + i\,\overline{\mathrm{Re}}_{*_\alpha}\right) &= -\frac{c_{\eta_\alpha}^3}{12\,\mu}\frac{\partial P_{Y_\alpha}}{\partial z_\alpha} - \frac{3\,c_{\eta_\alpha}^2\sin(\theta)}{12\,\mu}\ s_\alpha \end{aligned} \tag{4.9}$$

Note that for journal motions along the *X*-direction,

$$\dot{q}_{z_{X_\alpha}}\left(1 + i\,\overline{\mathrm{Re}}_{*_\alpha}\right) = -\frac{c_{\eta_\alpha}^3}{12\,\mu}\left[\frac{df_{X_\alpha}}{dz_\alpha}\cos(\theta) + \frac{dg_{X_\alpha}}{dz_\alpha}\sin(\theta)\right] - \frac{3\,c_{\eta_\alpha}^2\cos(\theta)}{12\,\mu}\ s_\alpha;\ \alpha = I, II, \ldots N \tag{4.10}$$

A similar expression follows for $\dot{q}_{z_{Y_\alpha}}$.

4.2 Boundary Conditions

The pressure field must be single-valued[2] and the axial flow rates leaving one region and entering the next must be equal. Application of these conditions at the interface groove-film land, and given specified pressure (or flow) at the inlet and exit planes of the whole flow region leads to a set of algebraic equations for determination of the coefficients $(c_{f_\alpha}, c_{g_\alpha}, s_{f_\alpha}, s_{g_\alpha})_{\alpha=I,II,..N}$ Specified supply (inlet) and discharge pressures (P_I,

[2] At the edge of a groove-land region no fluid inertia pressure drop or rise are accounted for. This oversimplification is acceptable for laminar flow conditions (low whirl frequencies).

P_{n+1}) easily determine the static pressure fields, see Eq.(4.3), and $s_\alpha = \frac{dP_\alpha}{dz_\alpha}$. The boundary and interface conditions for the dynamic pressure field (P_{X_α}) are:

a) Due to geometrical symmetry, the axial flow rate must be null at $z_1=0$ (groove middle plane). Hence, from Eq. (4.9), $s_{g_1} = 0$. This boundary condition, also implemented in Refs [18, 40], supports the experimental findings in Ref. [40] as it implies a non-zero dynamic pressure at the groove middle plane[3].

b) The last (N) flow region exits to ambient pressure $\left(P_{0_N}\Big|_{z_N=L_N}=0\right)$; and thus there is no generation of dynamic pressure at $z_N=L_N$. Thus,

$$P_{X_N}\Big|_{z_N=L_N}=0=f_{x_N}(L_N)\cos(\theta)+g_{x_N}(L_N)\sin(\theta) \tag{4.11}$$

Since the sine and cosine functions are linearly independent, then it follows

$$\begin{aligned} &c_{f_N}\cosh\left(L_N/R\right)+s_{f_N}\sinh\left(L_N/R\right)=F_N \;;\; F_N=12\,i\,\frac{\mu\,\omega\,R^2}{c_{\eta_N}{}^3} \\ &c_{g_N}\cosh\left(L_N/R\right)+s_{g_N}\sinh\left(L_N/R\right)=G_N \;;\; G_N=-\frac{6\mu\Omega R^2}{c_{\eta_N}{}^3} \end{aligned} \tag{4.12}$$

c) At the interface groove and land, he first-order pressures and axial flow rates must be equal, i.e.

$$\begin{aligned} &P_{X_\alpha}\Big|_{z_\alpha=L_\alpha}=P_{X_{\alpha+1}}\Big|_{z_{\alpha+1}=0};\alpha=1\ldots N-1 \\ &\rightarrow\quad f_{X_\alpha}(L_\alpha)=f_{X_{\alpha+1}}(0);\;\; g_{X_\alpha}(L_\alpha)=g_{X_{\alpha+1}}(0) \end{aligned} \tag{4.13}$$

$$\begin{aligned} &\dot{q}_{z_{X_\alpha}}\left(1+i\,\overline{\mathrm{Re}}_{*_\alpha}\right)\Big|_{z_\alpha=L_\alpha}=\dot{q}_{z_{X_{\alpha+1}}}\left(1+i\,\overline{\mathrm{Re}}_{*_{\alpha+1}}\right)\Big|_{z_{\alpha+1}=0};\quad \alpha=1\ldots N-1 \\ &\rightarrow\frac{c_{\eta_\alpha}^3}{R}\left[c_{f_\alpha}\sinh\left(L_\alpha/R\right)+s_{f_\alpha}\cosh\left(L_\alpha/R\right)\right]-\frac{c_{\eta_{\alpha+1}}^3}{R}\left[s_{f_{\alpha+1}}\right]=-3\,c_{\eta_\alpha}^2\,s_\alpha+3c_{\eta_{\alpha+1}}^2\,s_{\alpha+1} \\ &\frac{c_{\eta_\alpha}^3}{R}\left[c_{g_\alpha}\sinh\left(L_\alpha/R\right)+s_{g_\alpha}\cosh\left(L_\alpha/R\right)\right]-\frac{c_{\eta_{\alpha+1}}^3}{R}\left[s_{g_{\alpha+1}}\right]=0 \end{aligned} \tag{4.14}$$

[3] Importantly enough, measurements in Ref. [29] showing no significant dynamic pressure oscillations at the inlet groove are not an exception nor are in conflict with the proposed model. As detailed in Section 6, the seemingly null magnitudes of dynamic pressure measurements are related to the test conditions and to the inertial nature of the pressure field within the groove.

Integration of the first-order pressure fields around the journal surface renders the fluid film reaction forces

$$\begin{Bmatrix} F_X \\ F_Y \end{Bmatrix} = 2\sum_{\alpha=1}^{N} \int_0^{L_\alpha} \int_0^{2\pi R} \left\{ \left[e^{i\omega t} \left\{ \Delta e_X \; P_{X_\alpha} + \Delta e_Y \; P_{Y_\alpha} \right\} \right] \begin{Bmatrix} \cos(\theta) \\ \sin(\theta) \end{Bmatrix} dx \right\} dz_\alpha \tag{4.15}$$

These forces are expressed in terms of stiffness (*K),* damping *(C),* and inertia (*M*) force coefficients, i.e.

$$\begin{Bmatrix} F_X \\ F_Y \end{Bmatrix} = -\begin{bmatrix} K_{XX} - \omega^2 M_{XX} + i\omega C_{XX} & K_{XY} - \omega^2 M_{XY} + i\omega C_{XY} \\ K_{YX} - \omega^2 M_{YX} + i\omega C_{YX} & K_{YY} - \omega^2 M_{YY} + i\omega C_{YY} \end{bmatrix} \begin{Bmatrix} \Delta e_X \\ \Delta e_Y \end{Bmatrix} \tag{4.16}$$

where,

$$-\begin{bmatrix} K_{XX} - \omega^2 M_{XX} + i\omega C_{XX} \\ K_{YX} - \omega^2 M_{YX} + i\omega C_{YX} \end{bmatrix} = 2\sum_{\alpha=1}^{N} \int_0^{L_\alpha} \int_0^{2\pi R} \left\{ \begin{Bmatrix} f_{X_\alpha(z_\alpha)} \cos(\theta)^2 \\ g_{X_\alpha(z_\alpha)} \sin(\theta)^2 \end{Bmatrix} dx \right\} dz_\alpha = 2\pi R \sum_{\alpha=1}^{N} \int_0^{(z_\alpha)} \begin{Bmatrix} f_{X_\alpha} \\ g_{X_\alpha} \end{Bmatrix} dz_\alpha$$

(4.17)

Note that $K_{YY} = K_{XX}$, $C_{YY} = C_{XX}$, $K_{XY} = -K_{YX}$ for motions about the center of the bearing or seal.

The next two sections illustrate the system of equations to determine the force coefficients of a single-land SFD and an oil seal (two lands separated by a central grove). The force coefficients obtained from the open ends SFD reproduce well known formulas derived by Reinhart and Lund [4].

4.3 Case I: SFD-Classical Solution

Figure 9 presents a schematic view of a single SFD land extending from $-L/2 \le z \le L/2$. Both ends are exposed to ambient pressure, and there is no static axial pressure drop.

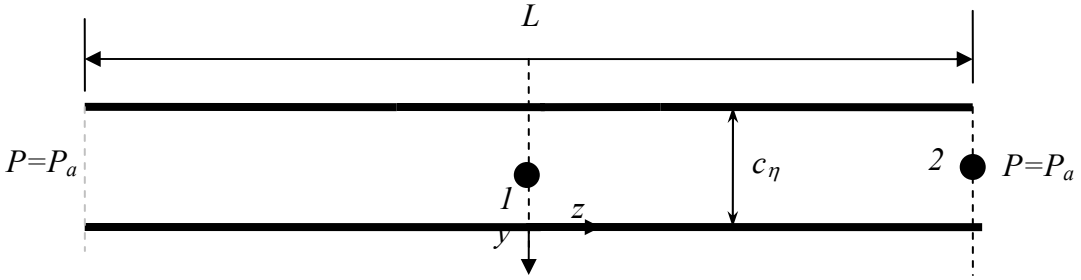

Figure 9 Schematic view of a simple SFD and boundary conditions.

The first order pressure fields must be symmetric about *z=0;* hence, the hyperbolic sine terms disappear in Eq. (4.8), i.e. s_f=s_g=0. Thus, for motion perturbations along the x direction

$$f_X(z) = c_{f_X} \cosh\left(z/R\right) + f_{X_P}\,; \quad g_X(z) = c_{g_X} \cosh\left(z/R\right) \tag{4.18}$$

At the ends the pressure is ambient (P_a), and thus the dynamic pressure is set to zero at both ends, hence

$$P_X\big|_{z=\frac{L}{2}} = f_X\left(\frac{L}{D}\right) = 0; \rightarrow \; c_f = \frac{-f_{X_P}}{\cosh\left(L/D\right)}; \; c_g = 0 \tag{4.19}$$

with f_{X_P} defined in Eq.(4.7). Integrating the pressure across the damper land

$$K_{XX} - \omega^2 M_{XX} + \mathrm{i}\omega C_{XX} = -\pi R \int_{-L/2}^{L/2} f(z)\,dz = -f_P \pi R L \left[1 - \frac{\tanh\left(L/D\right)}{\left(L/D\right)}\right] \tag{4.20}$$

yields the force coefficients

$$\begin{aligned} C_{XX} &= 12\pi \frac{\mu R^3 L}{c^3} \left[1 - \frac{\tanh\left(L/D\right)}{\left(L/D\right)}\right] \\ K_{XX} &= 0; \quad M_{XX} = \pi \frac{\rho R^3 L}{c} \left[1 - \frac{\tanh\left(L/D\right)}{\left(L/D\right)}\right] \end{aligned} \tag{4.21}$$

which coincide with the classical damping and inertia force coefficients derived by Reinhart and Lund [4].

4.4 Case II: Oil Seal-Two Lands Separated by a Central Groove

Figure 10 shows a schematic view of two thin film lands separated by a central groove. The analysis considers only half of the system due to its geometrical symmetry. The system is divided into ½ groove and land section of lengths L_1 and L_2, respectively. The clearance at the land is $c_L=c$, and at the groove section is $c_G=(d_\eta+c)$, where d_η is the effective groove depth.

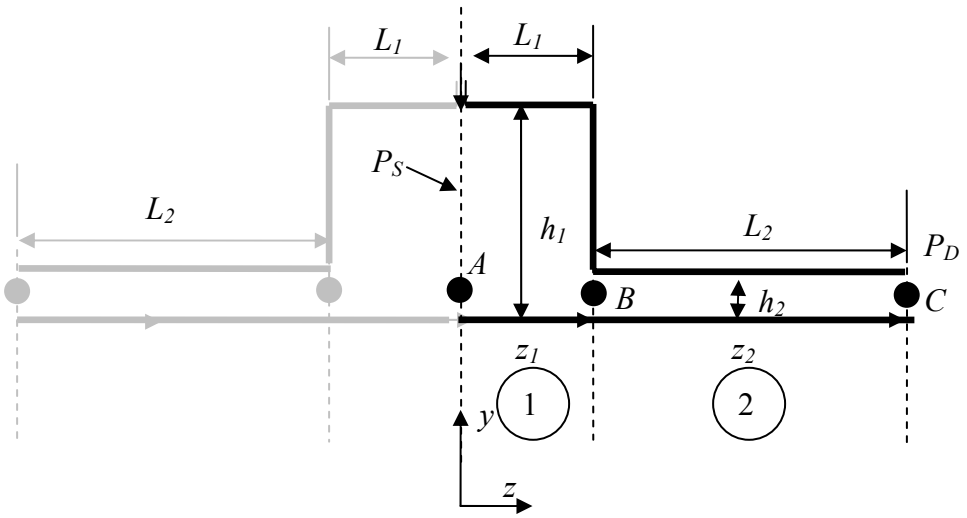

Figure 10 Schematic view of two film lands separated by a central groove.

A static pressure (P_s) is specified at the middle plane, while the pressure is ambient at the discharge planes ($P_D = P_a$). The equations for static pressure fields across the groove and land lengths are

$$P_{0_1}(z_1)=P_S\left(1-\frac{z_1}{L_1}\right)+P_E\left(\frac{z_1}{L_1}\right);\ P_{0_2}(z_2)=P_E\left(1-\frac{z_2}{L_2}\right)+P_a\left(\frac{z_2}{L_2}\right) \tag{4.22}$$

where P_E, the pressure at the groove-land interface, is determined from matching axial flow rates, i.e.

$$P_E = \frac{P_S + P_a\left(\frac{L_1}{L_2}\right)\left(\frac{c_L}{c_G}\right)^3}{1+\left(\frac{L_1}{L_2}\right)\left(\frac{c_L}{c_G}\right)^3} \tag{4.23}$$

Note that if $c_L << c_G$ then, $P_E \sim P_S$. The analysis shows that the coefficients of the first order pressure fields, here grouped as $\mathbf{f} = \left\{c_{f_1} \quad s_{f_1} \quad c_{f_2} \quad s_{f_2}\right\}^T$; $\mathbf{g} = \left\{c_{g_1} \quad s_{g_1} \quad c_{g_2} \quad s_{g_2}\right\}$ are determined from solution of the algebraic system of equations:

$$[\mathbf{H}][\mathbf{f} \mid \mathbf{g}] = [\mathbf{F} \mid \mathbf{G}] \tag{4.24}$$

where

$$\mathbf{H} = \begin{pmatrix} \cosh\left(\frac{L_1}{R}\right) & \sinh\left(\frac{L_1}{R}\right) & -1 & 0 \\ 0 & 0 & \cosh\left(\frac{L_2}{R}\right) & \sinh\left(\frac{L_2}{R}\right) \\ c_G{}^3 \sinh\left(\frac{L_1}{R}\right) & c_G{}^3 \cosh\left(\frac{L_1}{R}\right) & 0 & -c_L{}^3 \\ 0 & 1 & 0 & 0 \end{pmatrix} \tag{4.25}$$

and

$$\mathbf{F} = \begin{pmatrix} F_G - F_L \\ F_L \\ 3Rc_L{}^2 s_L - 3Rc_G{}^2 s_G \\ -\frac{3s_G R}{c_G} \end{pmatrix}; \quad \mathbf{G} = \begin{pmatrix} G_L - G_G \\ G_L \\ 0 \\ 0 \end{pmatrix}; \; s_G = \frac{\left(P_E - P_S\right)}{L_1}; \quad s_L = \frac{\left(P_a - P_E\right)}{L_2} \tag{4.26}$$

with

$$F_\beta = -12\,i\,\frac{\mu\,\omega R^2}{c_\beta^3}\left(1 + i\,\mathrm{Re}^*_{s_\beta}\right), \quad G_\beta = 6\,\frac{\mu\Omega R^2}{c_L^3}; \quad \beta = L, G \tag{4.27}$$

Once the coefficients of the pressure function are obtained, the resulting force coefficients are obtained from integrating the pressure function, as shown in Eq. (4.17).

5. FLOW ANALYSIS FOR SMALL AMPLITUDE MOTION ABOUT A JOURNAL OFF-CENTERED POSITION

5.1 Analysis

Similar to the previous sections, the following derivation applies to multiple groove cavities and the flow domain is divided into flow region with constant clearance as shown in Fig. 7. Presently, the analysis contemplates small amplitude motion of the journal about an off-centered or eccentric operation. Figure 11 depicts the journal, annular cavity geometry, and the coordinate system used in the analysis for small amplitude journal motions about an off-centered position.

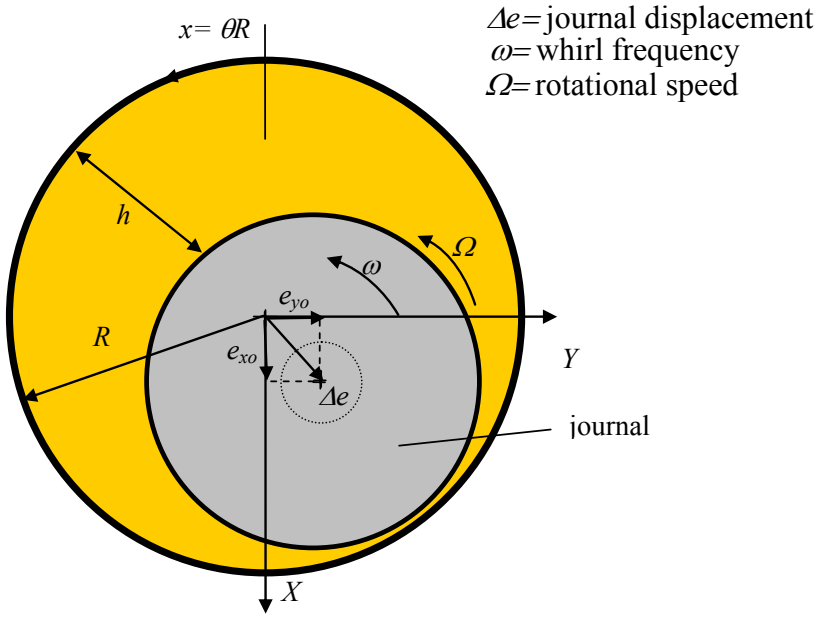

Figure 11 View of rotating and whirling journal and coordinate system for bulk-flow analysis.

Starting from the fluid film equation presented in Section 3,

$$\frac{\partial}{\partial x}\left(h_\alpha^{\,3}\frac{\partial P_\alpha}{\partial x}\right)+\frac{\partial}{\partial z_\alpha}\left(h_\alpha^{\,3}\frac{\partial P_\alpha}{\partial z_\alpha}\right)=12\,\mu\frac{\partial}{\partial t}\left(h_\alpha\right)+6\mu R\Omega\frac{\partial}{\partial x}\left(h_\alpha\right)+\left(\rho\,h_\alpha^{\,2}\right)\frac{\partial^2}{\partial t^2}\left(h_\alpha\right) \qquad (3.6)$$

$$\alpha = I, II, \ldots N$$

the film thickness *(h_α),* for small amplitude journal motions *(Δe_X , Δe_Y)*<< c_{η_α} and frequency ω about an static position (e_{Xo}, e_{Yo}), equals [1]

$$h_\alpha = h_{0_\alpha} + e^{i\omega t}\ \{\ \Delta e_X\ \cos(\theta) + \Delta e_Y \sin(\theta)\} = h_{0_\alpha} + e^{i\omega t}\ \Delta e_\sigma h_\sigma;\ \ i = \sqrt{-1};\ \sigma = X, Y \quad \alpha = I, II, \ldots N \tag{5.1}$$

with

$$h_{0_\alpha} = c_{\eta_\alpha} + e_X \cos(\theta) + e_Y \sin(\theta) = c_{\eta_\alpha} + e_{\sigma_0} h_\sigma;\ \ h_X = \cos(\theta), h_Y = \sin(\theta) \tag{5.2}$$

and c_{η_α} as the effective clearance, defined as $c_\eta = c + d_\eta$ over the grooved flow regions with d_η as the effective groove depth, and $c_{\eta_\alpha} = c$ for ungrooved (seal land) flow regions. Similarly, as in the previous section, the pressure is expressed as a superposition of a zeroth order field (P_o) and first order (dynamic) fields ($P_{X_\alpha}, P_{Y_\alpha}$)

$$P_\alpha = P_{0_\alpha} + \Delta e_\sigma\ P_{\sigma_\alpha}\ e^{i\omega t}\ \ ;\ \ \alpha = I, II, \ldots N \tag{5.3}$$

Substitution of Eqs. (5.1) and (5.3), into Eq. (3.6) gives the zero$_{th}$ order equations for the equilibrium pressure

$$\frac{\partial}{\partial x}\left(h_{0_\alpha}^{\,3} \frac{\partial P_{0_\alpha}}{\partial x} \right) + \frac{\partial}{\partial z_\alpha}\left(h_{0_\alpha}^{\,3} \frac{\partial P_{0_\alpha}}{\partial z_\alpha} \right) = 6\mu R\Omega \frac{\partial}{\partial x}\left(h_{0_\alpha} \right)\ ;\ \ \alpha = I, II, \ldots N \tag{5.4}$$

and the first order equations for journal dynamic displacements along the X and Y directions

$$\frac{\partial}{\partial x}\left(h_\alpha^{\,3} \frac{\partial P_{\sigma_\alpha}}{\partial x} \right) + \frac{\partial}{\partial z_\alpha}\left(h_\alpha^{\,3} \frac{\partial P_{\sigma_\alpha}}{\partial z_\alpha} \right) = 12 i \mu \omega \left\{ 1 + i \overline{\mathrm{Re}}_{*_\alpha} \right\} h_\sigma + 6\mu\Omega R \frac{dh_\sigma}{dx} - \frac{\partial}{\partial x}\left(3 h_{0_\alpha}^{\,2} h_\sigma \frac{\partial P_{0_\alpha}}{\partial x} \right) - \frac{\partial}{\partial z}\left(3 h_{0_\alpha}^{\,2} h_\sigma \frac{\partial P_{0_\alpha}}{\partial z} \right);\quad \sigma = X, Y; \alpha = I, II, \ldots N \tag{5.5}$$

where $\overline{\mathrm{Re}}_{*_\alpha} = \dfrac{\rho\omega c_{\eta_\alpha}^2}{12\mu}$ is a local squeeze film Reynolds number. Once the first order pressure fields (Eq. (5.4) and Eq. (5.5)) are obtained, the fluid film reaction forces at the given static journal position (e_{Xo}, e_{Yo}) are

$$F_{\sigma 0} = \sum_{\alpha=1}^{N} \int_{0}^{L_\alpha} \int_{\theta} h_\sigma P_{0_\alpha} R \, d\theta dz_\alpha ; \quad _{\sigma=X,Y;} \tag{5.6}$$

and force coefficients are also obtained by integrating the dynamic pressure fields over the flow domain [1],

$$K_{\sigma\beta_\alpha} - \omega^2 M_{\sigma\beta_\alpha} + i\omega C_{\sigma\beta_\alpha} = -\sum_{\alpha=1}^{N} \int_{0}^{L_\alpha} \int_{\theta} h_\sigma \, P_{\beta_\alpha} R \, d\theta dz_\alpha ; _{\sigma,\beta=X,Y} \; ; h_X = \cos(\theta), h_Y = \sin(\theta) \quad _{\alpha = I, II, \ldots N} \tag{5.7}$$

5.2 Finite Element Formulation

The procedure implemented for solving the PDEs (5.4, 5.5) on a grooved seal with the finite element method (FEM) is similar to that presented in Ref. [57, 58]. The implementation of the current development into a FORTRAN® code follows from modifying an existing code that predicts force coefficient for smooth land seals or journal bearings without fluid inertia effects [59]. In addition, Appendix A presents a Microsoft Excel® user interface developed for integrating the present formulation into the XLTRC2® rotordynamic software[5]. Without loss of generality, the solution is presented for a symmetric oil seal with an inlet plenum and a single mid-land groove similar to the seal tested in Ref. [29]. A similar solution can be applied to multi-groove seals.

Following the discretization of the domain into elements (Ω^e), as shown in Fig. 12, the static and dynamic pressure fields are represented as the linear combination of nodal values $\overline{P}_i^e$ within each element as

$$P_0^e = \sum_{i=1}^{n_{pe}} \Psi_i \overline{P}_{0_i}^{\,e} \; , \; P_\sigma^e = \sum_{i=1}^{n_{pe}} \Psi_i \overline{P}_{\sigma_i}^{\,e} \; ; \quad _{\sigma=X,Y} \tag{5.8}$$

[5] XLTRC2® is a rotordynamic software suite only available to members of the Turbomachinery Research Consortium (TRC).

where ψ^e are bilinear interpolation functions. The equation to be solved for each element follows from the representation of the fluid differential equations (Eq. (5.4), Eq. (5.5)) in its variational or weak form [58] using the interpolation functions as weight functions.

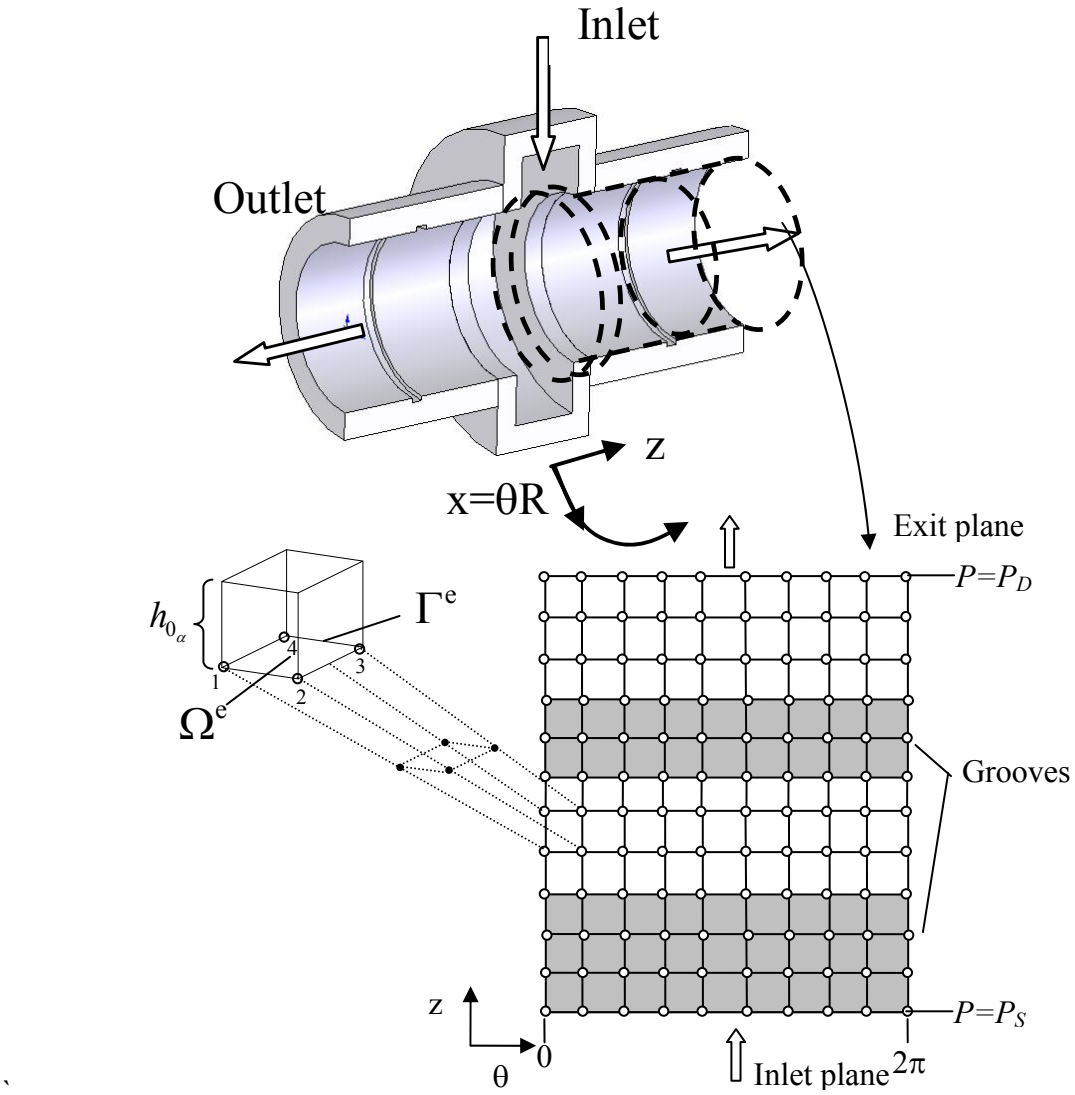

Figure 12 Coordinate system and sample mesh for oil seal FEM computational code.

The variational form of Eq. (5.4) for the zeroth order pressure yields

$$\sum_{j=1}^{n_{pe}} k_{ij}^{e} \overline{P}_{0_j}^{e} = -q_{0_i}^{e} + f_{0_i}^{e} \tag{5.9}$$

with

$$k_{ij}^{e} = \iint_{\Omega^e} \left(\frac{h_{0_\alpha}^3}{12\mu} \right)^e \left\{ \frac{\partial \Psi_i}{\partial x} \frac{\partial \Psi_j}{\partial x} + \frac{\partial \Psi_i}{\partial z} \frac{\partial \Psi_j}{\partial z} \right\}^e dx\, dz \tag{5.10}$$

$$f_{0_i}^{e} = \frac{\Omega R}{2} \iint_{\Omega^e} h_{0_\alpha} \frac{\partial \Psi_i^e}{\partial x}\, dx\, dz \tag{5.11}$$

$$q_{0_i}^{e} = \oint_{\Gamma^e} \Psi_i^e q_{n_0} d\Gamma^e \;\; ; \;\; \text{with} \;\; q_{n_0} = -\frac{h_{0_\alpha}^3}{12\mu} \frac{\partial P_0}{\partial n} + \frac{h_{0_\alpha} \Omega R}{2} n_x \tag{5.12}$$

Similarly for the first order perturbed pressure fields, P_X and P_Y, the set of equations for the nodal pressures in a finite element are

$$\sum_{j=1}^{n_{pe}} k_{ij}^{e} \overline{P}_{\sigma_j}^{e} = f_{\sigma_i}^{e} - \sum_{j=1}^{n_{pe}} S_{\sigma_{ij}}^{e} \overline{P}_{0_j}^{e} - q_{\sigma_i}^{e} \;\; ; \;\; \sigma = X, Y \tag{5.13}$$

where

$$f_{\sigma_i}^{e} = \iint_{\Omega^e} h_\sigma \left[\frac{\Omega R}{2} \frac{\partial \Psi_i^e}{\partial x} + \frac{\rho \omega^2}{12\mu} \Psi_i^e \; h_{0_\alpha}^2 \right] dx\, dz \;\; - \mathbf{i}\, \omega \iint_{\Omega^e} h_\sigma \left[\Psi_i^e \right] dx\, dz \tag{5.14}$$

$$S_{\sigma_{ij}}^{e} = \iint_{\Omega^e} \left(\frac{3 h_{0_\alpha}^2}{12\mu} \right)^e \left\{ \frac{\partial \Psi_i}{\partial x} \frac{\partial \Psi_j}{\partial x} + \frac{\partial \Psi_i}{\partial z} \frac{\partial \Psi_j}{\partial z} \right\}^e h_\sigma \; dx\, dz \tag{5.15}$$

$$q_{\sigma_i}^{e} = \oint_{\Gamma^e} \Psi_i^e q_{n_\sigma} d\Gamma^e ; \;\; q_{n_\sigma} = \left(-\frac{h_{0_\alpha}^3}{12\mu} \frac{\partial P_\sigma}{\partial n} - \frac{3 h_{0_\alpha}^2}{12\mu} h_\sigma \frac{\partial P_0}{\partial n} \right) + \frac{\Omega R}{2} h_\sigma \, n_x \tag{5.16}$$

with $\vec{n}$ as the normal vector to the boundary Γ^e of an element. Note that Eq. (5.14) includes the temporal fluid inertia term (second term in first integral). The integrals in Eq. (5.10) through Eq. (5.16) are evaluated numerically over a master element ($\hat{\Omega}$) with

normalized coordinates (isoparametric element). Reddy and Gartling [60] detail the coordinate transformation and numerical integration procedure using Gauss-Legendre quadrature formulas.

Equations (5.9) and (5.13), for each element of the flow domain, are assembled to form a linear system of equations represented as

$$\begin{aligned} &\left[k\right]_{Global}\left\{\bar{P}_0\right\}_{Global}=\left\{Q_\gamma\right\}_{Global}+\left\{F_\gamma\right\}_{Global} \quad ; \quad \gamma:0 \\ &\left[k\right]_{Global}\left\{\bar{P}_\gamma\right\}_{Global}=\left\{Q_\gamma\right\}_{Global}+\left\{F_\gamma\right\}_{Global}+\left[S\right]_{Global}\left\{\bar{P}_0\right\}_{Global} \; ; \; \gamma:X,Y \end{aligned} \tag{5.17}$$

where

$$\left[k\right]_{Global}=\bigcup_{e=1}^{Nem}\left[k\right]^e,\ \left\{Q_\gamma\right\}_{Global}=\bigcup_{e=1}^{Nem}\left\{q_\gamma\right\}^e,\ \left\{F_\gamma\right\}_{Global}=\bigcup_{e=1}^{Nem}\left\{f_\gamma\right\}^e,\ \gamma{:}0,X,Y. \tag{5.18}$$

The resulting global fluidity matrix $\left[k\right]_{Global}$ is symmetric and can be easily decomposed into its upper and lower triangular form, i.e.

$$\left[k\right]_G=\left[L\right]_G\left[U\right]_G=\left[L\right]_G\left[L\right]_G^T \tag{5.19}$$

Thus, once the **L, L**^{T} and **F** matrices are obtained, and defining the pressure at the inlet and the exit of the flow domain, a process of back- and forward-substitutions renders the discrete zeroth order pressure field $\left\{\bar{P}_0\right\}_G$. Using the results from the fluidity matrix and the zeroth order pressure field, the first order pressure field, $\left\{\bar{P}_\gamma\right\}_G$, are obtained. As in the previous case for journal centered operation, the selection of the appropriate boundary conditions, based on the physics of the problem, is essential for obtaining the force coefficients in the grooved seal geometry.

5.2.1 Boundary Conditions

Figure 13 shows the mesh for the flow domain on an oil seal with an inlet plenum and an inner groove, and the nodes of interest to enforce boundary conditions. For the studied flow domain the boundary conditions are:

Both the zeroth and first order fields are periodic in the circumferential direction

$$\bar{P}_{\gamma}(\theta,z)=\bar{P}_{\gamma}(\theta+2\pi,z);\ \gamma=0,x,y \tag{5.20}$$

The fluid pressure must be greater than the lubricant cavitation pressure (P_{cav}=0). In the occurrence of oil cavitation, the zeroth and dynamic pressure field vanishes.

Equations (5.12) and (5.16) automatically satisfy the flow continuity at boundary between smooth land and groove, for example.

5.2.1.1 Zeroth Order Pressure Field

A) Constant static pressure at inlet plane (z= *0*). This condition is set to the lower nodes of an element along the inlet plane.

$$\bar{P}_0^e\big|_{z=0}=P_S \tag{5.21}$$

B) Constant static pressure at exit plane (z= L). This condition is set to the upper nodes of an element along the exit plane.

$$\bar{P}_0^e\big|_{z=L}=P_D \tag{5.22}$$

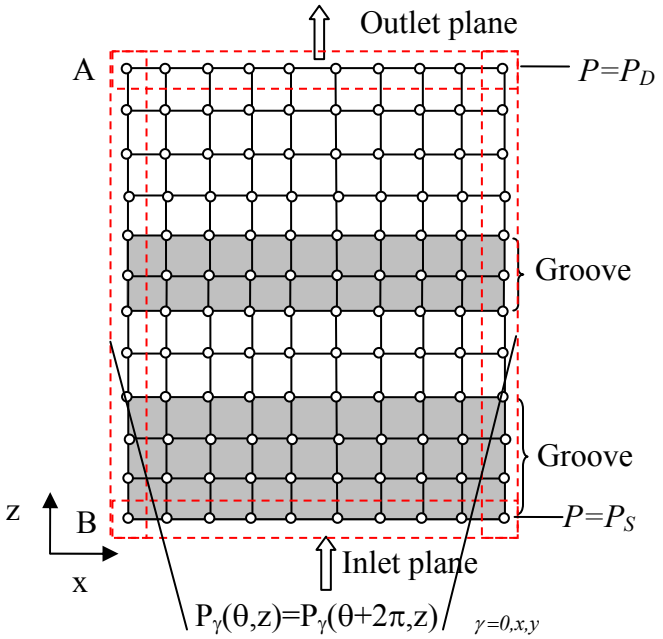

Figure 13 FEM mesh depicting nodes of interest for implementation of boundary conditions.

5.2.1.2 First Order Pressure Field

A) Null dynamic pressure at exit plane ($z= L$). While the static pressure is constant, it is assumed that there is not generation of dynamic pressure at the exit (discharge) plane. This condition is set to the upper nodes of an element along the exit plane.

$$\bar{P}_{\gamma}^{e}\Big|_{z=L} = 0 \tag{5.23}$$

B) At the inlet plane (inlet to feed plenum) the axial flow induced by the dynamic (fluid squeezing) motions is set to zero due to geometrical symmetry.

$$q_{z}\Big|_{z=0} = 0 \tag{5.24}$$

This boundary condition implies that the "perturbed" axial flow does not cross the middle plane and that there is a non-zero dynamic pressure field at this plane. This is a Neumann type B.C. implemented by treating the nodes at inlet plane as internal nodes.

6. PREDICTIONS OF DYNAMIC PRESSURE AND FORCE COEFFICIENTS FOR A GROOVED SFD AND A GROOVED OIL SEAL AND COMPARISONS TO EXPERIMENTAL DATA

This section presents predictions of dynamic pressure fields and dynamic force coefficients in a grooved SFD and a grooved oil seal, both operating with small amplitude journal motion. The geometry of both devices replicates the configurations tested in Refs. [27, 29]. Predictions of the pressure distribution in the damper and the seal stand to qualitatively describe the relative contribution of fluid inertia and viscous forces to the overall force response in each test device. In addition, the pressure profiles also help illustrating the influence of the grooves in the pressure distribution and overall force response of each test configuration.

Predictions of force coefficients are presented and compared to experimental results. In the case of the SFD, only test data for centered journal operation is available although with large orbit radii. On the other hand, the grooved oil-seal test data includes centered and off-centered journal operation for small amplitude motion. The predicted force coefficients for journal centered operation are presented as a function of the effective groove clearance values (c_η) and compared to experimental data. The analysis of the results indicates that there is a narrow range of effective groove depths (c_n) that yield excellent correlation to the experimental force coefficients, including added mass coefficients. The description of the SFD tested in Ref. [27] follows.

6.1 Squeeze Film Damper

The test SFD included in this study has been operated extensively, consistently evidencing large added mass coefficients (~ 10 kg, i.e. as large as the mass of the system), while predictions based on the classical theory [4] are ~5 times smaller that the experimental results. Figure 14 shows a cut view of the test SFD. The damper incorporates a mechanical seal at the discharge end that effectively prevents oil leakage. The lubricant is fed from the top and fills the inlet groove, film land, and end discharge

groove before exiting the damper radially through four outlet ports. Measurements of the dynamic pressure are available at the discharge groove.

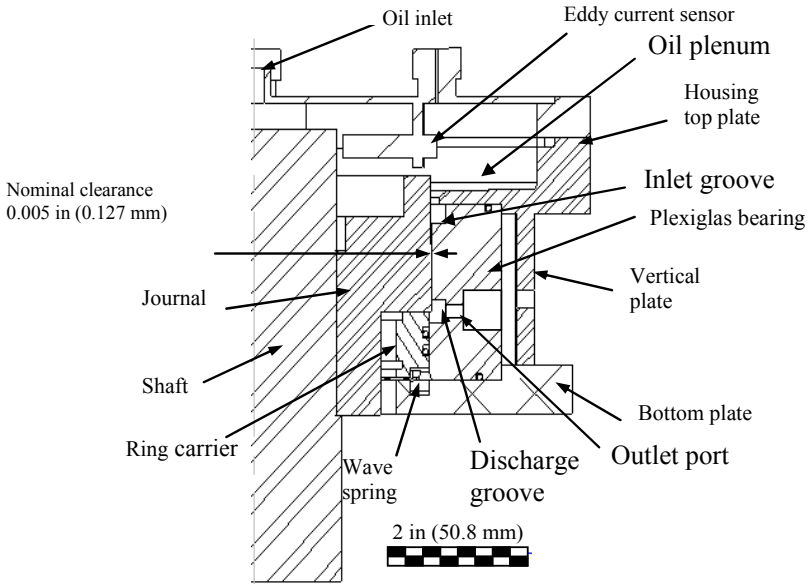

Figure 14 Sealed-end SFD assembly cut view [27].

6.1.1 Geometry and Model Descriptions

Table 1 shows the SFD dimensions and test conditions. Figure 15 depicts a schematic view of the SFD detailing the groove and land dimensions, and the flow region subdivisions.

The flow domain for the analysis encompasses the inlet groove, fluid film land and discharge groove. The boundary conditions for predicting the fluid film pressure and reaction forces are:

- Null axial flow at the feeding groove inlet, Eq. 4.20. This condition implies that the dynamic pressure in the plenum does not allow for backflow at the damper inlet.
- Continuity of pressure and flow rates at the groove-land interfaces.
- Amplitude of dynamic pressure amplitude set at discharge groove from measurements reported in Ref. [61].

Table 1 Test conditions for dynamic load tests (CCO). Lubricated SFD.

Dimensions	
Diameter (D)	127 mm
Clearance (c)	125-127 μm (4.9-5 mils)
Land length (L)	25.4 mm
Inlet groove clearance (c_{g_I})	78c
Inlet groove length	6.36 mm
Discharge groove clearance ($c_{g_{III}}$)	31c
Discharge groove length	4.1 mm
Parameters	
Discharge groove pressure (P_D)*	8.6 kPa-15.5 kPa
Inlet pressure (P_S)*	31 kPa
Frequency range	20-70 Hz
Lubricant temperature (T)	23-25 ^{0}C (73-77 ^{0}F)
Viscosity (η) (ISO VG-2 oil)	3.1 cP- 2.8 cP
Density (ρ)	800 kg/m^3
Orbit amplitude (e)	12-50 μm (0.5-2 mils)
Flow restrictors (hole diameter)	2.8 mm

*: Gauge pressure.

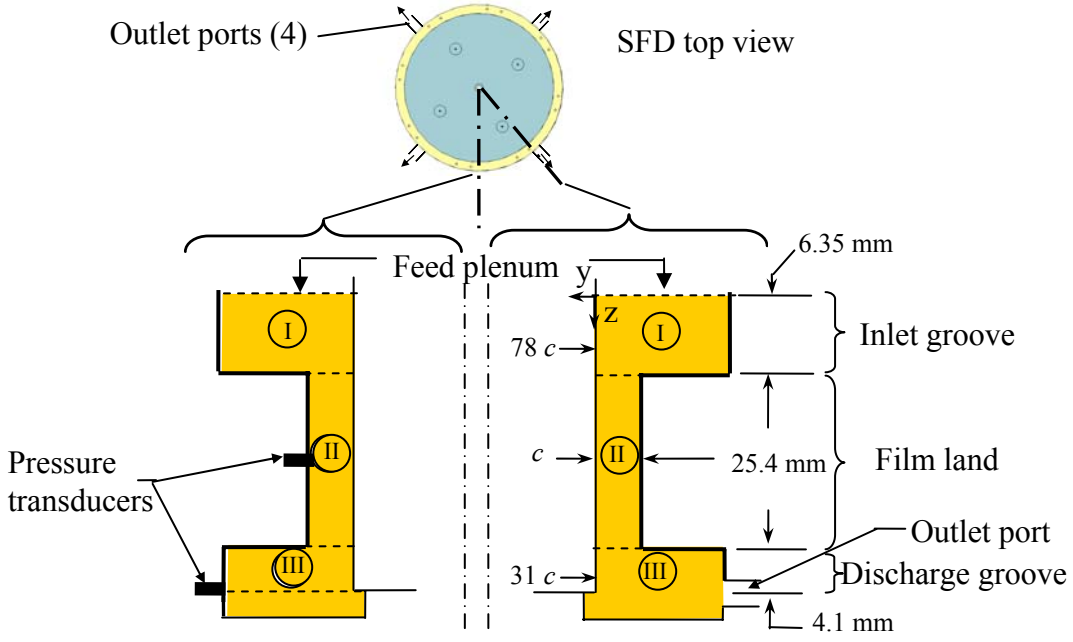

Figure 15 Test squeeze film damper geometry and flow regions [27].

6.1.2 Results from Analytical Solution

6.1.2.1 Dynamic Pressure

This section presents the predicted dynamic pressure field generated within the SFD due to small amplitude journal motion about a centered position. The dynamic pressure field in the damper adds pressures generated due to viscous and inertia fluid effects. The pressure field due to viscous effects generates a tangential force that is proportional and opposes the journal velocity vector (i.e. damping force). On the other hand, the pressure field due to fluid inertia generates a radial force that is proportional and opposes the journal acceleration vector. Thus, the pressure field solely due to inertia effects are 180^0 out of phase respect to the acceleration of the film gap (d^2h/dt^2), i.e. the maximum peak occurs at the instantaneous maximum film thickness (i.e. $\theta = 0$). Similarly, the pressure field due to viscous effects are 180^0 out of phase respect to the motion (velocity) of the film thickness (dh/dt), i.e. as the local film thickness decreases the pressure in the squeeze-film land increases, and vice versa. Thus, the maximum peak is $\pi/2$ radians away from the minimum film thickness (i.e. $\theta = \pi$). In the pressure plots presented in this and the next section the minimum film thickness takes place at $\theta=\pi$ and the maximum film gap is at $\theta=0$.

Figure 16 shows the dynamic pressure field due to circular centered motions of 12 μm in amplitude (i.e. 0.1c) at 50 Hz. The figure also depicts the film thickness and its time derivatives (velocity and acceleration). Note that the pressure field is a function of the time and the angular coordinate; though for circular centered orbits, the pressure is stationary in a coordinate system rotating with the journal center precessional speed [12]. Figure 16 shows the pressure field assuming no pressure generation at the inlet and outlet grooves. This pressure field corresponds closely with the classical finite-length solution for a single SFD land [4] as derived in Section 4. Note that the magnitude of the pressure induced by fluid inertia effects is much smaller that the peak of the pressure field due to viscous effects. Indeed, the Reynolds number (Re^*) at the SFD land is 0.2 (i.e. very low).

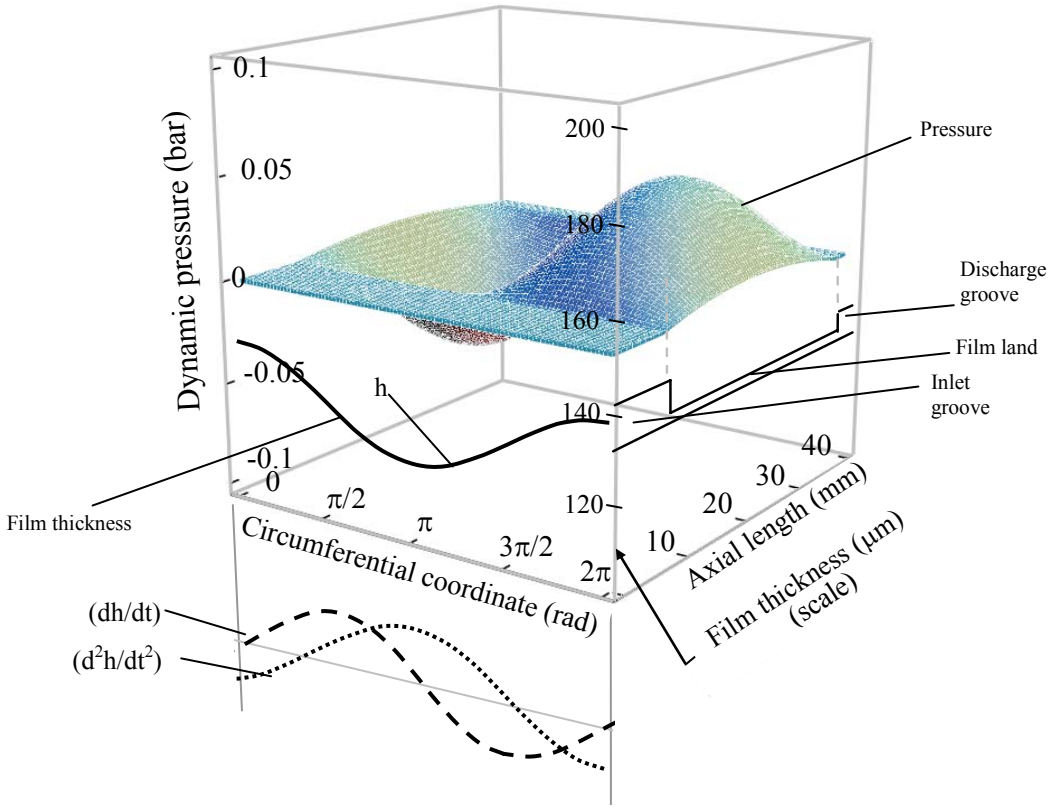

Figure 16 Predicted dynamic pressure field across SFD due to journal circular centered orbit (12 μm, 50 Hz). Classical theory [4] (Finite length model, null dynamic pressure at inlet and discharge grooves).

Figure 17 depicts predicted and measured dynamic pressures at the film land and discharge groove versus dimensionless time ($t\omega$) for forced excitation at 50 Hz resulting in circular orbits of ~12 μm in amplitude. The graph displays full-scale and zoomed views of two full periods of circular whirl motion and includes a depiction of the film thickness recorded at the location of pressure measurements. The measured dynamic pressure at the discharge grove is used as boundary conditions; thus the predictions obviously match the measurements at this location. The magnitude and phase of the pressure wave respect to the film thickness provides the necessary information to define the inertial and viscous components of the pressure field. In this case, the pressure is 180^0 out of phase with respect to the film gap acceleration (d^2h/dt^2), which indicates that the pressure field is mainly inertial. Indeed the ratio of the inertial forces to viscous

forces associated to this test conditions is ~10:1. The dynamic pressure in the mid-span of the film land is obtained from predictions using the given measurements at the discharge groove and considering an effective inlet groove clearance (c_{η_I} = 14c). As detailed next, in Section 6.1.2.2, this effective clearance yields the best correlation between the predicted and experimental force coefficients. Predictions of the film pressure profile mach the experimental results well considering the magnified scale. A more detailed discussion of this pressure field is included in the next graph.

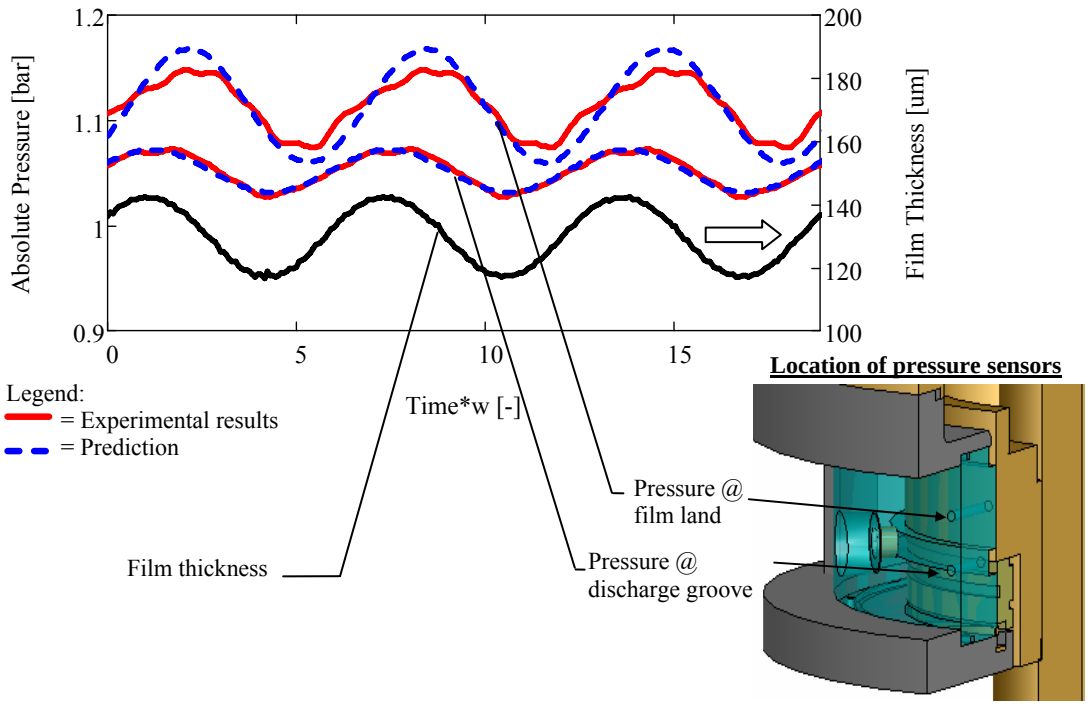

Figure 17 Dynamic pressure measurements and predictions at SFD land and discharge groove and film thickness. Frequency 50 Hz, 12 μm orbit amplitude, supply pressure= 1.31 bar. Dynamic pressure measurements at discharge groove used (matched) as boundary values. Dynamic pressure at the land predicted using an effective inlet groove clearance (c_{η_I} = 14).

Figure 18 depicts the pressure field from the improved model considering the generation of dynamic pressure at the inlet groove and using an effective discharge groove clearance (c_η) of 14. As previously mentioned, it can be seen that the pressure at

the groove is mainly due to fluid inertia effects as it is 180^0 out of phase with respect to the film thickness acceleration (d^2h/dt^2). These results are similar to the test data presented by Arauz and San Andrés [19], who reached the same conclusion about the inertial nature of the pressure field at the grooves. Note that squeeze film Reynolds number (Re*-based on the effective groove clearance - c_η) at the inlet and discharge grooves is 28 and 40, respectively. Thus as indicated by Tichy [8] and San Andrés [12], for $Re^* > 12$ the fluid inertia forces are indeed dominant at the grooves. Furthermore, although the peak dynamic pressure at the SFD land (due to viscous effects) is similar to that shown in Fig. 16, the contribution of the inertial pressure field is more noticeable than in Fig. 16. Thus, the influence of the inertial pressure field generated at the groove extends to the film land and enhances the fluid inertia effects (radial force) over the entire axial length of the damper land. Of course, these observations apply to the chosen effective groove depth since the relative contribution of the groove to the damping and inertia forces is a strong function of this parameter. A detailed description of the correlation between the damping and inertia force coefficients respect to the groove clearance follows.

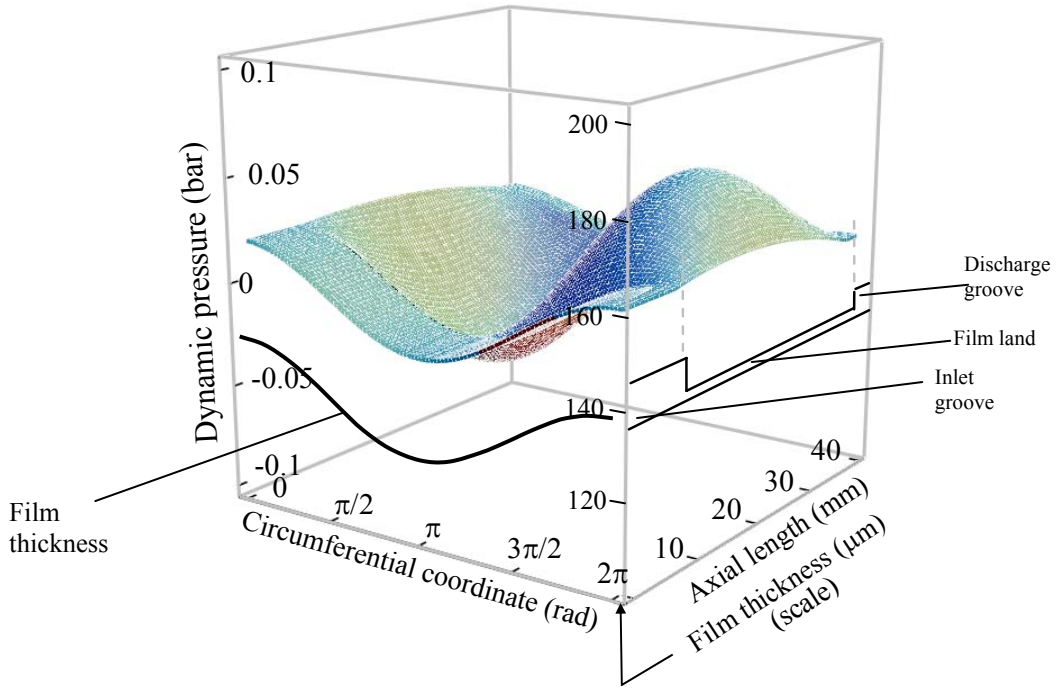

Figure 18 Predicted dynamic pressure distribution across end seal SFD due to journal excitations (12 μm, 50 Hz). Improved model incorporating contribution of grooves to dynamic pressure field using an effective inlet groove clearance (c_{η_I} = 14 c).

6.1.2.2 SFD Force Coefficients

This section includes comparisons of experimental and predicted force coefficients for the test SFD in Ref. [27]. The predicted force coefficients are presented in terms of the inlet effective groove clearance ($c_\eta = d_\eta + c$) to illustrate the effect of this parameter (c_η) on the force coefficients and to validate of the assumptions made in the current analysis. In the case of the discharge groove there is no need to evaluate the effective groove clearance since the pressure profile is based on actual measurements. However, a groove clearance could be obtained from the Re^* value based on the particular magnitude of the pressure and phase of the pressure field (i.e. relative contribution of viscous and inertial forces). For the given pressure measurements at 50 Hz with Re^*=40, the corresponding effective groove clearance ($c_{\eta_{III}}$) is ~18.

Figure 19 depicts the damping and added mass coefficients versus effective inlet groove-to-film clearance ratios. The predictions show that the damping coefficient rapidly converges to a constant value (C_{XX}=5 kNs/m) for $c_{\eta_I} \geq 10c$. Hence, as illustrated with the pressure profiles, a deep groove contributes little to the test seal tangential (damping) force. On the other hand, the direct added mass coefficient *(M_{XX})* converges more slowly towards an asymptotic value. However, note the predicted added mass coefficient is in good correlation with the experimental results for effective depths (d_η) where the damping coefficient is already insensitive. Thus, the best estimates of mass coefficients correspond to the smallest effective groove clearances (i.e. $c_{\eta_I} \sim 14c$) that do not have a significant impact (>10%) on the SFD tangential (damping) forces. Furthermore, comparisons of the damping values for decreasing d_η with that for a deep groove may be used to obtain an effective groove clearance c_η that accurately predicts the mass coefficients. Importantly enough, note that added mass coefficients reaches a peak value for a specific clearance. In particular, for the current case, inlet groove clearances (c_I) of 2 to 3 times the damper clearance would yield added mass coefficients above 20 kg (i.e. twice the mass of the test SFD).

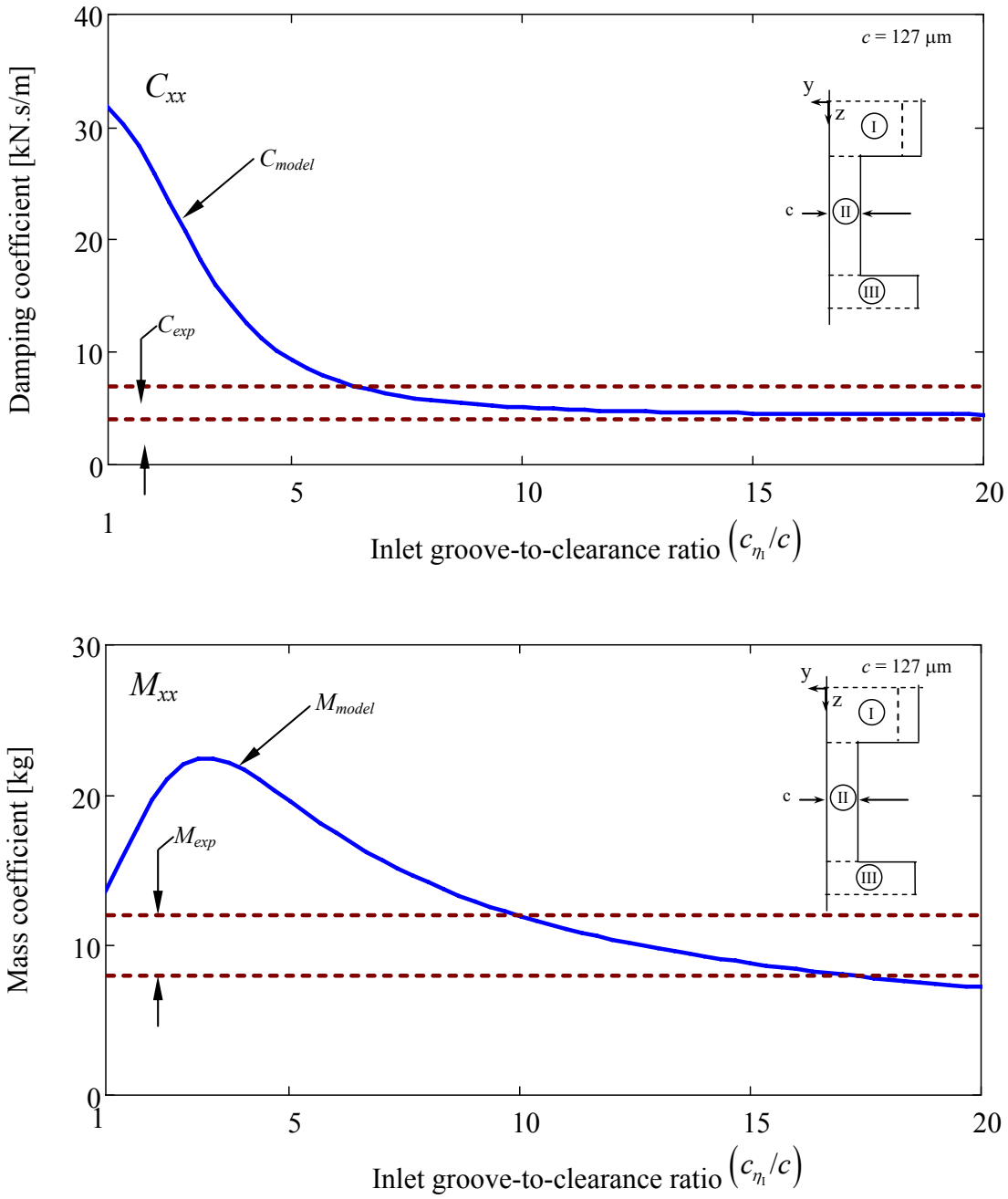

Figure 19 Predicted SFD added mass coefficient versus effective inlet groove clearance. Solid lines represent predictions($c_{\eta_{III}} \sim 18c$). Dotted lines represent range of experimental values from [27].

6.2 Grooved Oil Seal

Graviss [29] reports experimental data for a multiple groove oil seal. Figure 20 depicts the actual configuration of the grooved oil seal. The test configuration is an axially symmetric arrangement, and includes two oil seals separated by a central feed plenum. This configuration allows balancing the thrust force due to the pressure drop across the seals. The added mass coefficients reported for this configurations range from ~15 to ~30 kg, while the classical predictions [4] yield around ~3 kg (i.e. 5 times smaller). In addition, for the groove seal, the force coefficients (stiffness and damping) are underpredicted (~2 times) by Semanate and San Andrés [28].

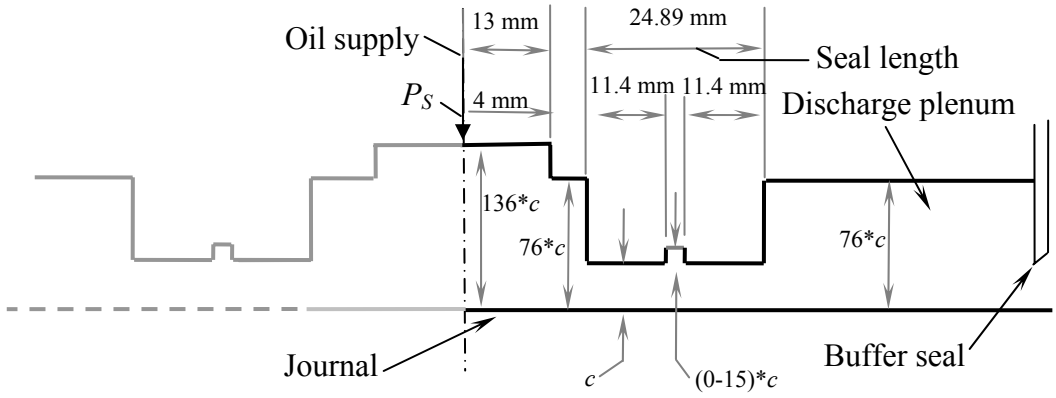

Figure 20 Configuration of parallel oil seals tested in [29].

6.2.1 Geometry and Model Description

Figure 21 depicts the modeled portion of the oil seal and the partition into flow regions. Table 2 lists the physical dimensions, fluid properties and operating conditions of the test seal. The seal is divided into 4 flow regions with the following boundary conditions:

- Dynamic pressure set to zero at exit plane.
- Continuity of pressure and flow rates at the groove-land interfaces.
- First order (perturbed) axial flow rate at inlet plenum (symmetry plane) is set to zero (no back flow).

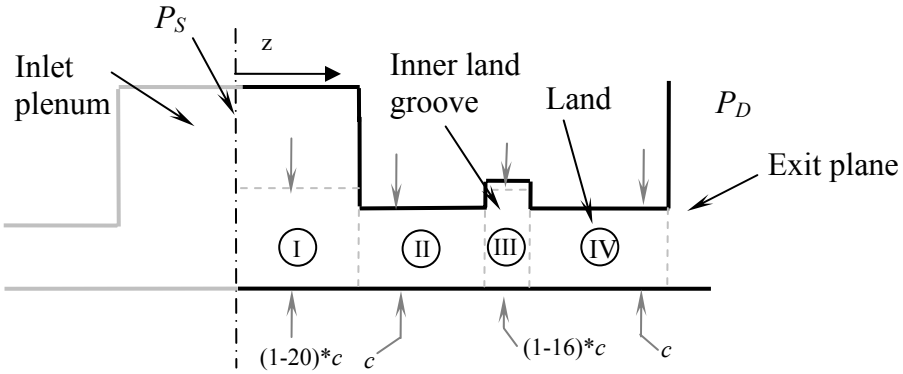

Figure 21 Partial view of test grooved oil seal geometry [29] and flow regions for predictions.

Table 2 Oil seal configuration, operating conditions and fluid properties.

Dimensions	
Journal Diameter	117 mm
Seal land length	24.89 mm
Land clearance (nominal @ 25 ^{o}C)	85.9 μm
½ central plenum length	17 mm
½ central plenum clearance (c_{g_I})	136c
Inner land groove length	2 mm
Inner land groove clearance ($c_{g_{III}}$)	(c, 6c, 11c, 16c) (tests)
Parameters	
Shaft speed	4000 rpm -10000 rpm
Whirl frequency, ω	0-200 Hz
Supply Pressure (P_s)	24-70 bar
Oil density (ISO VG32)	850 kg/m^3
Oil viscosity	0.02 Pa.s

6.2.2 Results from Analytical Solution

6.2.2.1 Dynamic Pressure

Figures 22 and 23 show the predicted dynamic pressure field for the smooth seal due to small amplitude journal motions about a centered position (5 μm, 200 Hz) while rotating at 10,000 RPM. Both figures show results corresponding to a seal supply pressure of 70 bar. Figure 22 depicts the dynamic pressure field assuming a null dynamic

pressure at the central plenum. Figure 23 shows the pressure field from the improved predictive model using an effective central plenum clearance (c_{η_l} = 12c). The results are similar to those observed for the SFD case, although the pressure field due to fluid inertia effects is not as large compared to the pressure field due to fluid viscous effects. Similarly to the SFD case study, the pressure field in Fig. 21 yields added mass coefficients (~3 kg) that are nearly five times smaller than those identified from experiments (~15 kg).

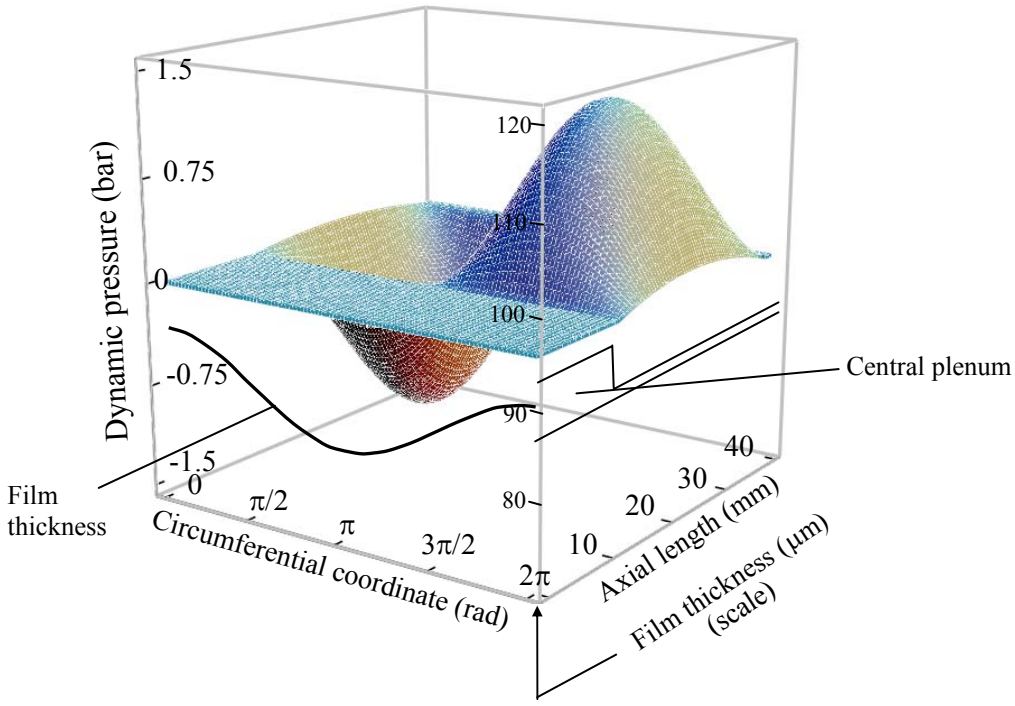

Figure 22 Predicted dynamic pressure distribution across smooth seal due to journal excitations (5 μm, 200 Hz). Classical theory [4] (Finite length model, null dynamic pressure at plenum).

The pressure fields show dimensional units to illustrate an important fact related to the amplitude of the pressure fluctuations at the central plenum section. Note that the amplitude of the pressure field is a function of the excitation amplitude, but more importantly it also varies with the excitation frequency, which depends on the nature of the pressure field (i.e. viscous or inertial). While the forces due to viscous effects are

directly proportional to the excitation frequency (ω), the inertia forces are proportional to ω^2. Thus, as Fig. 23 illustrates, the pressure fluctuations at the plenum associated to the 10 μm journal perturbation at 200 Hz are relatively small (~ 0.35 bar), though this entire pressure field corresponds to a relatively large added mass coefficient (~18 kg). Now, considering that the inlet pressure for the test seal ranges from 24-70 bar, the dynamic pressure field at the groove is almost imperceptible for the given test frequency range (0-200 Hz). This may explain the seemingly insignificant dynamic pressure at the central plenum mentioned in Refs. [29, 34].

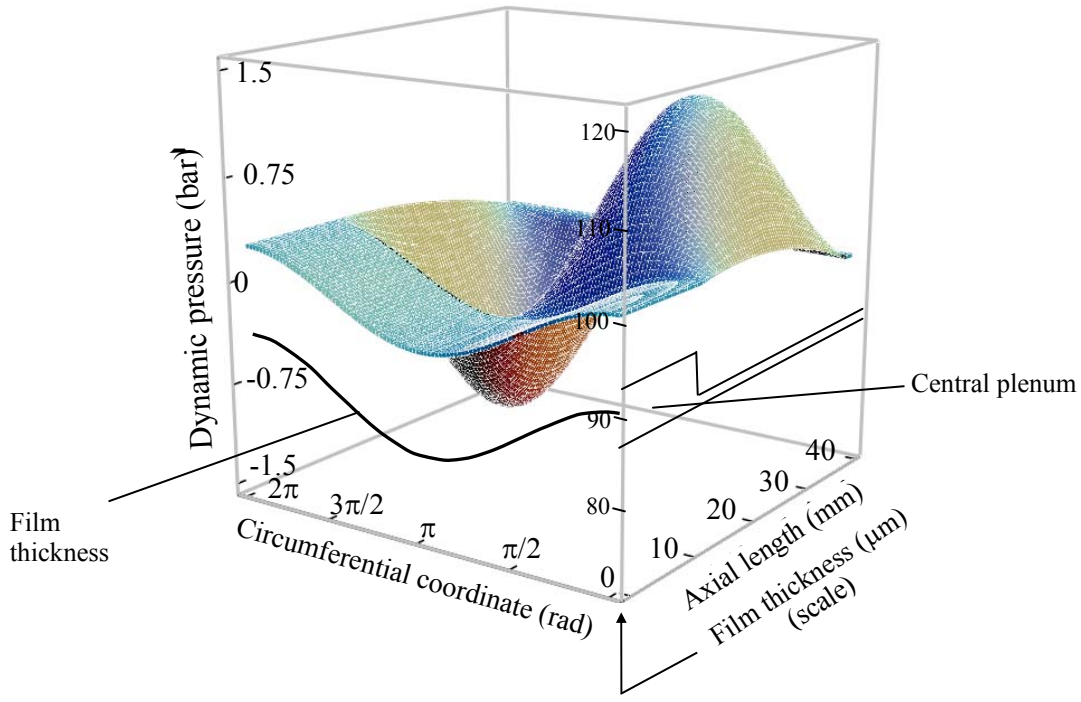

Figure 23 Predicted dynamic pressure distribution across smooth seal due to journal excitations (5 μm, 200 Hz). Improved model incorporating contribution of grooves to dynamic pressure field using an effective inlet groove clearance (c_{η_I} = 12*c*). Film thickness noted.

Figures 24 and 25 show predicted dynamic pressure fields for the seal with the deepest inner land groove (c_{III} =15 *c*). The pressure field corresponds to small journal motions about a centered position (10 μm, 200 Hz). Figure 24 depicts the pressure field

assuming a null dynamic pressure at the central plenum and the inner land groove. Note that the peak pressure in the land is much smaller (around 1/4) than that of the smooth seal. This pressure profile will determine direct damping and added mass coefficients smaller by a factor 2 and 5 with respect to test data, respectively. Figure 25 shows the pressure field using an effective plenum (c_{η_I}) and inner land ($c_{\eta_{III}}$) groove clearance of 12*c* and 7c, respectively. In this case both the plenum and inner-land groove enhance the fluid inertia effects across the seal lands. In fact, as the experimental results show, the added mass coefficients identified from the grooved seal (~30 kg) are larger than those associated to the smooth land seal (~20 kg).

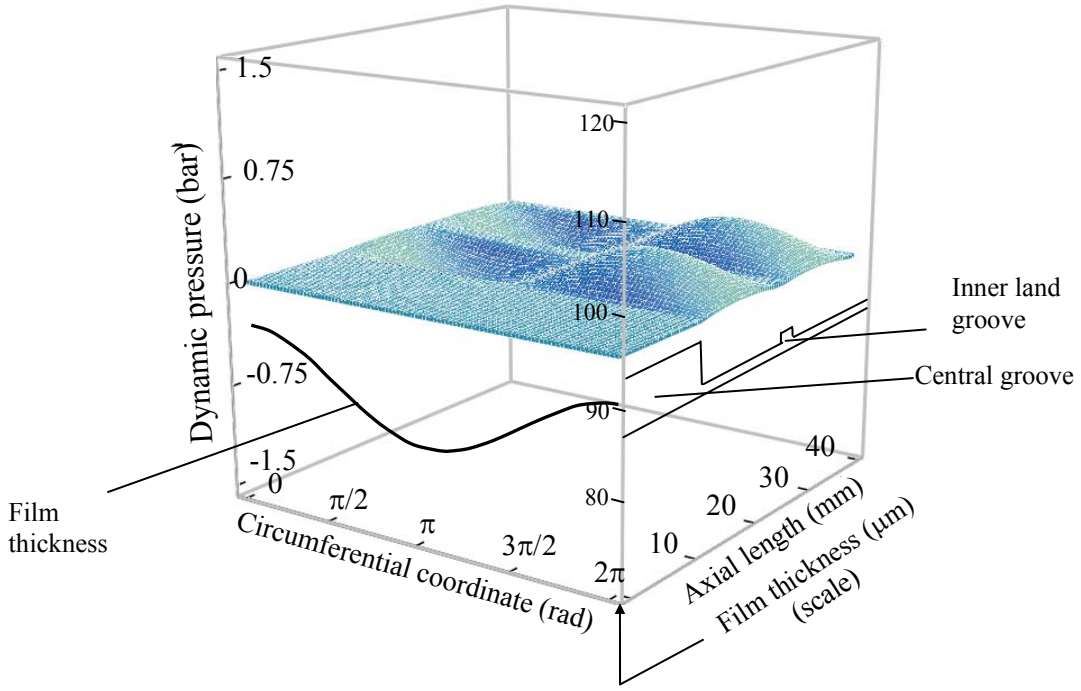

Figure 24 Predicted dynamic pressure distribution across seal with inner land groove due to journal excitations (5 μm, 200 Hz). Classical theory [4] (Finite length model, null dynamic pressure at plenum and groove).

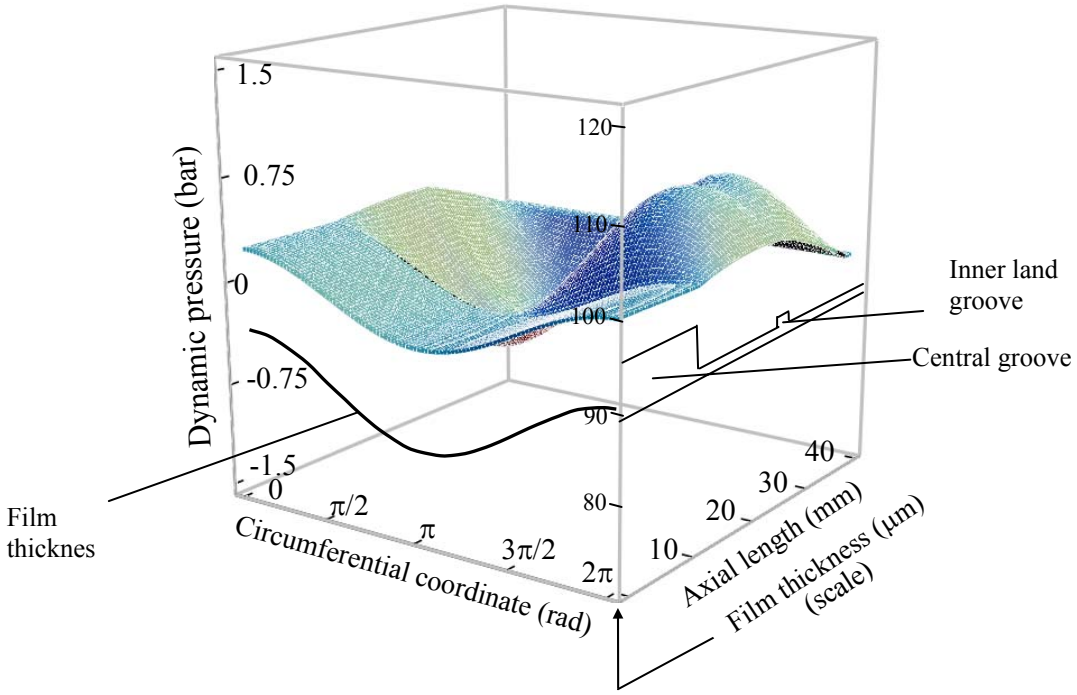

Figure 25 Predicted dynamic pressure distribution across seal with inner land groove due to journal excitations (5 μm, 200 Hz). Improved model incorporating contribution of grooves to dynamic pressure field using an effective plenum and inner land groove clearances (c_{η_I} = 12 c, $c_{\eta_{III}}$ =7 *c*).

6.2.2.2 Seal Force Coefficients

Figure 26 presents the predicted damping (C_{XX}) and added mass coefficients (M_{XX}) versus an effective central plenum-to-seal clearance ratios for the smooth seal configuration, i.e. without an inner land (internal) groove (i.e. $c_{III} = c$). The dotted lines enclose the range of experimental values reported in [29] for a three oil supply pressures (24-70 bar). Regarding the inlet groove, the results are similar to those found for the SFD. Again, the best estimates of mass coefficients are within the neighborhood of c_η magnitudes for which the overall damping becomes insensitive to the groove depth. From the results shown, one easily determines that the effective inlet or central plenum clearance that reproduces the experimental results is $10c < c_\eta < 15c$.

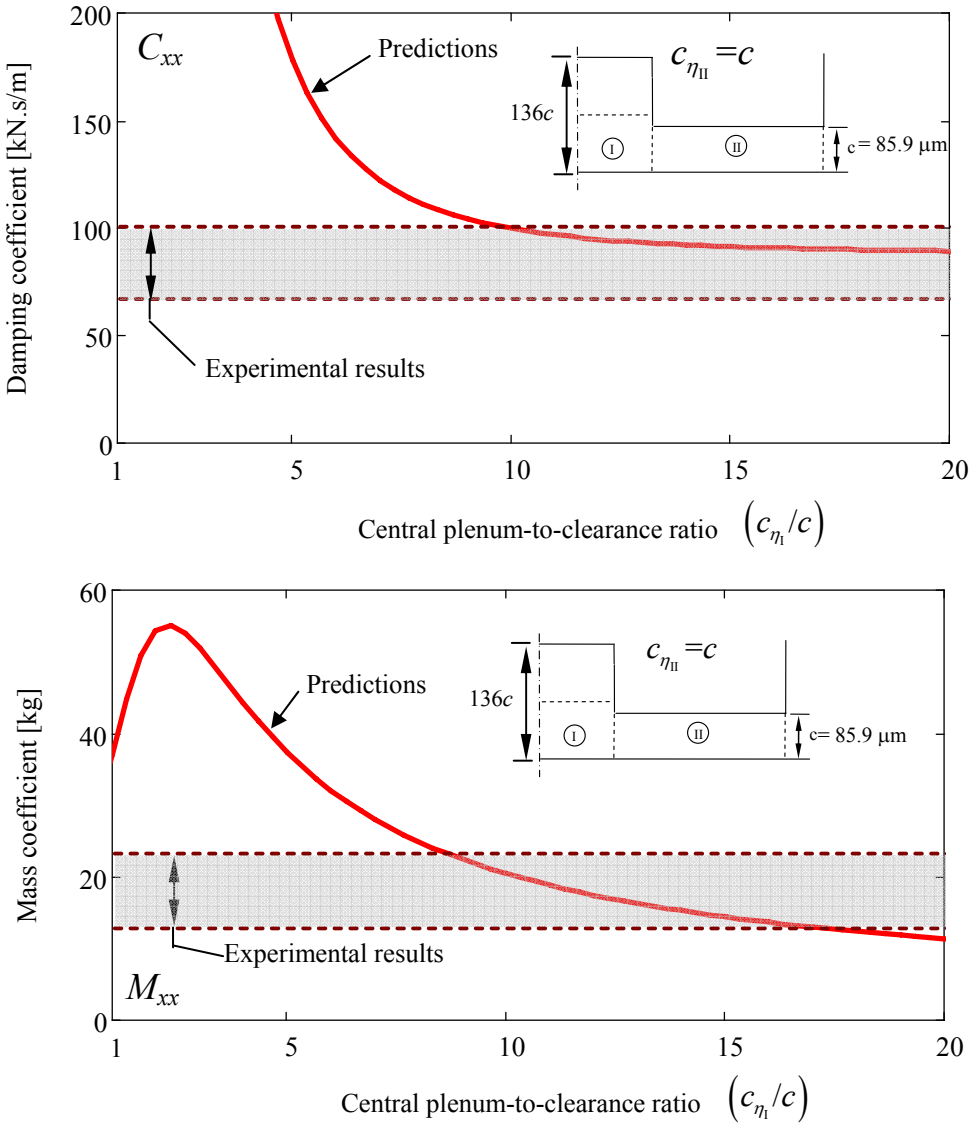

Figure 26 Predicted direct damping and added mass coefficients versus smooth seal effective central plenum-to-land clearance ratio. Solid lines represent predictions and dotted lines enclose the range of experimental values from [29] for a smooth seal (no inner land groove).

For the configuration with an internal groove dividing the original seal length, Fig. 27 presents the predicted damping and added mass coefficients versus effective inlet plenum-to-seal clearance ratios. The graph includes three increasing inner land grooves of effective groove clearances $(c_{\eta_{III}}=6c,\ 11c,\ 16c)$. The damping ($C_{XX}$) quickly decreases

for increasing inner-land groove clearances. On the other hand, the added mass (M_{XX}) increases as the effective inner-groove clearance increases to a peak value (i.e. $c_{\eta_{III}} = 6c$). As in the previous figure, the added mass coefficient correlates best with predictions for the smallest c_{η}, i.e. 6*c*. This clearance has a minimum impact on the damping force developed by the seal.

Figure 28 depicts the direct damping and added mass coefficients versus inner land groove-to-seal clearance ratios, including two effective clearances for the central groove. These values are within the range of best correlation with experimental data in Fig. 27. The damping steadily decreases as the inner land groove effective clearance ($c_{\eta_{III}}$) increases, whereas the mass presents a maximum value at $c_{\eta_{III}} \approx 5$. In this case, the inner-land groove is relatively shallow and short (2 mm) and its effective depth is ~ 1/3 of its physical depth to give good correlation with the experimental results.

Figure 29 displays the cross-coupled stiffness coefficient (K_{XY}) versus rotor speed. The results include experimental data for smooth (no inner-land groove) and with a inner land groove 15*c* deep (i.e. $c_{III} = 16c$). The predictions are based on an effective central groove clearance (c_{η_I}) of 12*c* and an inner-land effective groove clearance ($c_{\eta_{III}}$) of 7*c* (i.e. ~half of actual groove size). The predictions correlate best for the lowest rotor speeds. More importantly, the variation (reduction) of the cross-coupled stiffness is properly captured using effective groove clearances ($c_{\eta_{I,III}}$).

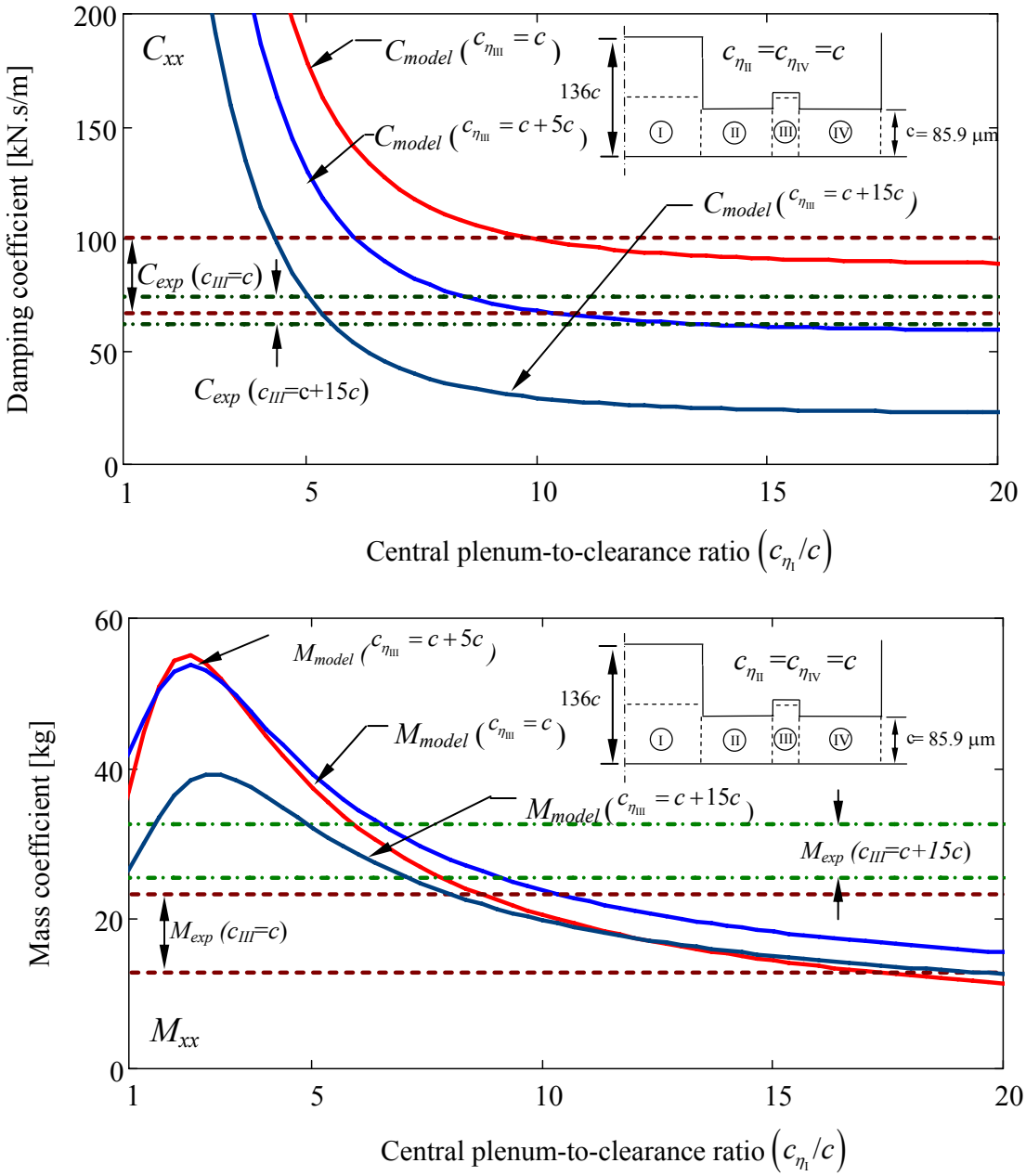

Figure 27 Predicted direct damping and added mass coefficients versus seal effective central groove-to-clearance ratio. Solid lines represent predictions for three effective inner land seal groove clearances $(c_{\eta_{III}}=6c,\ 11c,\ 16c)$. Dotted lines enclose the range of experimental values from [29] for two seal clearances $(c_{g\,III}=c,\ c+15c)$.

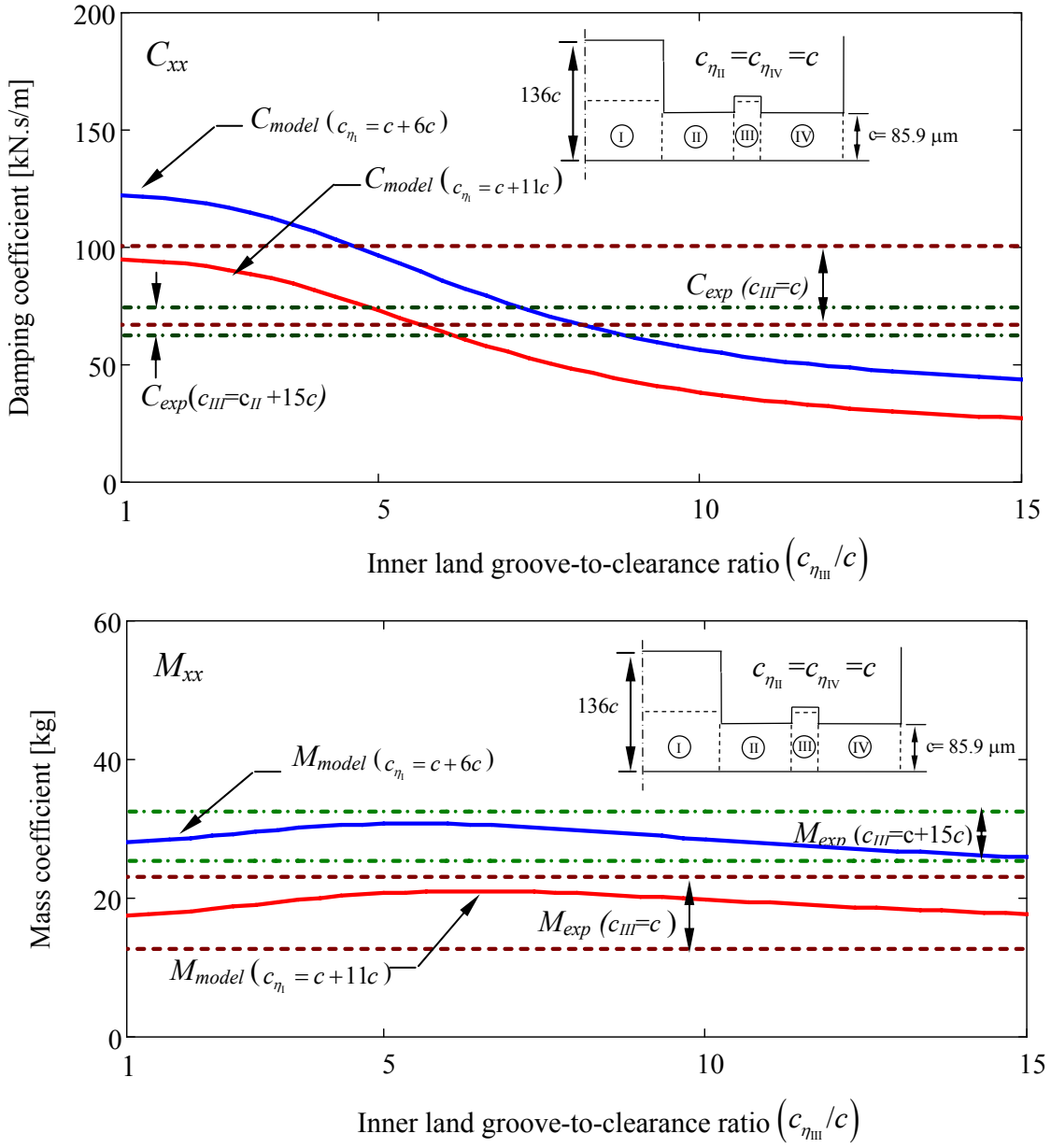

Figure 28 Direct damping and added mass coefficients versus effective inner land groove clearance. Solid lines represent predictions for two effective central plenum clearances $(c_{\eta_I}=7c,\ 12c)$.Dotted lines enclose the range of experimental values from [29] for two seal clearances $(c_{g\,III}=0,\ 16c)$.

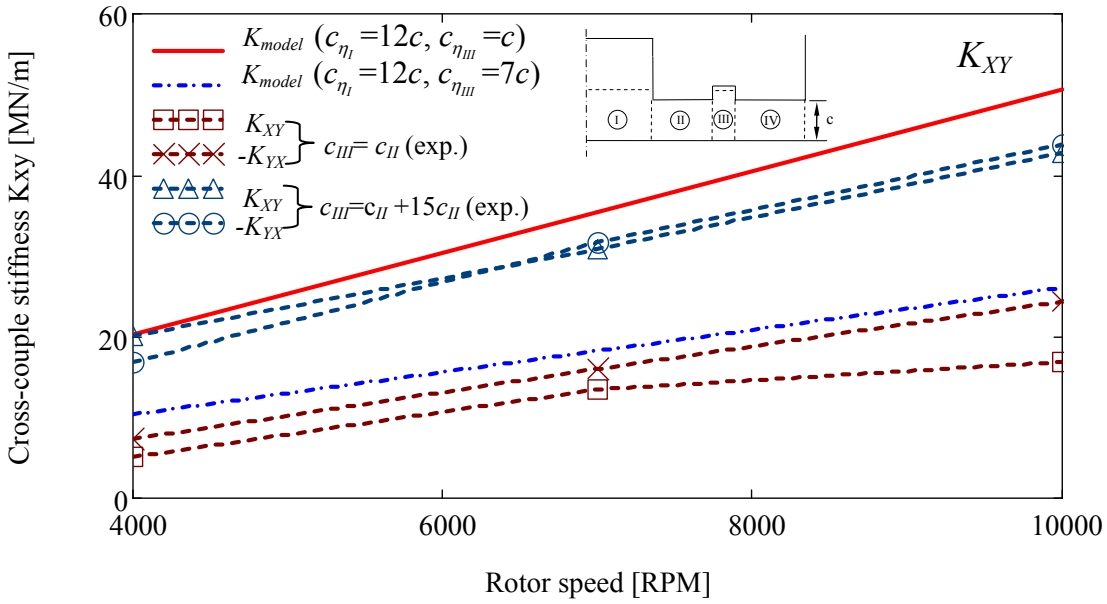

Figure 29 Cross-coupled stiffness coefficients versus rotor speed. Solid lines represent predictions for smooth seal and an effective inner land groove clearance with ($c_{\eta_{III}}$=c, 7c). Dotted lines represent experimental values from [29] for a smooth seal and an inner land grooved seal (with clearance =16*c*).

6.2.3 Results from Finite Element Model – Off-Centered Operation

This section presents comparisons of experimental and predicted damping, stiffness and mass coefficients for the oil ring seal for centered and off-centered journal operation tested by Graviss [29]. Table 3 lists the fluid properties, operating conditions, and number of elements of the FE mesh. Figure 30 shows the actual journal locus obtained from four journal eccentricities. Since the external load is along the *Y* direction, the proximity of journal center to the *Y* axis (i.e. small journal attitude angle) clearly indicates the presence of oil cavitation, in particular for the largest journal eccentricity ratios.

Table 3 Operating conditions fluid properties and number of elements for FE mesh .

Parameters	
Shaft speed	4000-10000 rpm
Oil density	850 kg/m^3
Static journal eccentricity ratios	0-0.7
Oil viscosity (smooth seal)	0.016 Pa.s (54 ^{0}C)
Oil viscosity (grooved seal)	0.019 Pa.s (49 ^{0}C)
Supply pressure	70 bar
FEM mesh (elements)	
Circumference	60
Seal land	12
Plenum	12
Inner land groove	6

Similar to the analytical development, the analysis reports results for half of the axially symmetric seal configuration. The comparisons include results for the oil seal without the inner groove (smooth land throughout) and with a machined (15c) depth groove at the inner land (i.e. c_{III} = c+15c). Following results from the parametric study, the effective clearance for the inlet oil supply (central) plenum (c_{η_I}) is set to 12c. This effective clearance presents the best correlation with all the force coefficients obtained for the smooth seal (i.e. no inner-land groove). For the oil seal with an inner-land groove, the inlet oil supply plenum effective clearance (c_{η_I}) remains constant and the inner-land groove effective clearance ($c_{\eta_{III}}$) is set to 7c.

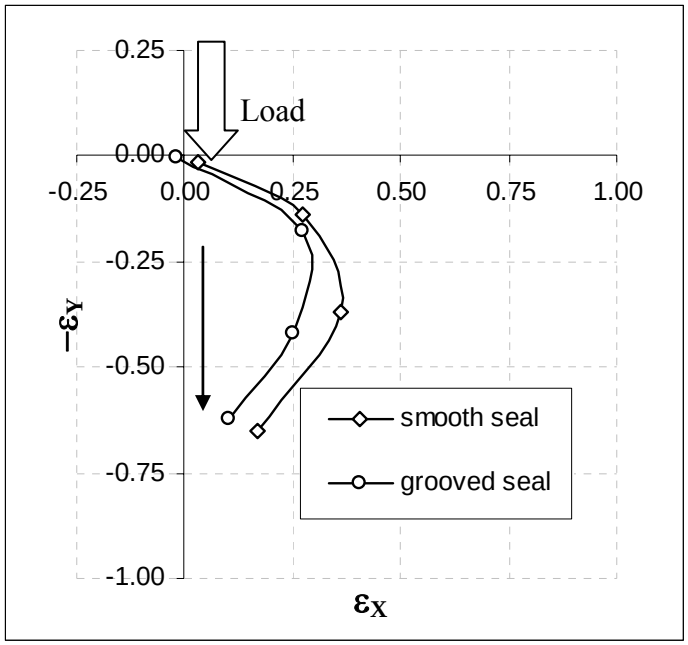

Figure 30 Measured journal centerline locus for smooth and grooved seal (c_{III}=16c). (70 bar, 10000 rpm) [29].

Figure 31 shows the seal reaction forces versus the static journal eccentricity. Predictions and experimental results present good correlation for journal eccentricities up to e/c = 0.5 for both the grooved and smooth seals. For the largest journal eccentricity (e/c=0.7), predictions are within 20 % of the experimental results for the smooth seal. On the other hand, the reaction force of the grooved seal is underpredicted by a factor of 2 for the largest journal eccentricity. For the largest journal eccentricities the oil temperature is significantly increases due to the small film thickness (i.e. large shear forces and power loss). Thus, the seal clearance and oil properties for the largest journal eccentricity ratio may differ significantly from the nominal values and have a large uncertainty. Ref. [29], however, does not include detailed information on the probable variation of the nominal values at such large journal eccentricity. Therefore, the predictions are compared with experimental results only for the low to mid-range eccentricities (i.e. ε= 0, 0.3, 0.5).

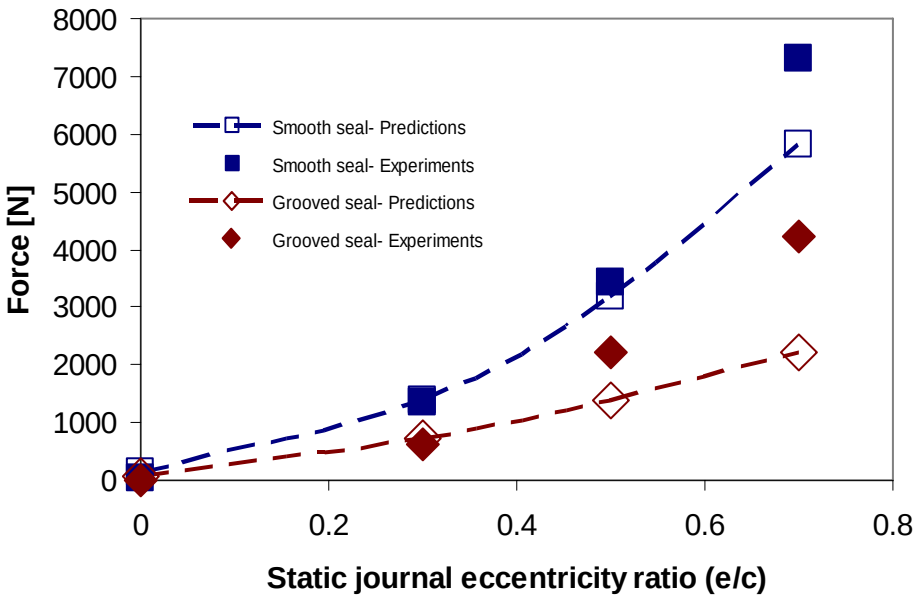

Figure 31 Oil seal reaction force versus journal eccentricity. Measurements in a smooth seal and a seal with inner land groove (c_{III} = 16*c*), 10000 rpm, 70 bar [29]. Predictions for smooth seal and seal with inner land groove ($c_{\eta_{III}}$ = 7*c*).

Figures 32 and 33 depict the direct (K_{XX}, K_{XY}) and crossed-coupled (K_{XY}, K_{YX}) stiffness coefficients versus the operating journal eccentricity, respectively. The predictions correlate well with the test data for the lower journal eccentricity ratios ($\varepsilon < 0.3$). For the 50 % eccentricity ratio there are discrepancies for both the direct and cross-coupled stiffness coefficients. The differences can be attributed in part to the lack of knowledge of the actual seal clearance variation due to thermal effects.

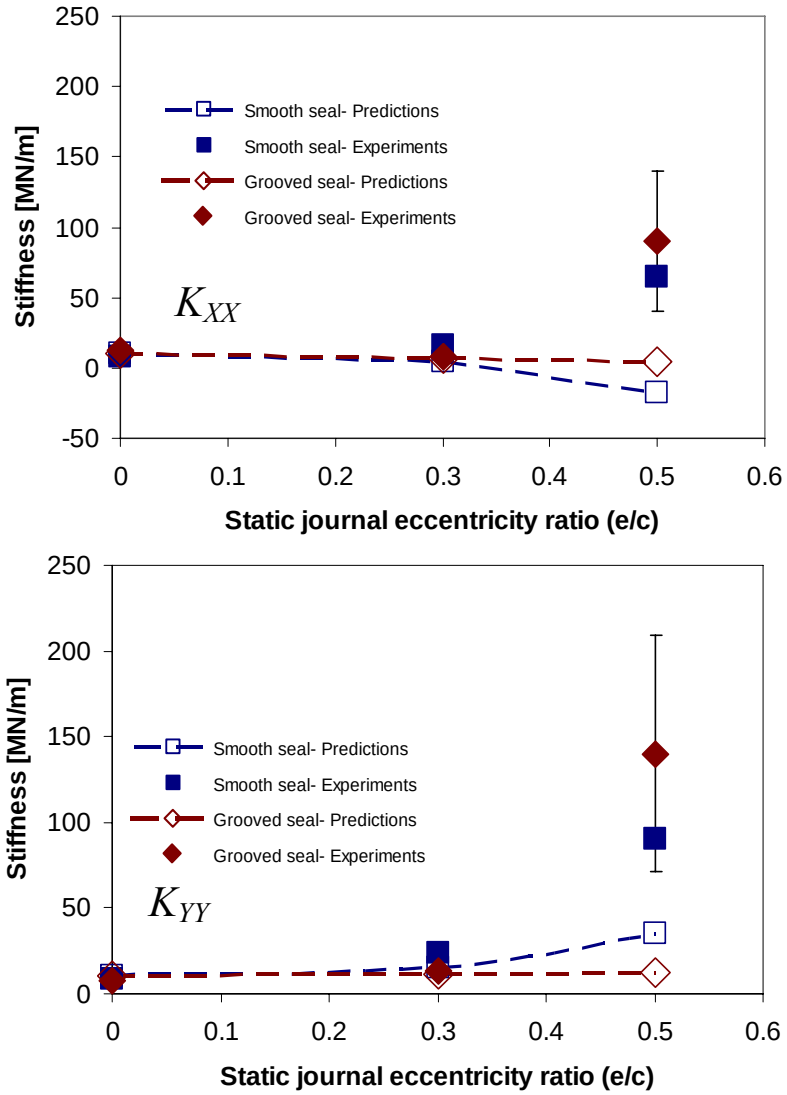

Figure 32 Direct stiffness coefficient (K_{ii}) versus journal eccentricity. Measurements in a smooth seal and a seal with inner land groove (c_{III} = 16c), 10000 rpm, 70 bar [29]. Predictions for smooth seal and seal with inner land groove ($c_{\eta_{III}}$ = 7c).

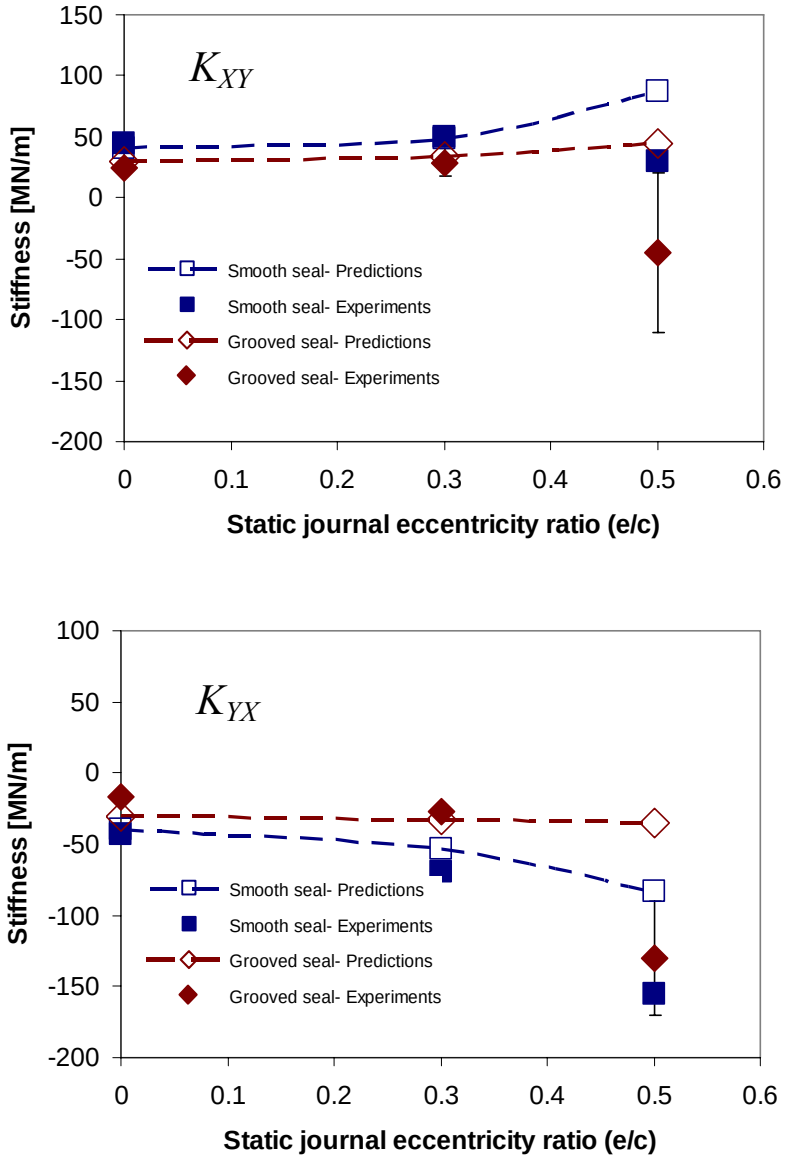

Figure 33 Cross-coupled stiffness coefficients (K_{ij}) versus journal eccentricity. Measurements in a smooth seal and a seal with inner land groove (c_{III} = 16c), 10000 rpm, 70 bar [29]. Predictions for smooth seal and seal with inner land groove ($c_{\eta_{III}}$ = 7c).

Figure 34 shows the cross coupled stiffness coefficients (K_{XY}, K_{YX}) versus rotor speed for two journal eccentricities (e/c=0, 0.3). The predictions show good correlation with the experimental results. In particular, the model adequately predicts the reduction of the cross-coupled coefficients after adding a groove in the middle of the smooth land seal.

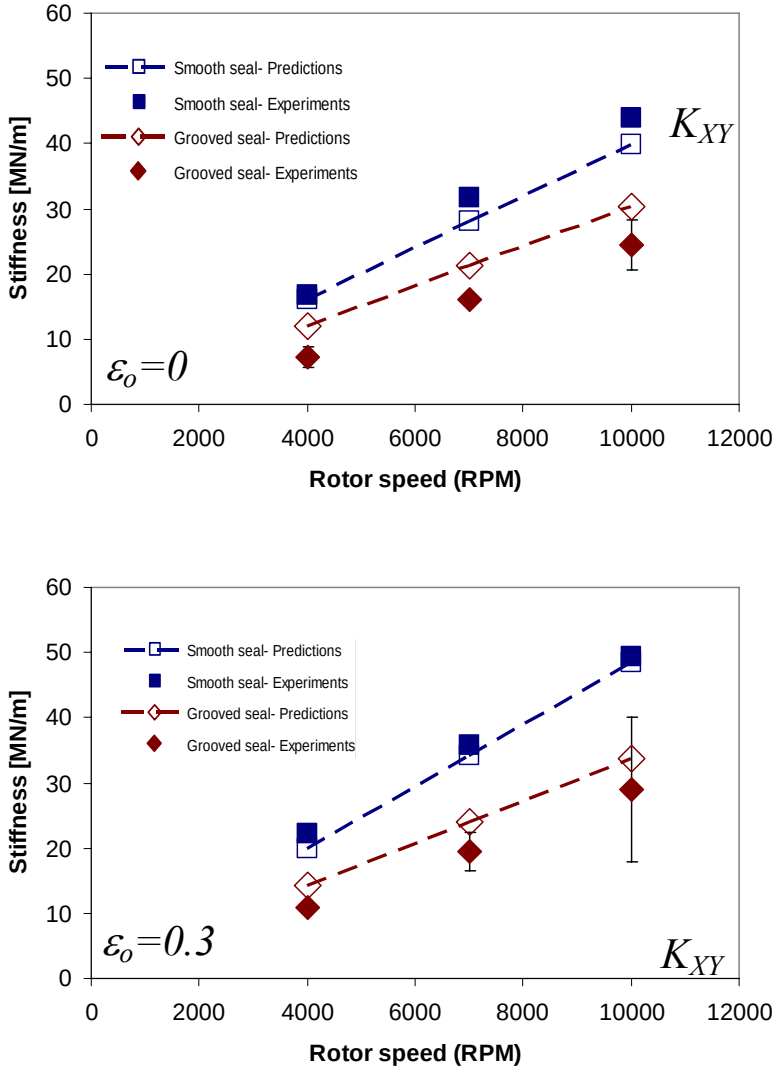

Figure 34 Cross-coupled stiffness coefficients (K_{xy}) versus shaft speed at two journal eccentricities (0, 0.3). Measurements in a smooth seal and a seal with inner land groove (c_{III} = 16c), 10000 rpm, 70 bar [29]. Predictions for smooth seal and seal with inner land groove ($c_{\eta_{III}}$ = 7c).

Figures 35 and 36 present the direct (C_{XX}, C_{YY}) and cross-coupled (C_{XY}, C_{YX}) damping coefficients versus static journal eccentricity ratio, respectively. The direct damping coefficients (C_{XX}, C_{YY}) show excellent correlation for the all the eccentricity ratios, except for the C_{XX} coefficient of the smooth seal that is 20% underpredicted for e/c=0.5.

The cross-coupled coefficients are much smaller than the direct damping coefficients and present moderate to good correlation for the different test journal eccentricities.

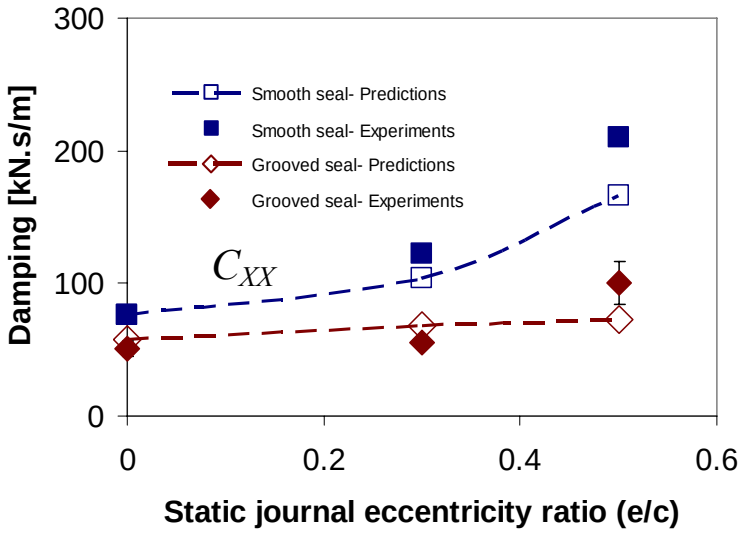

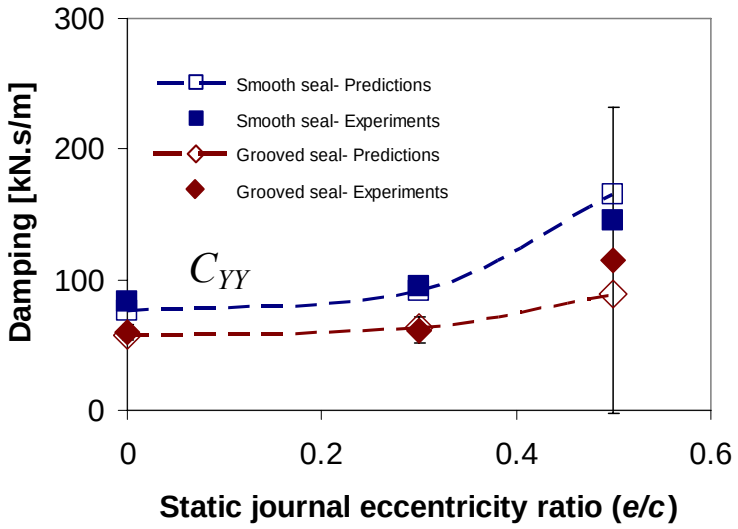

Figure 35 Direct damping coefficients (C_{ii}) versus eccentricity. Measurements in a smooth seal and a seal with inner land groove (c_{III} = 16c), 10000 rpm, 70 bar [29]. Predictions for smooth seal and seal with inner land groove ($c_{\eta_{III}}$ = 7c).

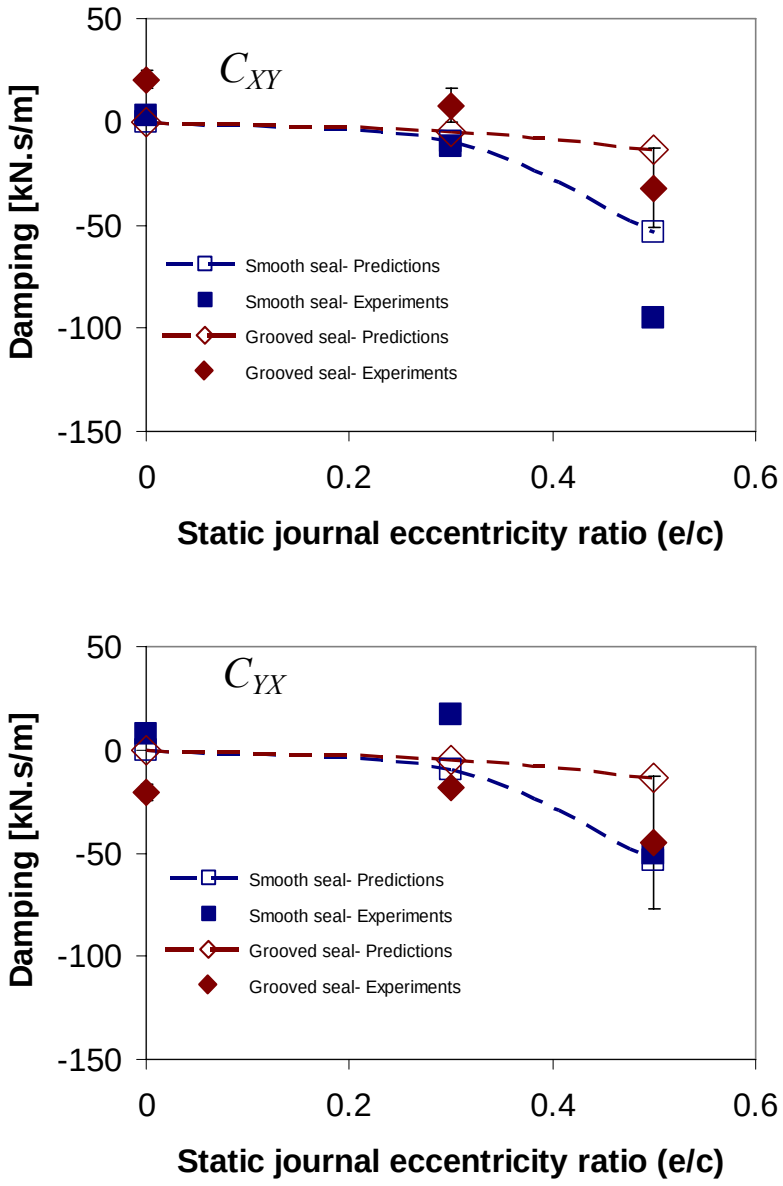

Figure 36 Cross-coupled damping coefficients (C_{ij}) versus eccentricity. Measurements in a smooth seal and a seal with inner land groove (c_{III} = 16c), 10000 rpm, 70 bar [29]. Predictions for smooth seal and seal with inner land groove ($c_{\eta_{III}}$ = 7c).

Figure 37 depicts the direct added mass coefficients versus the static journal eccentricity ratio. Predicted and experimental cross-coupled added mass coefficients (M_{XY}, M_{YX}) are nearly null. The direct added mass coefficients (M_{XX}, M_{YY}) present good

correlation with the experimental data. In particular, the analysis predicts a larger added mass coefficient for the grooved oil seal as the experiments also reveal. Note that the predicted added mass coefficient is nearly constant for all the test journal eccentricities.

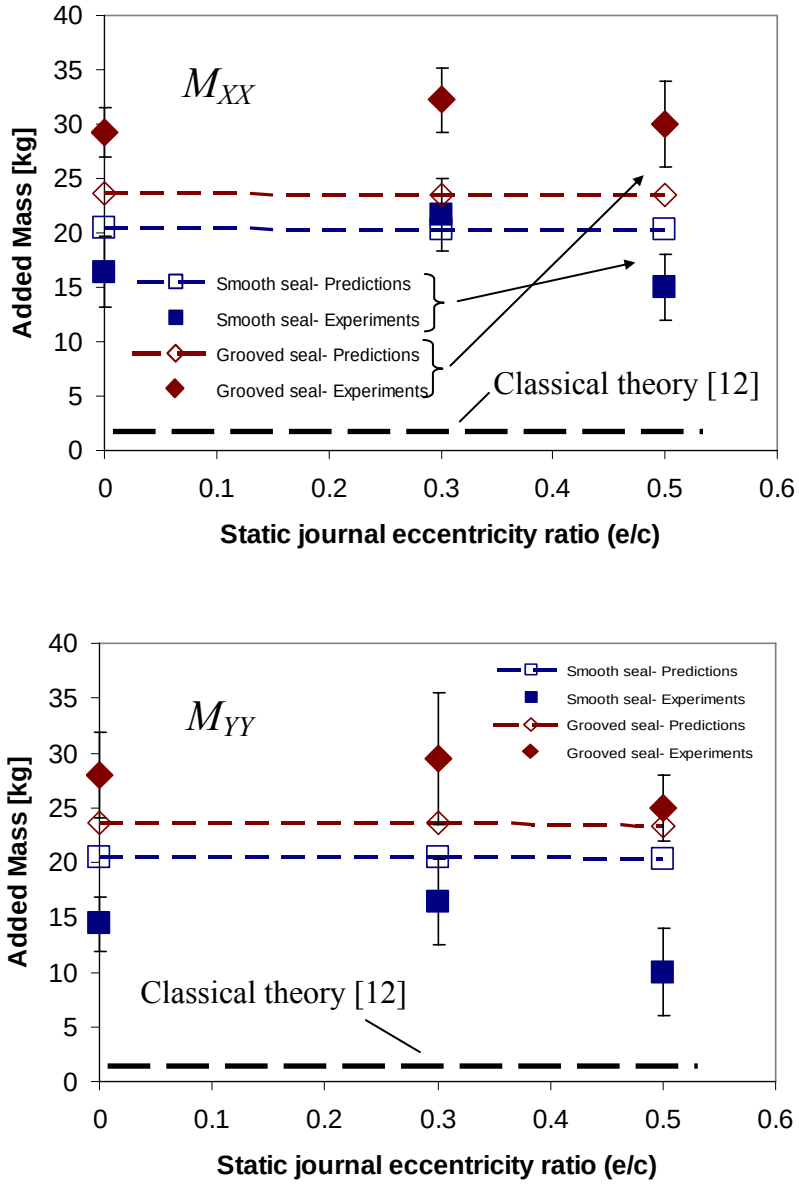

Figure 37 Added Mass coefficient (M_{XX}, M_{YY}) versus eccentricity. Experiments for smooth seal and seal with inner land groove (c_{III} = 16c), 10000 rpm, 70 bar [29]. Predictions for smooth seal and seal with inner land groove using ($c_{\eta_{III}}$ = 7c).

Figure 38 present the seal leakage versus the static journal eccentricity at 10,000 rpm and 70 bar feed pressure. The results show good correlation between experiments and predictions with a variation of less than ~15 % in both seals. Note that, contrary to intuition, the experiments and predictions show that the smooth seal leaks more than the grooved seal because its effective viscosity (land clearance) is slightly lower (larger) due to larger power losses inducing a temperature rise.

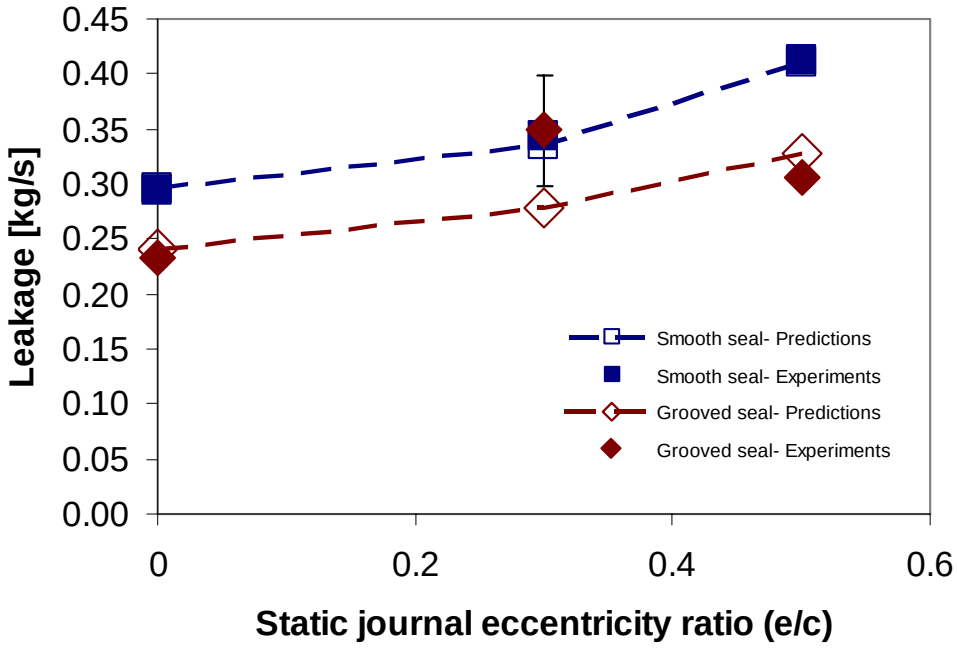

Figure 38 Seal leakage versus eccentricity. Experiments for smooth seal and seal with inner land groove (c_{III} = 16*c*), 10000 rpm, 70 bar [29]. Predictions for smooth seal and seal with inner land groove using ($c_{\eta_{III}}$ = 7*c*).

7. SUMMARY AND CONCLUSIONS

This dissertation presents a fluid flow model towards improving the prediction of the force coefficients in grooved oil seals and SFDs. In particular, the analysis focuses on the prediction of force coefficients in a SFD and oil ring seal test configurations (Ref. [27, 29]), both including feed/discharge grooves.

In SFDs, grooves are used to feed oil into the damper or as part of end sealing arrangements. The SFD test configuration in Ref. [27], yields unexpectedly large added mass coefficients that are largely underpredicted by classical theory [4]. Similarly, an oil seal test configuration tested in Ref. [29] shows large added mass coefficients that are also not accurately predicted. This test configuration includes a central plenum that feeds lubricant to two seals. The seals are installed in parallel as an axially symmetric arrangement to balance the test rig thrust forces. In addition, this configuration holds a grooved oil seal. Grooves are typically machined in oil ring seals to isolate and to divide the seal land into shorter length lands and hence to minimize the destabilizing effect (cross-coupled coefficients) [33]. However, predictions of force coefficients for grooved oil seals from available models (i.e. Ref. [28]) largely underpredict experimental results, which is a clear indication that the grooves do not completely isolate the dynamic pressure field of the contiguous lands.

The proposed model to improve the predictions of force coefficients in grooved SFDs and oil seals is based on a fluid flow analysis that divides the multiple groove annular cavities into flow regions of constant clearance. The analysis treats both the groove and film land sections similarly in terms of the fluid flow equations, and it considers both the circumferential and axial dynamic pressure variations across the groove and land regions. At the groove regions, an effective groove depth (d_η) and clearance ($c_\eta = d_\eta + c$) are defined based on qualitative observations of the laminar flow pattern through annular cavities, and supported by experiments [27] evidencing the generation of relatively large dynamic pressures in deep grooves. Solutions for small

amplitude journal circular centered and off-centered orbits are presented. A closed-form solution is obtained for circular centered orbits

The predictions of force coefficients for the oil seal and SFD are presented as a function of effective groove depths and compared to experimental results (SFD [27] and oil seal [29]). Comparisons of predicted and experimental force coefficients show excellent correlation for a narrow range of effective groove clearances. Most importantly, the parametric study shows that the best analytical correlation for the force coefficients is obtained for the minimum effective groove depths for which the overall damping is not substantially modified (<10%) from that calculated using the actual physical feeding/discharge groove or plenum depth for both the oil seal and SFD. In the case of the SFD, the boundary conditions include actual pressure measurements at the discharge groove. The pressure field measurements, also available at the film land are compared to predictions based on an effective groove clearance (c_η= 14) obtained from the parametric study.

For the oil seal test rig, the force coefficients are compared to experimental force coefficients from centered and off-centered journal positions. The effective groove depth for the central plenum is obtained as in the case of the SFD from comparisons of damping and added mass coefficients to experimental results for the smooth oil seal. In terms of a inner-land groove in a seal, the parametric study shows good correlation with the experimental data for effective clearance (c_η) values smaller or equal to 50% of the groove depth.

A finite element method based on Ref. [54] is extended and implemented to obtain the force coefficients for journal off-centered operation. Predictions of force coefficients are compared to experimental results from Ref. [29] for three journal eccentricities ε = 0, 0.3 ,0.5. The force coefficients, leakage and reaction forces of a smooth and grooved oil seal are predicted and compared to experimental results. The test grooved oil seal includes a rectangular central groove located at the seal mid-land plane with a depth of 15 times the seal clearance (c=85.9 μm). The predicted parameters are compared to

experimental results for four journal eccentricities (e/c=0, 0.3, 0.5, 0.7) at 10,000 rpm and with a 70 bar oil feed pressure.

Predicted and experimental force coefficients present good correlation for the direct force coefficients for the lower journal eccentricities (e/c=0, 0.3) and moderate to good correlation for e/c=0.5. The cross-coupled stiffness coefficients are also accurately predicted for the lower journal eccentricities. In particular, the current model accurately predicts the reduction of the direct stiffness, direct damping, and cross-coupled stiffness coefficients when adding a circumferential groove to the seal land. The added mass coefficients for both seals are also predicted accurately (within 20 %). Furthermore, the analysis and experimental results indicate that a grooved seal shows larger direct added mass coefficient than a smooth seal.

For journal eccentricity ratios (ε) up to 70% there are discrepancies between the experimental results and predictions for some force coefficients. These discrepancies are attributed to changes of seal clearance and oil properties due the large shear drag torque and forces at such large eccentricity. Nevertheless, the test data reported in Ref. [7] does not offer details on operating conditions and the probable variation of the lubricant properties and seal clearance. Therefore, the predictions are compared with experimental results only for the low to mid-range eccentricities (i.e. ε= 0, 0.3, 0.5).

The current analysis represents a significant improvement over the current predictive tools available to analyze SFD and oil seal configurations that include deep and/or shallow grooves. The proposed model and assumptions prove to be adequate based on the correlation between the predicted and experimental force coefficients. The present work delivers a FORTRAN code for prediction of leakage and force coefficients (*K, M, C*) in grooved SFD and grooved oil seals, as well as a GUI for direct integration into the XLTRC2® rotordynamic software. See Appendix A for details.

The most important conclusions from the current study are:

- Force coefficients in test configurations, like SFD and oil seals, are a function of the ancillary geometries like feeding/discharge arrangements. Deep grooves or plenums do generate dynamic pressures of mainly inertial nature, which lead to

large added mass coefficients. These, however, can now be predicted. Furthermore, there is a specific groove depth where the added mass coefficient peaks. This groove depth value for the studied configurations is < 10c.

- The dynamic pressure field in deep grooves or plenums may be difficult to measure for most practical excitation frequency ranges, especially in the presence of large static pressure differentials. This follows from the inertial nature of the filed and the simple observation that the fluid inertia pressures are proportional to ω^2.
- In grooved oil seals, grooves (short: L <30c and shallow*:* c_g <16c) do not isolate the pressure field of adjacent smooth film lands. While force coefficients are reduced to a lesser extend of what theory [28] otherwise predicts, fluid inertia forces are enhanced for the same reasons above described (i.e. large Re^* values). Furthermore, the effective clearance values that yield the best correlation with experimental data in Ref. [29] (i.e. d_η smaller or equal to 50% of the groove depth) could be generalized for short deep grooves like those found in oil seals.

A more detailed study of the fluid flow in grooved SFDs, including either 3D CFD simulations or experimental flow visualization of the flow induced due to journal whirling motions is in order. Such study could provide actual magnitudes of the velocity and acceleration of the fluid film in grooved SFDs. Furthermore, it would serve to scrutinize the assumptions put forth in the course of this investigation.

An experimental study of the influence of grooves in force coefficients for a wide range of groove depths could also complement this research effort. The investigation should focus on measuring the dynamic pressure field at the grooves and correlating the results to given Re^* values for a number of groove depths. In specific, it would be important to observe the behavior of the added mass coefficients and verify that there is and maximum value for a given groove depth. Also, it would be relevant to study the correlation between the effective groove depth and the penetration depth of the streamline dividing the thru and recirculation flow regions.

REFERENCES

[1] San Andrés, L., "Modern Hydrodynamic Lubrication Theory," Tribology Group, Texas A&M University, http://phn.tamu.edu/me626.

[2] Fritz, R., 1970, "The Effects of an Annular Fluid on the Vibrations of a Long Rotor: Part I Theory," ASME J. Basic Eng., **92**, pp. 923-929.

[3] Kuzma, D. C., 1967, "Fluid Inertia Effects in Squeeze Films," Appl. Scientific Research, **18**, pp.15-20.

[4] Reinhardt, F., and Lund, J. W., 1975, "The Influence of Fluid Inertia on the Dynamic Properties of Journal Bearings," ASME J. Lubr. Technol., **97**(1), pp. 154-167.

[5] Brennen, C., 1976, "On the Flow in an Annulus Surrounding a Whirling Cylinder," J. Fluid Mech., **75**(1), pp. 173-191.

[6] Tichy, J. A., 1983, "The Effect of Fluid Inertia in Squeeze Film Damper Bearings: A Heuristic and Physical Description," ASME Paper 83-GT-177.

[7] Modest, M. F., and Tichy, J.A., 1978, "Squeeze-film Flow in Arbitrary Shaped Journal Bearings Subject to Oscillations," J. Lub. Tech., **100**(3), pp. 323-330.

[8] Tichy, J. A., 1982, "Effects of Fluid Inertia and Viscoelasticity on Squeeze-Film Bearing Forces," ASLE Trans., **25**(1), pp. 125-132.

[9] Tichy, J.A., and Modest, M. F., 1980, "A Simple Low Deborah Number Model for Unsteady Hydrodynamic Lubrication Including Fluid Inertia," J. Rheology, **24**(6), pp. 829-845.

[10] Tichy, J. A., 1984, "Effects of Fluid Inertia and Viscoelasticity on the One-Dimensional Bearing," ASLE Trans., **27**(2), pp. 164-167.

[11] Mulcahy, T. M., 1980, "Fluid Forces on Rods Vibrating in Finite Length Annular Regions," Trans. ASME J. Appl. Mech., **47**(2), pp. 234-246.

[12] San Andrés, 1985, "Effect of Fluid Inertia Effect on Squeeze Film Damper Force Response," Ph.D. Dissertation, Texas A&M University, College Station, TX

[13] San Andrés, L., and Vance, J., 1986, "Effect of Fluid Inertia on Squeeze-Film Damper Forces for Small-Amplitude Circular-Centered Motions," ASLE Trans., **30**(1), pp. 63-68.

[14] Zhang J. X., and Roberts J. B., 1993, "Observations on the Nonlinear Fluid Forces

in Short Cylindrical Squeeze Film Dampers," ASME J. Tribol., **115**(3), pp. 692-698

[15] Zhang J. X., 1997, "Fluid Inertia Effects on the Performance of Short and Long Squeeze Film Dampers Execution Periodic Vibration," ASME J. Tribol., **119**(3), pp. 306-314

[16] Qingchang, T., Wei, L., and Jun, Z., 1997, "Fluid Forces in Short Squeeze-Film Damper Bearings," Tribol. Int., **30**(10), pp. 733-738

[17] Zhang J. X.,1997, "Fluid Inertia Effects on the Performance of Short and Long Squeeze Film Dampers Execution Periodic Vibration," J. Tribol., **119**(3), pp. 306-314.

[18] San Andrés, L., 1992, "Analysis of Short Squeeze Film Dampers with a Central Groove," ASME J. Tribol., **114**(4), pp. 659-665.

[19] Arauz, G., and San Andrés, L., 1994, "Effect of a Circumferential Feeding Groove on the Dynamic Force Response of a Short Squeeze Film Damper," J. Tribol., **116**(2), pp. 369-377.

[20] Arauz, G., and San Andrés L., 1996, "Experimental Study on the Effect of a Circumferential Feeding Groove on the Dynamic Force Response of a Sealed Squeeze Film Damper," J. Tribol., **118**(4), pp. 900-905.

[21] Zhang J. X., and Roberts J. B., 1996, "Force Coefficients for a Centrally Grooved Short Squeeze Film Damper," ASME J. Tribol., **118**(3), pp. 608-616.

[22] Ellis, J., Roberts, J. B., and Hosseini, S. A., 1990, "The Complete Determination of Squeeze-Film Linear Dynamic Coefficients from Experimental Data," ASME J. Tribol., **112**(4), pp. 712-724.

[23] Zhang, J. X., Roberts, J. B., and Ellis, J., 1994, "Experimental Behavior of a Short Cylindrical Squeeze Film Damper Executing Circular Centered Orbits," ASME J. Tribol., **116**(3), pp. 528-534.

[24] Qingchang, T., Ying, C., and Lyjiang, W., 1997, "Effect of a Circumferential Feeding Groove on Fluid Force in Short Squeeze Film Dampers," Tribol. Int., **30**(6), pp. 409-416.

[25] Lund, J., W., and Myllerup, C., M., Hartmann, H., 2003, "Inertia Effects in Squeeze-Film Damper Bearings Generated by Circumferential Oil Supply Groove," J. Vib. Acoust., **125**(4), pp. 495-499.

[26] Kim, K. J., and Lee, C. W, 2005, "Dynamic Characteristics of Sealed Squeeze

Film Damper with a Central Feeding Groove," ASME J. Tribol., **127**(1), pp. 103-111.

[27] San Andrés, L., and Delgado, A., 2007, "Identification of Force Coefficients in a Squeeze Film Damper with a Mechanical End Seal- Centered Circular Orbit Tests," ASME J. Tribol., **129**(3), pp. 660-668.

[28] Semanate, J., and San Andrés, L., 1993, "Analysis of Multi-Land High Pressure Oil Seals," STLE Tribol. Trans., **36**(4), pp. 661–669.

[29] Graviss, M., 2005, "The Influence of a Central Groove on Static and Dynamic Characteristics of an Annular Liquid Seal with Laminar Flow," M.S. Thesis, Texas A&M University, College Station, TX.

[30] Childs, D. W. Rodriguez, L. E., Cullotta, V., Al-Ghasem, A., and Graviss, M., 2006, "Rotordynamic-Coefficients and Static (Equilibrium Loci and Leakage) Characteristics for Short, Laminar-Flow Annular Seals," J. Tribol., **128**(2), pp. 378-387.

[31] Kirk, R., 1986, "Oil Seal Dynamic Considerations for Analysis of Centrifugal Compressors," *Proceedings of the 15th Turbomachinery Symposium*, Houston, TX, pp. 25-34.

[32] Allaire, P. E., and Kocur, J. A. Jr., 1985, "Oil Seal Effects and Subsynchronous Vibrations in High-Speed Compressors," NASA Conf. Publ., pp. 205-223.

[33] Baheti, S., and Kirk, R., 1995, "Finite Element Thermo-Hydrodynamic Solution of Floating Ring Seals for High Pressure Compressors Using the Finite-Element Method," STLE Tribol. Trans., **38**, pp. 86-97.

[34] Childs, D. W., Graviss, M., and Rodriguez, L. E., 2007, "The Influence of Groove Size on the Static and Rotordynamic Characteristics of Short, Laminar-Flow Annular Seals," ASME J. Tribol, **129**(2), pp. 398-406.

[35] Della Pietra, L., and Adiletta, G., 2002,"The Squeeze Film Damper over Four Decades of Investigations. Part I: Characteristics and Operating Features," Shock Vib. Dig, **34**(1), pp. 3-26.

[36] Della Pietra, L., and Adiletta, G., 2002, "The Squeeze Film Damper over Four Decades of Investigations. Part II: Rotordynamic Analyses with Rigid and Flexible Rotors," Shock Vib. Dig., **34**(2), pp. 97-126.

[37] San Andrés, L., and Vance, J. M., 1986, "Experimental Measurement of the Dynamic Pressure Distribution in a Squeeze Film Damper Executing Circular

Centered Motions," ASLE Trans., **30**(3), pp. 332-383.

[38] Zeidan, F. Y., and Vance J. M., 1990, "Cavitation and Air Entrainment Effects on the Response of Squeeze Film Supported Rotors," ASME J. Tribol., **112**, pp. 347-353.

[39] Ramli, M. D., Roberts, J. B., and Ellis, J., 1987, "The Determination of Squeeze Film Dynamic Coefficients from Experimental Transient Data," ASME J. Tribol., **109**(1), pp. 155-163.

[40] Arauz, G. L., 1993, "Experimental Study of a Grooved Squeeze Film Damper," M.Sc. Thesis, Texas A&M University, College Station, TX.

[41] Tichy, J. A. and Bou-said B., 1991, "Hydrodynamic Lubrication and Bearing Behavior with Impulsive Loads," ASLE Tribol. Trans., **34**(4), pp. 505-512.

[42] Zeidan, F.Y., San Andrés, L., and Vance, J. M., 1996, "Design and Application of Squeeze Film Dampers in Rotating Machinery," *Proceedings of the 25th Turbomachinery Symposium*, Houston, TX, pp.169-188.

[43] Childs, D., 1993, *Turbomachinery Rotordynamics,* John Wiley & Sons, Inc., New York, Chap. 3.

[44] San Andrés, L., "Modern Hydrodynamic Lubrication Theory: Class Notes #12," Tribology Group, Texas A&M University, http://phn.tamu.edu/me626.

[45] Kaneko, S., Hori, Y., and Tanaka, M., 1984, "Static and Dynamic Characteristics of Annular Plain Seals," *Proceedings of the 3rd IMechE International Conference of Vibrations in Rotating Machinery*, York, England, pp. 205-214.

[46] Zirkelback, N., and San Andrés, L., 1996, "Bulk-Flow Model for the Transition to Turbulence Regime in Annular Seals," STLE Tribol. Trans., **39**(4), pp. 835–842.

[47] San Andrés, L., Soulas, T., and Fayolle, P., "A Bulk-Flow Model of Angled Injection Lomakin Bearings," J. Eng. Gas Turbine and Power, **129**(1)**,** pp. 195-204.

[48] Arghir, M., Hélène, M., and Frene, J., "Analysis of Tangential-Against-Rotation Injection Lomakin Bearings," J. Eng. Gas Turbine Power, **127**(4), pp. 781-790.

[49] San Andrés, L., and Delgado, A., 2007, "Parameter Identification of an End Sealed SFD Part II: Improved Predictions of Added Mass Coefficients for Grooved SFDs and Oil Seals," TRC report, TRC-SFD-2-07, Texas A&M University, College Station, TX.

[50] Delgado, A., and San Andrés, L., 2008, "A Novel FE Bulk-Flow Model for Improved Predictions of Force Coefficients in Off-Centered Grooved Oil Seals,"

TRC report, TRC-SEAL-1-08, Texas A&M University, College Station, TX.

[52] San Andrés, L., "Modern Hydrodynamic Lubrication Theory: Class Notes #2," Tribology Group, Texas A&M University, http://phn.tamu.edu/me626.

[53] Sinha, S. N, Gupta A. K., and Oberai, M. M., 1981, "Laminar Separating Flow Over Backsteps and Cavities Part II: Cavities," AIAA J., **20**(3), pp. 370-375.

[54] Wyssmann, H. R., Pham T.C., and Jenny, R. C., 1984, " Prediction of Stiffness and Damping Coefficients for Centrifugal Compressor Labyrinth Seals," J. Eng. Gas Turbine Power, **106**, pp. 920-926.

[55] Florjancic, S., 1990, ''Annular Seals of High Energy Centrifugal Pumps: A New Theory and Full Scale Measurement of Rotordynamic Coefficients and Hydraulic Friction Factors,'' Ph.D. Dissertation, ETH Zürich Nr. 9087.

[56] Marquette, O. R., 1994, ''A New Three-Control-Volume Theory for Circumferentially-Grooved Liquid Seals,'' ASME J. Tribol., **118**(1), pp. 276–285.

[57] San Andrés, L., "Modern Hydrodynamic Lubrication Theory: Class Notes #7," Tribology Group, Texas A&M University, http://phn.tamu.edu/me626.

[58] San Andrés, L., 2007, "Modern Lubrication Notes # 7-Analysis of Finite Length Bearings: Reaction Forces and Dynamic Force Coefficients Including Temporal Fluid Inertia Effect," Internal Communication, Tribology Group, Texas A&M University College Station, TX.

[59] San Andres, L., 2005, "FEM Model for Estimating Oil Seal Force Coefficients," Internal Communication, Tribology Group Texas A&M University, College Station, TX.

[60] Reddy J. N., and Gartling, D. K., 2001, *The Finite Element Method in Heat transfer and Fluid Dynamics*, CRC Press, Boca Raton, FL, Chap. 2.

[61] Delgado, A., and San Andrés, L., 2006, "Identification of Force Coefficients in a Squeeze Film Damper with a Mechanical Seal," TRC report, TRC-SFD-1-06, Texas A&M University, College Station, TX.

APPENDIX A
EXCEL PROGRAM INTERFACE FOR PREDICTION OF LEAKAGE AND FORCE COEFFICIENTS IN GROOVED OIL SEALS

The Microsoft Excel® user interface is named XLFEGLOSeal® (Excel Finite element grooved laminar oil seal), as depicted in Fig. A.1. This GUI is part of the rotordynamic software XLTRC2®, and available to members of the Texas A&M University Turbomachinery Research Consortium. The user inputs include:

-Fluid properties: Density and viscosity

-Operating conditions: Inlet and outlet pressures, static journal eccentricity (ratio).

-Geometry: Rotor diameter, clearance, groove depth, number of grooves, inlet and outlet land length, inter-groove length, groove length. The groove depth is set to the actual physical value for groove depths less than (6c), considering that the effective and actual groove depths are relatively similar. For deeper grooves, the pressure driven flow streamlines remain relatively constant regardless of the actual depth, as shown in Fig. 4b. For this case, a constant effective groove depth of d_η=6c is used.

The code outputs direct and cross-coupled force coefficients, seal reactions forces, and leakage as a function of shaft speed.

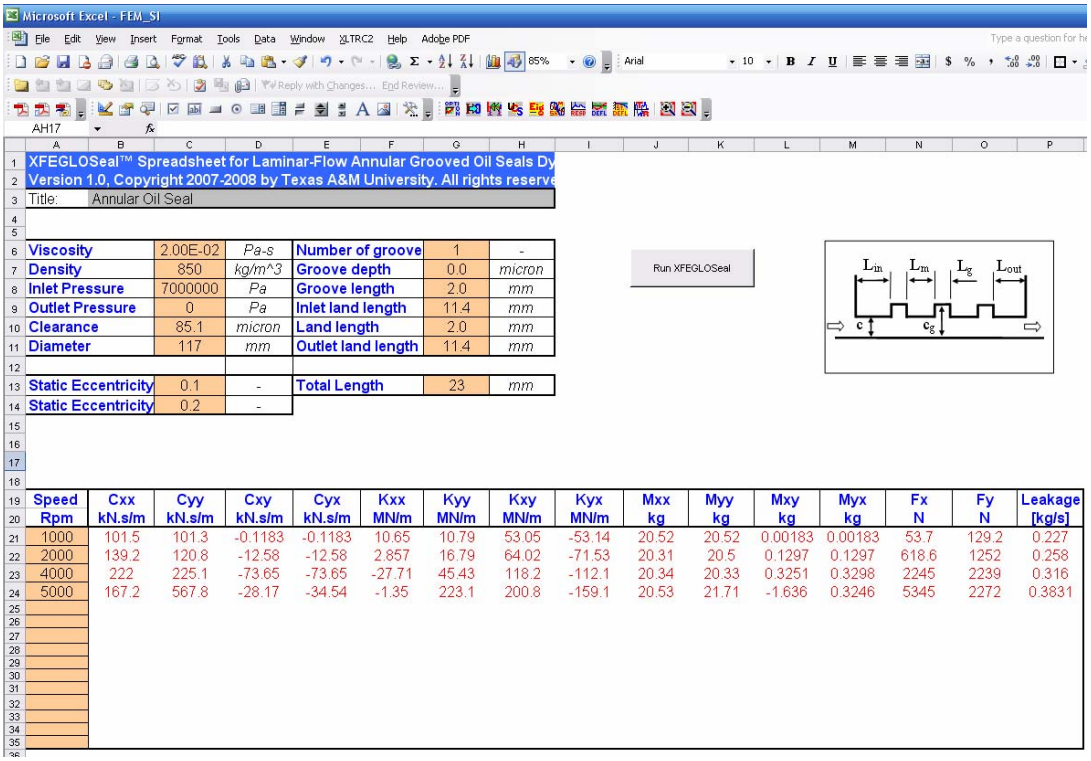

Figure A 1Graphical user interface for XLFEGLOSeal® code. (SI units)

VITA

Name: Adolfo Delgado-Marquez

Address: Texas A&M Turbomachinery Laboratory, College Station, TX 77843-3123
c/o Dr. David Forrest

Email Address: adelgam@gmail.com

Education: B.S., Mechanical Engineering, Universidad Simón Bolívar at Caracas (Venezuela), 2002.
M.S., Mechanical Engineering, Texas A&M University, 2005
Ph.D., Mechanical Engineering, Texas A&M University, 2008

Interests: Turbomachinery- rotordynamics and lubrication.